ISTANBUL TECHNICAL UNIVERSITY ★ GRADUATE SCHOOL

INDUCTION ASSISTED ALUMINIZING OF 316L AND INCONEL 718 ALLOYS

Ph.D. THESIS

Aptullah KARAKAŞ

Department of Metallurgical and Materials Engineering

Metallurgical and Materials Engineering Programme

APRIL 2026

ISTANBUL TECHNICAL UNIVERSITY ★ GRADUATE SCHOOL

INDUCTION ASSISTED ALUMINIZING OF 316L AND INCONEL 718 ALLOYS

Ph.D. THESIS

Aptullah KARAKAŞ
(506182415)

Department of Metallurgical and Materials Engineering

Metallurgical and Materials Engineering Programme

Thesis Advisor: Prof. Dr. Murat BAYDOĞAN

APRIL 2026

İSTANBUL TEKNİK ÜNİVERSİTESİ ★ LİSANSÜSTÜ EĞİTİM ENSTİTÜSÜ

316L VE INCONEL 718 ALAŞIMLARININ İNDÜKSİYON DESTEKLİ ALUMİNYUM KAPLAMA YÖNTEMİYLE KAPLANMASI

DOKTORA TEZİ

Aptullah KARAKAŞ
(506182415)

Metalurji ve Malzeme Mühendisliği Ana Bilim Dalı

Metalurji ve Malzeme Mühendisliği Programı

Tez Danışmanı: Prof. Dr. Murat BAYDOĞAN

NİSAN 2026

Aptullah KARAKAŞ, a Ph.D. student of İTU Graduate School, student ID 506182415, successfully defended the thesis/dissertation entitled "INDUCTION ASSISTED ALUMINIZING OF 316L AND INCONEL 718 ALLOYS", which he prepared after fulfilling the requirements specified in the associated legislations, before the jury whose signatures are below.

Thesis Advisor :	**Prof. Dr. Murat BAYDOGAN** İstanbul Technical University	.....
Jury Members :	**Prof. Dr. Hüseyin CIMENOGLU** Istanbul Technical University	.....
	Prof. Dr. Suleyman Can KURNAZ Sakarya University	.....
	Assoc. Prof. Dr. Hakan YILMAZER Yildiz Technical University	.....
	Asst. Prof. Dr. Faiz MUHAFFEL Istanbul Technical University	.....

Date of Submission : 04 February 2026
Date of Defense : 24 April 2026

To Alper, Bilge and Aysegul…

FOREWORD

I would like to offer my profound gratitude to my beloved wife, Ayşegül KARAKAŞ. As is well known, the doctoral process is long and demanding; it requires substantial time and focus. This inevitably meant sacrificing time with my family, and at times, being unable to give them the attention they deserved. Despite these challenges, she never withheld her support. I dedicate this thesis also to my children, Alper KARAKAŞ and Bilge KARAKAŞ, as a lasting memory. I hope that one day, in their own time, they will achieve far greater accomplishments.

I would like to begin by expressing my sincere gratitude to my thesis advisor, Prof. Dr. Murat BAYDOĞAN. Throughout this doctoral journey, I have learned immensely from him, and the guidance he provided has shaped both my academic perspective and professional discipline principles I will carry throughout my life. We worked together tirelessly, including weekends and late evenings, to bring this study to completion. I extend my deepest appreciation for his unwavering support.

My heartfelt thanks are due to Repkon Holding, where I have been employed for the past eight years. The company has generously supported me throughout my doctoral studies providing financial resources, time, and complete freedom in selecting my thesis topic. I sincerely appreciate the opportunities and trust extended to me by the entire Repkon family.

I would also like to express my sincere thanks to Research Assistant Erdem BALCI. Completing the experimental studies and tests would have been extremely challenging without his assistance. I am truly grateful for his support both in the laboratory and during the manuscript preparation stages, and I feel fortunate to have worked with him as a teammate.

February 2026

Aptullah KARAKAŞ
(Metallurgical and Materials Engineer)

TABLE OF CONTENTS

Page

ABBREVIATIONS

HDA	**:** Hot Dip Aluminizing
SA	**:** Slurry Aluminizing
PA	**:** Pack Aluminizing
PIA	**:** Pack Induction Aluminizing
XRD	**:** X-Ray Diffraction
SEM	**:** Scanning Electron Microscope
EBSD	**:** Electron Back Scatter Diffraction
EDM	**:** Electrical Discharge Machining
CSAM	**:** Cold Spray Additive Manufacturing
CS	**:** Cold Spray
SS	**:** Stainless Steel

LIST OF TABLES

Page

LIST OF FIGURES

Page

INDUCTION ASSISTED ALUMINIZING OF 316L AND INCONEL 718 ALLOYS

SUMMARY

This doctoral study encompasses the application of three different aluminizing methods hot-dip aluminizing (HDA), slurry aluminizing (SA), and pack aluminizing (PA) on AISI 316L stainless steel, Inconel 718 (IN718) superalloy, and IN718 produced by Cold Spray Additive Manufacturing (CSAM), along with the enhancement of these coatings through rapid induction heating. The common objective of all studies is to determine the effectiveness of induction heating in accelerating the formation of aluminide phases within very short durations and to evaluate the resulting coatings in terms of their microstructural, mechanical, tribological, and high-temperature oxidation behaviors.

In the first stage of the thesis, wear and high-temperature oxidation behavior of AISI 316L stainless steel (SS) subjected to two distinct aluminizing processes hot-dip aluminizing (HDA) and slurry aluminizing (SA) both followed by rapid induction heating was investigated. The objective was to assess the efficiency of short-time induction heating as a diffusion treatment and to compare the resulting structural and functional properties of the coatings. Microstructural characterization was carried out using SEM, XRD, and EBSD, while mechanical and tribological properties were evaluated by nanoindentation and wear testing. The HDA coating exhibited a uniform outer morphology, whereas the SA coating developed a lamellar structure due to localized thermal gradients during induction heating. Despite these morphological differences, both coatings consisted of Fe_2Al_5, FeAl, and α-Fe (Al) phases. The SA coating demonstrated a higher surface hardness (13.2 GPa vs. 10.8 GPa for HDA) and a lower coefficient of friction (0.40 vs. 0.52), resulting in a markedly lower wear rate (3.2×10^{-5} mm³/N·m vs. 6.5×10^{-5} mm³/N·m). Isothermal oxidation at 1000 °C for 24 h and 96 h revealed that both coatings transformed toward a protective α-Fe (Al) matrix with a continuous Al_2O_3 scale. However, the coating thickness increased more significantly in the SA samples from 35 μm to 400 μm after 96 h compared to 230 μm for HDA, indicating superior Al diffusion kinetics in the SA process. Overall, the SA process combined with rapid induction heating exhibited superior wear resistance compared to the HDA route, whereas the HDA process combined with the same thermal treatment demonstrated enhanced oxidation resistance relative to the SA.

In the second stage of the thesis, the effect of very fast induction heating for two competitive and cost effective aluminizing process, namely, HDA and SA of IN718 superalloy was compared. Each process produced well adhered coating layers, which comprise two or more layers. Morphological, structural and chemical characterizations of each layer were extensively studied, and formation mechanisms of the coatings were discussed in comparison to each other. The HDA process performed in a molten Al-11 wt. Si bath at 700 °C formed a 120 μm coating layer, mostly comprising of $NiAl_3$. The induction heating for 20 s at 1000 °C increased the coating thickness more than

two times (250 μm), transformed the aluminides to Ni_2Al_3, made the elemental distribution more uniform within the coatings, and also formed $CrSi_2$ precipitates, which might be beneficial for an improved oxidation resistance. In the SA process, the induction heating forms a coating of 43 μm in thickness, which is more uniform than the HDA coatings, and also comprises of two layers having Ni_2Al_3 and NiAl type aluminides. EBSD examination revealed that the SA coating has a uniform grain size and random grain orientation, which are promising for improved oxidation resistance. Evaluation of the results in comparison to each other provided a better understanding of the effect of induction heating on different aluminizing processes. For example, a coating uniformity similar to that of the SA coating can be achieved only after the application of the induction heating in the HDA coatings. Also, the SA process assisted with the induction heating can be applied to various substrates without subjected them to a high temperature for a long time, and would be a promising method for partial and complete aluminizing of Ni-based substrates.

In the third stage of the thesis, the development of aluminide coatings using a Pack Induction Aluminizing (PIA) process on IN718 superalloy, which was produced by CSAM, was investigated. Benefit of the proposed method is to significantly reduce the aluminizing time, from a few hours as for the conventional furnace aluminizing conducted in a furnace to a few ten minutes as for the prosed method. The research also aimed to characterize the resulting coating's microstructure, phase evolution, and tribological performance in comparison to the conventional pack aluminizing furnace. The results confirmed the formation of a dense, dual-layer aluminide coating that grew in thickness from approximately 10 μm to 19 μm with the increase in process time from 5 min to 10 min, respectively. XRD and EDS analyses identified the coating's primary constituents as aluminum-rich intermetallics, with an outer layer of $Ni(Fe,Cr)Al_3$ and an inner layer of $Ni_2(Fe,Cr)Al_3$, characteristic of a high-activity aluminizing process. The PIA treatment significantly enhanced the tribological properties of the IN718 substrate. It reduces friction coefficient, and improves wear resistance reducing the wear track depth by over 80% for the samples treated for the process durations of 10 and 15 min, as compared to the uncoated alloy. These findings demonstrate that the PIA method is a highly effective and rapid technique for producing protective, high-performance aluminide coatings on IN718 superalloy.

316L VE INCONEL 718 ALAŞIMLARININ İNDÜKSİYON DESTEKLİ ALUMİNYUM KAPLAMA YÖNTEMİYLE KAPLANMASI

ÖZET

Bu doktora çalışmasında, AISI 316L paslanmaz çeliği, konvansiyonel yöntemlerle üretilmiş Inconel 718 (IN718) süperalaşımı ve soğuk püskürtme eklemeli imalat yöntemiyle üretilmiş IN718 alaşımı üzerinde indüksiyon destekli alüminyumlama işlemlerinin etkisi sistematik olarak incelenmiştir. Çalışmanın temel amacı, geleneksel alüminyumlama ve difüzyon tavlama işlemlerinde saatler mertebesinde süren işlemlerin, indüksiyon ısıtmanın sağladığı yüksek ısıtma hızı ve lokalize enerji girdisi sayesinde saniyeler veya dakikalar seviyesine indirilebileceğini göstermek ve bu kısa süreli işlemler sonucunda oluşan kaplamaların mikroyapısal, mekanik, tribolojik ve yüksek sıcaklık oksidasyon davranışlarını ortaya koymaktır. Bu kapsamda sıcak daldırma alüminyumlama, bulamaç (slurry) alüminyumlama ve kutu alüminyumlama olmak üzere üç farklı alüminyumlama yaklaşımı ele alınmış; bu yöntemlerin farklı altlık malzemelerde kaplama oluşum mekanizması, faz gelişimi ve performans üzerindeki etkileri karşılaştırmalı olarak değerlendirilmiştir.

Tezin ilk aşamasında, AISI 316L paslanmaz çelik üzerine sıcak daldırma alüminyumlama ve bulamaç alüminyumlama işlemleri uygulanmış, ardından kısa süreli indüksiyon ısıtma ile kaplamaların difüzyon davranışı geliştirilmiştir. Bu bölümde temel amaç, indüksiyon ısıtmanın AISI 316L çeliği üzerinde bir difüzyon tavlama yöntemi olarak ne derece etkili olduğunu belirlemek ve iki farklı alüminyumlama yönteminin kaplama yapısı ile aşınma ve oksidasyon performansı üzerindeki etkilerini karşılaştırmaktır. Kaplamaların mikroyapısal özellikleri SEM, XRD ve EBSD analizleriyle incelenmiş; mekanik ve tribolojik davranışları ise nanoindentasyon ve aşınma testleriyle değerlendirilmiştir. Elde edilen sonuçlar, her iki yöntemde de altlık malzemeye iyi bağlanmış alüminat kaplamaların oluştuğunu göstermiştir. Sıcak daldırma alüminyumlama sonucunda daha homojen ve nispeten düzgün bir dış yüzey morfolojisi elde edilirken, slurry alüminyumlama sonrası indüksiyon ısıtma sırasında oluşan lokal sıcaklık gradyanlarının etkisiyle daha lamelli ve karmaşık bir kaplama yapısı meydana gelmiştir. AISI 316L numunelerde oluşan kaplamalar genel olarak Fe_2Al_5, FeAl ve α-Fe(Al) fazlarından meydana gelmiştir. Bu fazlar, alüminyumun çelik yüzeyine difüzyonu ve demir ile reaksiyonu sonucunda oluşan klasik Fe-Al esaslı alüminat yapılarla uyumludur. Bununla birlikte, kaplama morfolojisi ve faz dağılımı uygulanan alüminyumlama yöntemine bağlı olarak belirgin şekilde değişmiştir. Bulamaç alüminyumlama ile elde edilen kaplamalarda daha yüksek yüzey sertliği, daha düşük sürtünme katsayısı ve daha düşük aşınma oranı elde edilmiştir. Özellikle slurry kaplamalarda ölçülen yaklaşık 13.2 GPa seviyesindeki sertlik değeri, sıcak daldırma yöntemiyle elde edilen kaplamalara kıyasla daha yüksek bir mekanik direnç sağlandığını göstermiştir. Benzer şekilde, bulamaç kaplamalarda sürtünme katsayısının yaklaşık 0.40 seviyesine düşmesi ve aşınma oranının belirgin şekilde azalması, lamelli yapının ve yüksek sertlikteki alüminat fazların aşınma direnci üzerinde olumlu etki yaptığını ortaya koymuştur. Buna karşılık sıcak daldırma

kaplamaları daha düzgün ve sürekli bir yüzey morfolojisi sunduğundan, yüksek sıcaklık oksidasyonu açısından daha kararlı bir davranış sergilemiştir. Bu aşamada gerçekleştirilen 1000 °C'de 24 ve 96 saatlik izotermal oksidasyon testleri, her iki kaplama türünün de yüksek sıcaklıkta önemli bir faz dönüşümü geçirdiğini göstermiştir. Oksidasyon sonrası kaplama yapılarında Al bakımından zengin fazların zamanla α-Fe(Al) esaslı bir matrise dönüştüğü ve yüzeyde koruyucu nitelikte ince bir Al_2O_3 tabakasının oluştuğu belirlenmiştir. Bu koruyucu oksit tabakası, altlık malzemenin yüksek sıcaklıkta oksitlenmesini sınırlandırmış ve özellikle Fe esaslı oksitlerin oluşumunu engellemiştir. Bununla birlikte, bulamaç kaplamalarda kaplama kalınlığının 96 saat sonunda yaklaşık 400 µm seviyesine ulaşması, bu yöntemde alüminyum difüzyonunun daha etkin gerçekleştiğini göstermiştir. Sıcak daldırma kaplamalarında ise kaplama kalınlığı yaklaşık 230 µm'ye ulaşmıştır. Bu sonuçlar, bulamaç alüminyumlama ve indüksiyon ısıtma kombinasyonunun aşınma dayanımı açısından avantajlı olduğunu, sıcak daldırma alüminyumlama ve indüksiyon ısıtma kombinasyonunun ise oksidasyon dayanımı açısından daha kararlı bir yapı sunduğunu ortaya koymuştur.

Tezin ikinci aşamasında, konvansiyonel olarak üretilmiş IN718 süperalaşımı üzerinde sıcak daldırma alüminyumlama ve bulamaç alüminyumlama yöntemleri karşılaştırmalı olarak incelenmiştir. IN718, yüksek sıcaklık dayanımı ve mekanik özellikleri nedeniyle havacılık, enerji ve ileri mühendislik uygulamalarında yaygın olarak kullanılan bir nikel esaslı süperalaşımdır. Ancak bu alaşımın yüksek sıcaklık oksidasyonu ve yüzey aşınması gibi koşullar altında daha uzun süreli kullanılabilmesi için yüzey özelliklerinin geliştirilmesi önem taşımaktadır. Bu kapsamda, tez çalışmasının ikinci bölümünde indüksiyon ısıtmanın Ni-Al esaslı alüminat kaplamaların oluşumu üzerindeki etkisi değerlendirilmiş ve kısa süreli işlemlerle yüksek sıcaklık uygulamaları için uygun kaplama yapılarının elde edilip edilemeyeceği araştırılmıştır. Sıcak daldırma alüminyumlama işlemi, Al-%11 Si içeren banyoda 700 °C'de gerçekleştirilmiş ve işlem sonucunda yaklaşık 120 µm kalınlığında, büyük ölçüde $NiAl_3$ fazından oluşan bir kaplama tabakası elde edilmiştir. Bu kaplama, indüksiyon ısıtma sonrasında belirgin şekilde kalınlaşmış ve yaklaşık 250 µm seviyesine ulaşmıştır. Aynı zamanda, başlangıçta Al bakımından daha zengin olan $NiAl_3$ fazının, indüksiyon ısıtma ile birlikte Ni_2Al_3 fazına dönüştüğü belirlenmiştir. Bu dönüşüm, indüksiyon ısıtmanın yalnızca kaplama kalınlığını artırmakla kalmadığını, aynı zamanda kaplama içerisindeki element dağılımını daha homojen hâle getirerek faz evrimini de yönlendirdiğini göstermektedir. Ayrıca kaplama içerisinde $CrSi_2$ çökeltilerinin oluşması, krom ve silisyumun difüzyon sürecine katıldığını ve bu çökeltilerin yüksek sıcaklık oksidasyon direncine katkı sağlayabileceğini düşündürmektedir.

Tezin üçüncü aşamasında, soğuk püskürtme eklemeli imalat yöntemiyle üretilmiş IN718 alaşımı üzerinde kutu alüminyumlama işlemi indüksiyon ısıtma ile birlikte uygulanmıştır. Soğuk püskürtme eklemeli imalat yöntemiyle üretilen malzemeler, üretim doğası gereği konvansiyonel dövme alaşımlara kıyasla farklı porozite, tane yapısı, deformasyon geçmişi ve yüzey özellikleri gösterebilmektedir. Bu nedenle, bu tür malzemeler üzerinde uygulanacak yüzey işlemlerinin etkisinin ayrıca incelenmesi gerekmektedir. Bu bölümde önerilen kutu indüksiyon alüminyumlama yöntemi, geleneksel fırınlı kutu alüminyumlama işlemlerinde birkaç saat süren proses süresini yalnızca birkaç dakikaya indirmeyi hedeflemiştir. Böylece eklemeli imalatla üretilmiş IN718 alaşımının yüzeyinde kısa sürede alüminat kaplama oluşturulması ve bu kaplamanın tribolojik performansa etkisinin değerlendirilmesi amaçlanmıştır. Elde

edilen sonuçlar, işlem süresinin 5 dakikadan 10 dakikaya çıkarılmasıyla kaplama kalınlığının yaklaşık 10 μm'den 19 μm'ye yükseldiğini ve yoğun, çift katmanlı bir alüminat kaplama yapısının oluştuğunu göstermiştir. XRD ve EDS analizleri, dış katmanın ağırlıklı olarak $Ni(Fe,Cr)Al_3$, iç katmanın ise $Ni_2(Fe,Cr)Al_3$ fazlarından meydana geldiğini ortaya koymuştur. Bu faz yapısı, yüksek aktivite alüminyumlama koşullarında beklenen Al bakımından zengin nikel alüminat fazlarıyla uyumludur. Kaplama yapısının çift katmanlı olması, yüzeyden altlığa doğru gelişen Al konsantrasyon gradyanı ve karşılıklı element difüzyonunun bir sonucu olarak değerlendirilmiştir. İndüksiyon ısıtmanın sağladığı hızlı ısıl çevrim, çok kısa sürelerde alüminyumun yüzeye taşınmasını ve nikel esaslı altlıkla reaksiyona girerek alüminat fazları oluşturmasını mümkün kılmıştır. Kutu indüksiyon alüminyumlama işlemi, soğuk püskürtme ile üretilmiş IN718 altlığın tribolojik performansını da belirgin şekilde iyileştirmiştir. Kaplamasız numuneye kıyasla kaplanmış numunelerde sürtünme katsayısı düşmüş, özellikle 10 ve 15 dakikalık işlem sürelerinde aşınma izi derinliği %80'den fazla azalmıştır. Bu sonuç, yüzeyde oluşan sert ve yoğun alüminat tabakanın karşı yüzeyle temas sırasında altlığı koruduğunu ve aşınma mekanizmasını sınırlandırdığını göstermektedir. Bununla birlikte, işlem süresinin artmasıyla kaplama kalınlığı ve faz dağılımı değişmiş, bu da tribolojik davranış üzerinde doğrudan etkili olmuştur. Bu bölümde elde edilen bulgular, kutu indüksiyon alüminyumlama yönteminin yalnızca konvansiyonel alaşımlar için değil, aynı zamanda eklemeli imalatla üretilmiş nikel esaslı süperalaşımlar için de uygulanabilir ve etkili bir yüzey mühendisliği yaklaşımı olduğunu göstermektedir.

Tez genelinde elde edilen bulgular birlikte değerlendirildiğinde, indüksiyon ısıtmanın alüminyumlama işlemlerinde yalnızca bir ısı kaynağı olarak değil, aynı zamanda difüzyon kinetiğini hızlandıran ve kaplama gelişimini yönlendiren etkili bir proses aracı olarak kullanılabileceği ortaya konmuştur. Geleneksel difüzyon tavlama işlemlerinde uzun sürelerde gerçekleşen faz dönüşümleri ve kaplama büyümesi, indüksiyon ısıtmanın sağladığı hızlı ve lokalize ısı girdisi sayesinde çok daha kısa sürelerde elde edilmiştir. AISI 316L paslanmaz çelikte Fe-Al esaslı alüminid kaplamalar, IN718 süperalaşımında ise Ni-Al esaslı alüminat kaplamalar başarıyla geliştirilmiştir. Ayrıca, soğuk püskürtme eklemeli imalat yöntemiyle üretilmiş IN718 üzerinde kutu indüksiyon alüminyumlama işleminin uygulanabilirliği gösterilerek, bu yöntemin yeni nesil üretim teknikleriyle birlikte kullanılabilecek potansiyele sahip olduğu ortaya konmuştur. Sonuç olarak, bu tez çalışması indüksiyon destekli alüminyumlamanın AISI 316L paslanmaz çelik, konvansiyonel IN718 ve soğuk püskürtme eklemeli imalat yöntemiyle üretilmiş IN718 alaşımları için hızlı, enerji verimli ve yüksek performanslı bir yüzey mühendisliği yöntemi olarak kullanılabileceğini göstermiştir. Kısa süreli indüksiyon ısıtma altında uygulanan sıcak daldırma, bulamaç ve kutu alüminyumlama işlemleri; kaplama oluşum mekanizmaları, faz gelişimi ve fonksiyonel performans açısından kapsamlı biçimde değerlendirilmiştir. Elde edilen sonuçlar, işlem süresinin saatler mertebesinden saniyeler veya dakikalar seviyesine indirilebileceğini, buna rağmen altlık malzemeye iyi bağlanmış ve difüzyon kontrollü alüminat kaplamaların oluşturulabileceğini ortaya koymuştur. İndüksiyon ısıtmanın sağladığı yüksek ısıtma hızları ve lokalize ısıl etki, atomik difüzyonu belirgin şekilde hızlandırmış; aynı zamanda altlık malzemelerde istenmeyen mikroyapısal bozulmaların oluşmasını sınırlamıştır. Bu nedenle indüksiyon destekli alüminyumlama, özellikle yüksek sıcaklıkta çalışan mühendislik malzemeleri için hem proses verimliliği hem de yüzey performansı bakımından gelecek vadeden bir yöntem olarak değerlendirilebilir.

1. INTRODUCTION

The service life of metallic materials in industrial applications is often governed not only by their bulk properties, but also by their surface characteristics. Surface-dominated degradation mechanisms such as wear, oxidation, corrosion, and high-temperature phase instability can lead to significant performance losses in critical components used in the energy, defense, petrochemical, and aerospace sectors. Therefore, surface engineering has become a central strategy in modern materials science, serving both performance enhancement and cost-reduction objectives. The development of this field has undergone a long evolutionary trajectory, starting from early pack cementation practices and progressing toward today's diffusion-controlled coating technologies.

Diffusion coatings are among the oldest and most reliable methods in surface engineering. Rather than depositing an external film, these coatings rely on the formation of new phases within the substrate surface region through solid-state diffusion of alloying elements at elevated temperatures. Atomic diffusion processes, governed by Fick's laws, create a metallurgical bond between the coating and substrate, providing superior high-temperature strength, oxidation resistance, and adhesion stability. However, a major disadvantage of conventional diffusion coatings is the requirement for long-duration high-temperature treatments, which increase energy consumption and reduce processing efficiency in industrial environments.

In this context, aluminizing introducing Al into the surface to form aluminide phases stands out as one of the most effective protection methods for high-temperature applications. Intermetallic phases such as NiAl and Ni_2Al_3 form a stable α-Al_2O_3 scale that offers exceptional resistance to oxidation and sulfidation. For this reason, aluminizing is widely used in jet engine turbine blades, refinery reformer tubes, power plant components, chemical processing equipment, and metallic parts where the balance between wear and oxidation resistance is critical. Although the three main aluminizing methods SA, HDA and PA have long been used in industry, the diffusion

heat treatment required in all these routes typically lasts for several hours, posing a major limitation.

Recent advancements have introduced new approaches in terms of processing speed, energy efficiency, and thermal control. One such approach is induction-assisted aluminizing, which has gained attention due to its ability to reduce coating times to the order of minutes and significantly accelerate diffusion kinetics through rapid heating rates. Induction heating generates heat directly within the material via electromagnetic induction, enabling a rapid and homogeneous thermal cycle. Consequently, diffusion stages that normally require hours in conventional furnaces can be completed within minutes. This not only reduces energy consumption but also considerably shortens maintenance and coating durations in industrial applications.

In this doctoral thesis, induction-assisted aluminizing was applied using three different aluminizing routes (slurry, hot-dip, and pack) on three material systems: AISI 316L stainless steel, IN718 superalloy, and IN718 produced by CSAM. The microstructural evolution, phase formation, diffusion behavior, wear performance, and oxidation resistance of the resulting coatings were comprehensively investigated.

2. RESEARCH OBJECTIVES

2.1 Enhanced Wear and Oxidation Resistance of AISI 316L Stainless Steel via Slurry and Hot-Dip Aluminizing Assisted by Rapid Induction Heating

This study examines the behavior of aluminide coatings produced on AISI 316L stainless steel through HDA and SA, both followed by rapid induction heating. The main objective is to determine whether short induction cycles can effectively act as an alternative to long conventional diffusion treatments. Microstructural evolution of the coatings was assessed using SEM, XRD and EBSD. Both aluminizing routes generated similar phases but exhibited distinct morphological features. The hot-dip method produced a more uniform and compact outer layer, while the slurry method developed a lamellar morphology due to localized thermal gradients during induction heating. Nanoindentation results indicated that the slurry coatings achieved higher hardness. Tribological tests showed that slurry aluminizing resulted in a lower friction coefficient and significantly improved wear resistance. Oxidation experiments demonstrated that both coatings could form a protective alumina scale at high temperatures. The slurry route exhibited a faster aluminum diffusion response under induction conditions. Overall, slurry combined with induction heating performed better in terms of wear resistance, whereas hot-dip combined with induction heating showed superior oxidation performance.

2.2 Induction Assisted Hot-Dip and Slurry Aluminizing of Inconel 718

This study explores the influence of rapid induction heating on aluminide coatings produced by HDA and SA on conventionally forged IN718 superalloy. The objective is to clarify how extremely short heating durations affect phase transformations and coating uniformity. The hot-dip process initially formed an aluminide layer rich in aluminum-based intermetallics. Induction heating transformed this coating into a thicker, more diffusion-driven structure with a different dominant phase. Elemental gradients became more uniform after the induction step. Under the same thermal conditions, slurry aluminizing generated a thinner but more homogeneous bilayer

structure. EBSD analysis revealed that slurry coatings exhibited finer grains and random crystallographic orientation. These features are advantageous for long-term oxidation resistance. Comparative evaluation showed that achieving the uniformity obtained in slurry coatings was possible in hot-dip coatings only after applying induction heating. The study demonstrated that induction heating significantly accelerates diffusion and phase evolution in both aluminizing methods for Ni-based superalloys.

2.3 Pack Aluminizing by Induction Heating: Application to Inconel 718 Produced by Cold Spray Additive Manufacturing

This study focuses on the development of aluminide coatings on cold-sprayed IN718 using the pack induction aluminizing method. The aim is to create a rapid aluminizing process capable of reducing treatment time from hours to only minutes. The PIA route successfully produced dense and well-defined multilayer aluminide coatings within a very short duration. Microstructural analysis revealed an upper intermetallic layer enriched in aluminum and a lower layer composed of a distinct aluminide phase characteristic of high-activity pack processes. Coating thickness increased progressively with longer induction exposure. The identified phases confirmed the accelerated diffusion behavior enabled by induction heating. Tribological evaluation showed that the coatings significantly reduced friction. Wear testing demonstrated substantial protection of the substrate, with markedly lower wear damage compared to the uncoated material. The findings indicate that PIA is a fast, energy-efficient, and highly effective method for producing high-performance aluminide coatings on additively manufactured IN718.

3. ENHANCED WEAR AND OXIDATION RESISTANCE OF AISI 316L STAINLESS STEEL VIA SLURRY AND HOT-DIP ALUMINIZING ASSITED BY RAPID INDUCTION HEATING[1]

3.1 Introduction

AISI 316L is a commonly used stainless steel in petrochemistry, nuclear and aerospace applications due to its superior corrosion resistance resulting from stable oxide layer (mainly Cr_2O_3) on the surface. It also exhibits excellent formability characteristics resulting from high strain hardening exponent. It is used up to a mid-temperature of 450 °C requiring high oxidation resistance. Further increasing the temperature leads to deterioration of mechanical properties because of formation of detrimental sigma phase [1], and loss of surface properties such as oxidation resistance [2]. Because 316L SS is widely used in various engineering applications, it is desirable to have good tribological properties as well, when in contact with other engineering components. However, its wear properties are not satisfactory due to its low hardness and low yield strength, and hence need to be improved by surface modifications. In this context, nitriding and carburizing are primarily effective in improving surface hardness and wear resistance, but offer limited protection against oxidation [3]. On the other hand, thermal spray coatings can offer good oxidation resistance at high temperatures, and also improve wear resistance, but they lack of adhesion strength with the substrate [4]. Thus, in order to combine both improved wear and oxidation resistance with a good adhesion to the substrate, aluminide coatings are promising surface processes to protect the surface of 316L stainless steel against wear and oxidation in severe industrial environments.

Aluminizing can be performed by many ways including hot dip aluminizing (HDA) HDA [5], slurry aluminizing (SA) SA [6], pack aluminizing (PA) PA [7] and chemical

[1]This chapter is based on the article: Karakas, A., Balci, E. and Baydogan, M. (2025). Enhanced Wear and Oxidation Resistance of AISI 316L Stainless Steel via Slurry and Hot-Dip Aluminizing Assisted by Rapid Induction Heating, Langmuir, 41(48), 0743-7463. https://doi:10.1021/acs.langmuir.5c04513

vapor deposition (CVD) [8]. HDA, SA and PA processes are relatively easy to implement in terms of required equipment and ease of applicability, while CVD is more expensive because it needs to have a highly sophisticated equipment. Depending on the Al source, process temperature and time, various aluminide phases form, and thus the final properties of the coatings can be significantly varied. In order to achieve at the desired properties, tailoring the process parameters are of vital importance. There are studies in the literature investigating the wear and oxidation behavior of 316L SS after aluminizing. Yuan et al [9] reported the formation of $(Fe,Cr,Ni)_2Al_5$ and $(Fe,Cr,Ni)Al_3$ type aluminides after HDA process performed in a molten bath of pure Al, while $Al_7(Fe,Cr)_2Si$ phase was formed in molten Al-Si bath. After diffusion annealing at 900 °C for 3 h, the surface layer was transformed into (Fe,Cr,Ni)Al type aluminide. Majumdar et al [10] determined that a Fe_2Al_5 type aluminide formed on the surface of 316 SS after pack aluminizing at 450-700 °C for 4 to 16 h, and this layer was transformed into a FeAl/Fe(Al)-based aluminide layer by diffusion annealing at 1050 °C for 1.5 h. Wang et al. [11] formed a FeAl-based coating layer on 316L SS through slurry aluminizing with diffusion annealing at 980 °C for 5 h in an Ar atmosphere, which was found to be significantly enhanced the oxidation resistance at high temperatures. In the HDA and PA processes, diffusion annealing is commonly applied to modify the aluminide coatings as a post process. On the other hand, SA can only be achieved by diffusion annealing because this process is carried out by spraying the slurry onto the surface at room temperature and an annealing is necessarily required for the formation of aluminide layers.

Compared with conventional furnace diffusion annealing, rapid induction-assisted aluminizing provides substantial advantages in terms of energy efficiency, sustainability, and process control. Induction heating minimizes the processing time from several hours to only a few seconds and confines the heat to the near-surface region, thereby reducing the total energy consumption by more than an order of magnitude. The localized and short-duration heating also prevents grain coarsening and preserves the mechanical integrity of the substrate, which is particularly beneficial for large or geometrically complex components [12]. From an environmental perspective, the significant reduction in heating time and electrical energy demand translates directly into lower CO_2 emissions, aligning with global decarbonization goals in manufacturing. These merits highlight the industrial relevance of rapid

induction-assisted aluminizing, especially for components operating under severe environments such as petrochemical heat-exchanger tubes, turbine blades, and aerospace engine parts, where both oxidation resistance and sustainable processing are crucial. For example, Takesue et al [13] nitrided titanium gr2 alloy with induction heating at 900 °C for 3 min, while conventional nitriding process takes more than 10 h. Chen et al [14] applied induction heating to bioactive alkali-treated titanium and they observed that induction heated samples have higher adhesion strength than conventional heated sample. Hu et al. [15] carried out induction heating with pack chromizing and they observed that wear resistance and hardness are higher than conventional chromized samples. Yang et al. [16] used induction heating for cold spray deposition instead of conventional heating, they achieved similar microstructure with induction heating within minutes.

Although numerous studies have been conducted on aluminizing of 316L stainless steels, and utilizing induction as a heating method in various thermochemical processes, to our knowledge, no study has combined aluminizing with induction heating on 316 stainless steel. This study was undertaken to address this gap. To this end, two commonly used aluminizing processes, the HDA and SA methods, were implemented using induction heating applied for a very short time. This rapid induction heating also aimed to minimize the substrate heating time to prevent loss of strength. After the aluminizing process was performed and the morphological, microstructural, and crystallographic properties were characterized, wear and oxidation tests were also conducted to evaluate the performance of the aluminizing processes in service environments.

3.2 Experimental Methods

3.2.1 Hot dip and slurry aluminizing

316L round bars supplied in the diameter of 30 mm were cut into 15 mm thick samples. Prior to the aluminizing processes, the sample surfaces were ground with 320-grit sandpaper for 2 min, thereafter undergoing ultrasonic cleaning in ethanol for 5 min, and subsequently rinsed with acetone to achieve optimal surface cleanliness. In the HDA process, the samples were immersed in a graphite crucible containing molten Al-11 wt.% Si alloy maintained at a temperature of 700 °C for 9 min, followed by removal from the bath and cooling in still air until reaching ambient temperature. They were

subsequently annealed by induction heating at 1000 °C for 20 s (these samples referred as HDA samples). In the SA method, the slurry was formulated by dissolving a binder in a solvent (55 wt.%) and integrating aluminum microparticles (45 wt.) with an average particle size ranging from 30 to 35 μm (Nanografi, 99.9% purity). The solvent utilized was a mixture of polyvinyl butyral (PVB) and methyl ethyl ketone in a 1:10 mass ratio. All constituents were meticulously combined using a magnetic stirrer for a period of 1 h, followed by ball milling for 24 h to ensure the attainment of a uniform slurry. The resultant slurry was subsequently applied to the surfaces by air brushing. Slurry deposit was calculated as 18 mg/cm² by weighing the samples before and after the spraying. After drying the samples at the room temperature they were subjected to induction heating at 1000 °C for 20 s to form an aluminide coating, and cooled to the room temperature in air afterwards (these samples referred as SA samples).

3.2.2 Induction heating

The induction heating was conducted using a coil shown in Fig. 3.1 (model RT-380M50, manufactured by Reterm Induction Heating Limited, TUR), which operates at a maximum power of 50 kW and a maximum frequency of 20 kHz.

Figure 3.1 : General view of induction heating equipment.

The suitable helical coil was chosen according to the geometrical configuration and dimensions of the samples, ensuring a separation of 10 mm between the coil and the sample. In order to mitigate the risk of overheating, the induction coil was perpetually cooled through the utilization of a water circulation apparatus. The induction current was calibrated to elevate the temperatures of the samples from ambient conditions to 1000 °C at a rate of 50 °C/s. Temperature was monitored by a pyrometer during the heating. Upon attaining the designated temperature, the coated samples were maintained at this elevated temperature for 20 s, and cooled to the room temperature.

3.2.3 Nanoindentation

Nanoindentation tests were performed on the cross-sections of the coatings and the substrate using a CSM nanoindentation tester equipped with a Berkovich indenter. A maximum indentation load of 100 mN was applied with a loading and unloading speed of 500 mN/min. The maximum load was maintained for 10 s, and each measurement was repeated three times for each coating layer and the substrate to ensure reproducibility. Young's modulus of the coatings were calculated using the Oliver & Pharr method [17], and elastic recovery was determined from the loading – unloading curves of the indentation through Eq 3.1.

$$\text{Elastic Recovery } (\%) = \frac{h_{max} - h_r}{h_r} \text{ x100} \tag{3.1}$$

where h_{max} is maximum indentation depth during loading, h_r is residual depth after unloading.

3.2.4 Wear test

Reciprocating wear tests were performed on the surface of the aluminized samples at room temperature with a relative humidity of 40-45 %. In the wear tests, the counterface was an Al_2O_3 ball with a diameter of 6 mm. The normal load, sliding velocity, stroke length, and total sliding distance were 3 N, 10 mm/s, 5 mm, and 50 m, respectively. During the wear tests the friction force were continuously monitored by means of load cell, and then was divided by the normal load to calculate the friction coefficient. Following the wear tests, the wear tracks were scanned by using a 2-D surface profilometer (Veeco Dektak 6M) to measure worn volume (mm^3), which were then divided by the normal load (N), and the total sliding distance (m) to calculate the wear rate in the unit of mm^3/Nm. The worn surfaces were examined by SEM to compare the samples, and to evaluate the dominant wear mechanisms.

3.2.5 Oxidation tests

Oxidation tests were performed at 1000°C for 24 and 96 h in an open-atmosphere electrical furnace to evaluate the isothermal oxidation behavior of the samples. The specimens were weighed before and after the oxidation using a balance with an accuracy of 0.01 mg to calculate the weight change per unit area of the samples. Following the oxidation, the cross-sections of the samples were prepared in the

conventional manner, and examined by SEM after etching. XRD analysis was also conducted to identify the post oxidation phases on the surface.

3.3 Characterization

Cross-sections of the samples after aluminizing, induction heating, and oxidation processes, were embedded in bakelite, subsequently ground using emery papers, and polished with 1 μm diamond paste in the conventional manner. After etching with oxalic acid for 1 min, the microstructures were examined by a scanning electron microscope (SEM – Thermofisher Quatro) functioning at 25 kV, which was outfitted with an X-ray energy-dispersive spectroscopy (EDS) detector. The analysis of electron backscattered diffraction (EBSD) was executed on an SEM (Tescan MAIA3 XMU) that was equipped with an EBSD detector operating at 20 kV and 6.4 nA, utilizing a step size of 0.09 μm. To facilitate the EBSD analysis, the samples were polished using a vibratory polisher (Mikrotest MVP) at a frequency of 60 Hz for a duration of 2 h in colloidal silica. Qualitative phase analysis was conducted through X-ray Diffraction (XRD) utilizing a Rigaku D-Max 2200 PCI instrument (Cu Kα radiation, λ=0.15418 nm) across 2θ angles ranging from 20 to 80° at a scanning rate of 2°/min.

3.4 Results and Discussion

3.4.1 Micrographs of HDA and SA samples

Cross-sectional SEM micrographs and corresponding EDS analysis of the HDA and SA samples are given in Fig. 3.2. Both samples have 35 μm thick coatings comprising of three layers that can be classified into outer (OL), mid (ML) and inner (IL) layers. They are differentiated from each other according to the contrast difference as seen in the backscattered SEM micrographs in Fig. 3.2a and b. It was observed that ML and IL of both coatings were quite similar in thickness, morphology and contrast. However, there are significant variations in the OL of the coatings. First of all, OL of the HDA sample was more uniform, and OL-ML interface is protruded (Fig. 3.2a), while the OL of the SA sample has a lamellar structure, and the interface was wavy (Fig. 3.2b). Line EDS analysis along the white line seen in Figs. 3.2c and d reveal that the outer layers are rich in Al and Fe in both samples. However, their distribution within this layer is different, namely, Al content decreases, and Fe content increases

in the SA sample, while they are relatively constant over this layer in the HDA sample. This is attributed to the initial coating structure before the induction heating. In the HDA sample, the Fe_2Al_5 layer has been already formed during the immersion to the molten Al-Si bath [18], therefore, an initially formed coating has been subjected to the induction heating encouraging the solid state diffusion [19]. The induction heating, which facilities electromigration and joule heating provide inward diffusion of Al and outward diffusion of Fe [20], resulting an decreasing content of Al towards the inner layers, and decreasing content of Fe towards the surface [20]. On the other hand, in the case of the SA sample, there is no initially formed coating at all. It was just a deposited slurry before the induction heating.

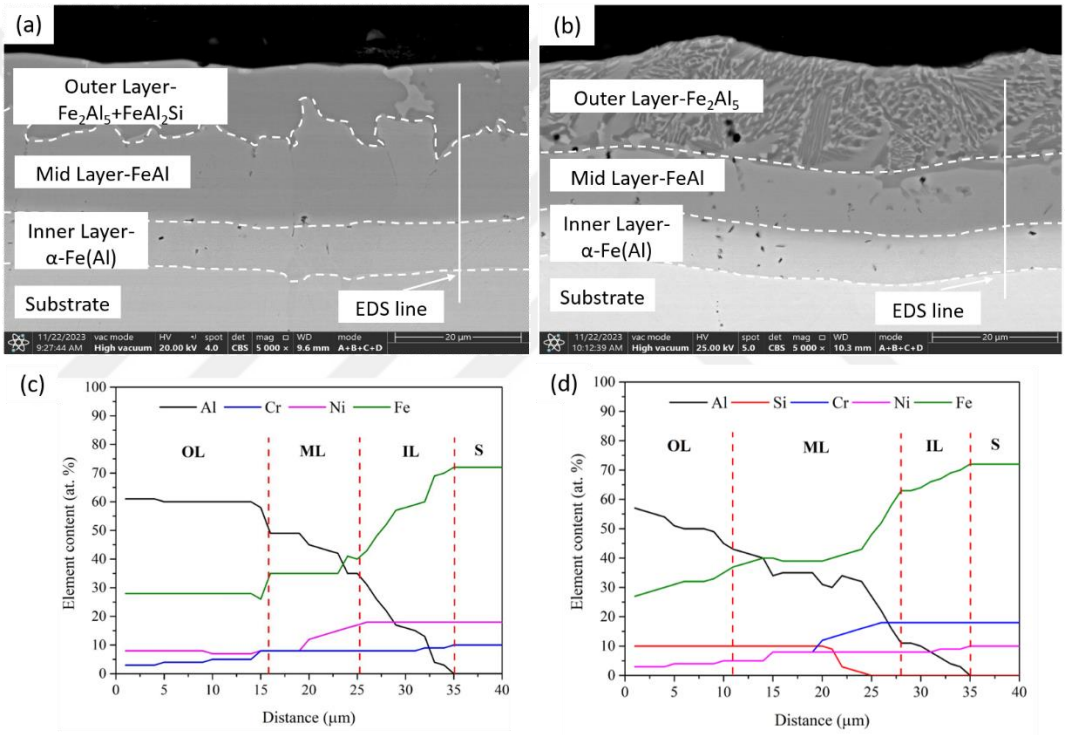

Figure 3.2 : Cross-sectional SEM micrographs and corresponding EDS analyses of aluminized samples: (a,c) HDA, (b,d) SA.

It is widely accepted that two successive mechanisms are responsible for the coating formation in slurry aluminizing, such as dissolution and solid state diffusion [21]. This emphasizes the fact that all coating formation, which consists of dissolution of the substrate elements to the melt, and solid-state diffusion afterwards, takes place during the induction heating that lasts only 20 s. Within this very short period of time, interdiffusion of the elements cannot be so fast, thus the resulting elemental contents must have been largely the result of the initial dissolution stage. Consequently, Al and Fe contents are less uniform in the SA coating. Similarly, for the formation of lamellar

structure in the OL of SA process, the work by Guo et al. [22] can provide a reasonable understanding. In their work, they studied the branching mechanism during binary eutectic directional growth by the phase-field crystal model, and found that heterogeneous nucleation due to decreasing the temperature, interfacial energy, or lattice-mismatch could stimulate lamellar branching. In the SA sample, because of the non-uniform distribution of the elements during the initial dissolution as stated earlier, could be result in the lamellar formation. In the study of Sharma et al. [23]. it was also observed that lamellar morphology of $FeAl_3$ structure was formed after plasma spray Al coating on the surface of pure iron, and diffusion annealing with laser afterwards. The lamellar morphology was thought to be arisen from short-time laser induced after the coating. Similarly, Novak et al. [24]. showed that lamellar FeAl and $FeAl_2Si_3$ structures were formed after reactive sintering of Fe-Al-Si powders.

The aluminide phases change through the coating thickness depending on decreasing Al and increasing Fe content. In both samples, since OL is rich in aluminum, it consists of Fe_2Al_5 phase, but it transforms into FeAl in ML, and α-Fe (Al) in IL. It is compatible with the work of Majumdar et al. [25], who observed that Fe_2Al_5 formation at the outermost, FeAl in the mid layer, and α-Fe (Al) layers in the inner layer after pack aluminizing of 316L alloy at 900 °C for 6 h. It was observed that ML and IL of both samples have different type of aluminides, and are free from any apparent discontinuity at the interfaces, and in this respect, they presented a functional graded coating structure [26]. Formation sequence of iron aluminides according to their free energies from low to high is given as; $Fe_2Al_5 > FeAl_3 > FeAl_2 > FeAl > Fe_3Al$. Since Fe_2Al_5 has the lowest free energy, it is the first phase formed during the initial immersion of the HDA process [27]. In the SA process, on the other hand, the dissolution of the elements to the melt and the formation of Fe_2Al_5 layer take place simultaneously during the induction heating lasting 20 s. As the diffusion continues during the induction heating towards the inner layers, where Al content gradually decreases, the FeAl layer secondly forms, and finally α-Fe (Al) forms. The formation of α-Fe (Al) is attributed to the fact that Al is a ferrite forming element. Since Si atoms are present in the molten bath in the HDA process, and Si has been already detected in the EDS analysis, a Si containing phase such as $FeAl_2Si$ is also expected [28], which will be shown later by EBSD analysis along with the presence of Fe_2Al_5. In this context, the ML and IL layers of the HDA and SA samples are almost identical. It was

observed that Fe_2Al_5 and $FeAl_2Si$ phases formed a uniform structure together in the OL of the HDA sample, while a lamellar structure of Fe_2Al_5 was observed in the OL of the SA sample.

3.4.2 XRD and EBSD characterizations

XRD analysis are indicated in Fig. 3.3 of both aluminized sample and consistent with EDS results. There are common phases of both samples which are Fe_2Al_5 and FeAl. The HDA sample contains also $FeAl_2Si$ phase which is distributed very closely with Fe_2Al_5 in the microstructure which could be realized with EBSD color maps as indicated in Fig. 3.4.

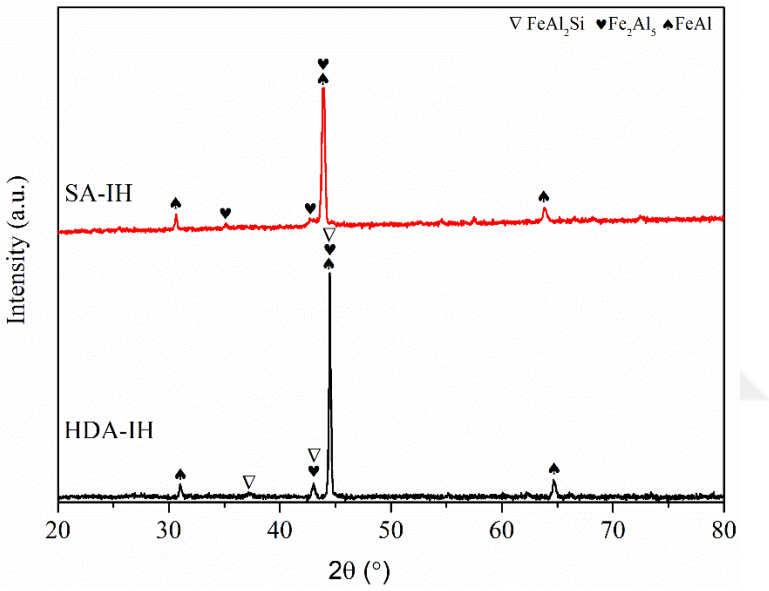

Figure 3.3 : XRD patterns of the HDA and SA samples.

In the HDA sample, the presence of $FeAl_2Si$ phase, in conjunction with the Fe_2Al_5 phase, was observed. While the OL in the HDA sample appeared as smooth and single phase layer in the SEM micrograph, $FeAl_2Si$ phase was observed in the XRD analysis, and its morphology and orientation were determined in the EBSD analysis. In the study of Cheng et al. [29], Fe_2Al_5 and $Fe_2(Al,Si)_5$ phases were formed when the samples were annealed at 750 °C for 48 h after the HDA process, which was similar to the morphology of the OL of the HDA sample in the present study. EBSD color map of the SA sample revealed that OL is not only composed of Fe_2Al_5, but also FeAl is present as indicated in Figure 3.4d. In the present study, it was found that different aluminizing methods showed a major difference in the microstructure of the OL, but not in the ML and IL. In the inverse pole figure (IPF) maps obtained from EBSD, it

was seen that texturing was observed in the 001 and 101 directions of the OL of SA sample. This is consistent with the color maps, because the Fe_2Al_5 phase mostly formed in the 001 direction, which is the characteristic texturing for Fe_2Al_5. This phase grows in the 001 direction because it has orthorhombic crystal structure, and Al atoms diffuse most rapidly in this direction [30].

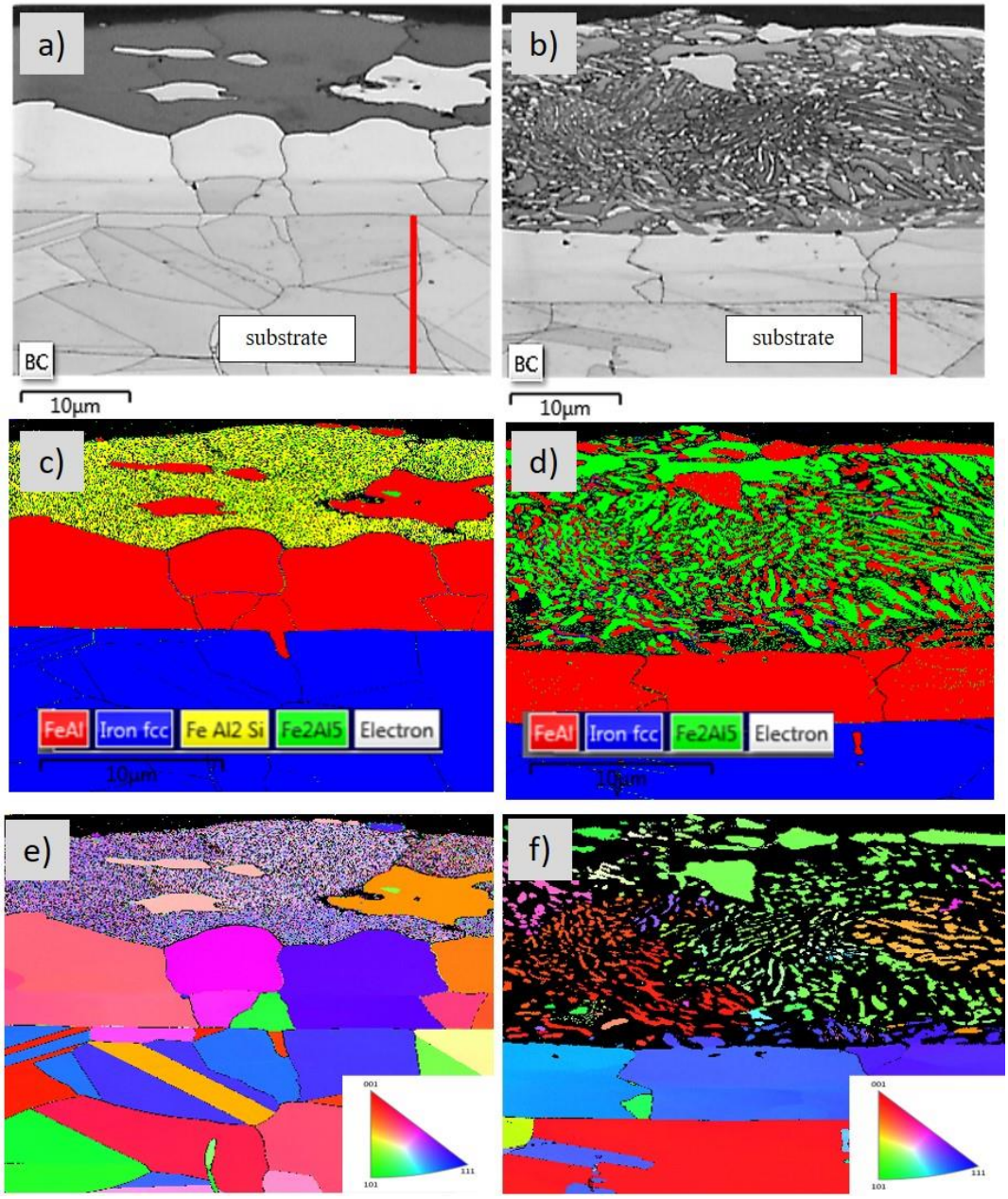

Figure 3.4 : EBSD analysis of aluminized coatings: (a, b) band contrast maps, (c, d) phase maps, (e, f) inverse pole figure (IPF) maps for HDA and SA samples, respectively.

The OL of the HDA sample is formed by the sequential arrangement and uniform distribution of $FeAl_2Si$ and Fe_2Al_5 phases in very fine submicron sizes. Due to their

low sizes, it is not possible to observe the texturing in the magnification performed by EBSD. The ML and ILs of both samples have similar structures, both are colored the same (in red color) in the color maps. In the phase diagram pertaining to the Fe-Al system, the FeAl phase is characterized by a B2 structure, while the α-Fe (Al) phase is defined by an A2 structure. Both of these phases are derived from the body-centered cubic (bcc) lattice and can persist over a broad spectrum of compositions. Consequently, EBSD measurements were insufficient to distinguish between these two distinct phases, which possess an identical lattice structure and exhibit comparable lattice parameters (FeAl ¼ 2.91 Å and α-Fe (Al) ¼ 2.86 Å) [25].

3.4.3 Nanoindentation

Loading and unloading curves of the aluminized samples, and the substrate are presented in Fig. 3.5. Indentation hardness and Young's modulus of each coating layer and the substrate were calculated by the Oliver Pharr method [17], and elastic recovery of the samples was determined by Eq. (3.1). The calculate values are given in Table 3.1. In both aluminizing methods, there was a decrease in the hardness from the surface to the substrate, depending on the formation of various aluminides and α-Fe layers due to the decreasing Al content. It presents a functional graded effect, reduces the delamination of the coating by reducing the stress concentration and the driving force for the crack formation. The hardness of OL and ML of the SA sample are higher than those of the HDA sample due to the morphological and structural differences as already discussed in the previous subsection. The hardness of IL of both samples are quite similar, as expected, because they have the same structures of α-Fe (Al), and the morphologies. However, α-Fe layers are two times higher than the substrate γ-Fe (austenitic 316L SS). This is attributed to the fact that α-Fe (Al) crystal structure creates lattice distortion in γ-Fe region, and α-Fe (Al) was strengthened by solid solution strengthening by Al. These two factors make α-Fe (Al) more strengthened than γ-Fe after aluminizing of 316L SS [31]. Young's modulus of the coating layers was calculated to be in the range of 207 - 230 GPa. There was not a clear correlation among the Young's modulus, the coating layers and the aluminizing process. However, it is noted that the coating layers have 3.5 to 15 % higher Young's modulus than that of the substrate. On the other hand, elastic recovery means that the ability of material returns to its original shape when the applied force is removed [32]. The SA

sample has a higher elastic recovery value than the HDA sample (Table 3.1). It can be concluded that the values of hardness and elastic recovery are highly influenced by the local microstructural, chemical and morphological features.

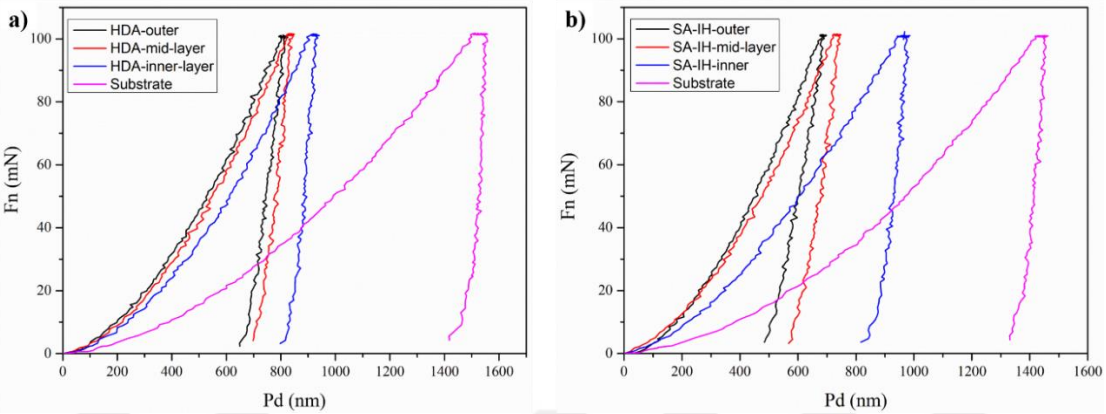

Figure 3.5 : Load–unload curves obtained by nanoindentation: (a) HDA, (b) SA.

Table 3.1 : Nanoindentation test results of the HDA and the SA samples.

Coating Layers	H (GPa)		Elastic Recovery (%)		Young's Modulus (GPa)	
	HDA	SA	HDA	SA	HDA	SA
Outer Layer	7.9 ± 0.2	13.2 ± 0.2	14.9	24.3	210	207
Mid-layer	6.9 ± 0.7	9.6 ± 0.4	13.0	15.2	225	231
Inner-layer	5.5 ± 0.1	4.9 ± 0.4	9.4	9.2	228	221
Substrate	2.2 ± 0.3	2.2 ± 0.1	4.6	5.6	199	199

3.4.4 Wear test

The wear track profiles, as illustrated in Fig. 3.6, demonstrated that the SA sample exhibited a reduced wear loss in comparison to the HDA sample, with both aluminized samples have significantly lower wear loss than the substrate. The wear rates of the samples were calculated in the unit of mm^3/Nm as mentioned in Section 2.4. They showed that the HDA and the SA samples have almost 7 and 10 times higher wear resistance (in terms of reciprocal of the wear rate) than the substrate, respectively. Also, the SA sample has an approximately 50% higher wear resistance than the HDA sample. It is well known that wear resistance can be influenced by hardness and Young's modulus. Elastic recovery can also affect the wear rate because higher elastic recovery reduces plastic work [33]. In the present study, hardness and elastic recovery varied depending on the location of the coating layers and the aluminizing process, while the calculated values of Young's modulus did not exhibit a clear correlation with the coating layer and the type of aluminizing process, as stated earlier.

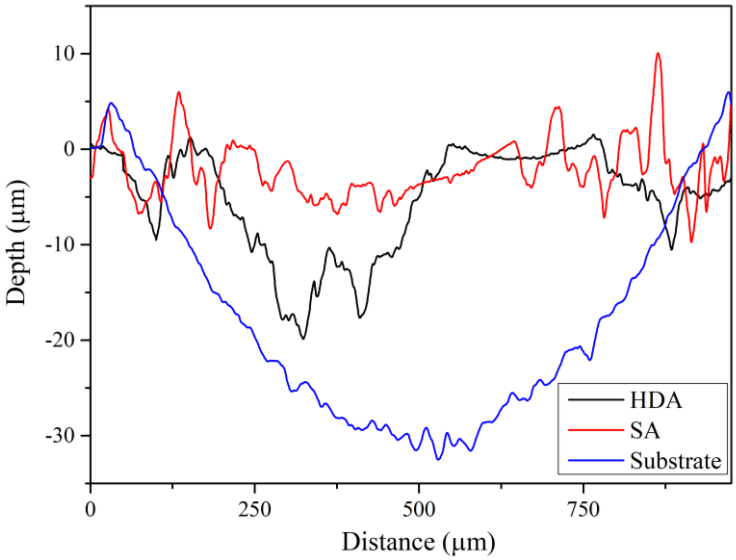

Figure 3.6 : 2-D profilometer of the wear track of the samples.

When the maximum depth in the wear tracks for both samples is considered, it is seen that this is almost 7 μm in the SA sample, and 20 μm in the HDA sample. This shows that the counter face ball of the wear test remained in the coating layer during the wear test of the SA sample (with approximately 12 μm thick OL), while it reached up to the mid layer in the HDA sample (with approximately 17 μm thick OL). Therefore, higher wear resistance of the SA sample can be reasonably correlated to both its higher hardness (Fig. 3.7a) and higher elastic recovery (Fig. 3.7b) in the OL. These figure shows a reasonable trend between the wear rate, hardness and elastic recovery, i.e. as the hardness and elastic recovery increase, the lower is the wear rate. In other words, increasing hardness and elastic recovery increases wear resistance. Keeping in mind that both hardness and elastic recovery affect the wear rate, in order to obtain a more clear correlation among them, we combined these two important surface related properties in terms of ratio of hardness to elastic recovery. As seen in Fig. 3.7c, this ratio (hardness to elastic recovery) reveals a clear linear correlation with the wear rate giving a high correlation coefficient *(R^2=0.9978)*. When the ratio of hardness to elastic recovery increases, the higher is the wear resistance. The unit of this ratio is Nmm/mm^3, which is the unit of toughness as energy consumed per unit volume. This emphasizes that the wear rate can be correlated by toughness, which can be determined by hardness and elastic recovery in the indentation tests. This also implies the fact that lamellar morphology of the outer layer in the SA sample has a higher hardness to elastic recovery ratio, in turn, results in a higher wear resistance than the HDA samples with almost equal thickness and phase content.

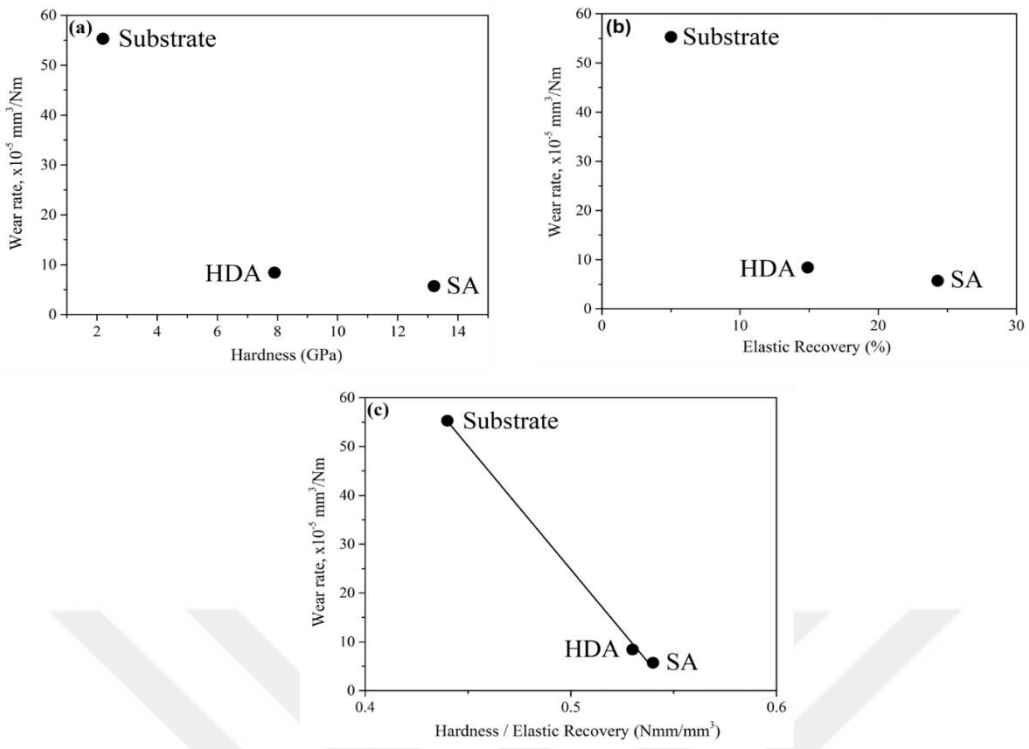

Figure 3.7 : Correlation between (a) hardness, (b) elastic recovery, and (c) hardness/elastic recovery ratio with wear rate.

Another significant aspect can be ascribed to the lamellar morphology of the SA coating, which augmented wear resistance, as the toughness of the coating was enhanced by the lamellar structure, as evidenced by the research conducted by Gao et al. [34]. Additionally, lamellar structures impede the initiation of cracks and contribute to superior wear resistance by complicating the propagation of cracks [35]. It can be inferred that the toughness of the coating on the SA sample exceeds that of the HDA sample, as the elastic recovery of the SA sample is superior to that of the HDA sample [33]. This should also be noted that, in stainless steel aluminizing, the coating morphology can have a significant effect in addition to coating composition, and the SA process that can be realized within very short period of time assisted by the induction is promising in enhancing wear resistance of the stainless steels used in the present study.

Friction coefficient variation of the samples with the sliding distance are given in Fig. 3.8. The SA sample has a lower average friction coefficient compared to the HDA sample and the substrate. It should be recalled that the SA sample has a higher elastic recovery than that of the HDA sample in the outer layer. Since the total depth of the wear track is within the outer layer for the SA sample, and within outer and mid-layers for the HDA sample, the friction coefficient of the samples can also be reasonably

correlated with the elastic recovery of the layers. A higher elastic recovery means a reduced plastic deformation. Since it is very well known that one of major factors affecting friction coefficient is plastic deformation, as the plastic deformation increases, the higher is the friction coefficient [36]. Finally, the lower friction coefficient of the SA sample is correlated with its higher elastic recovery determined by the indentation tests.

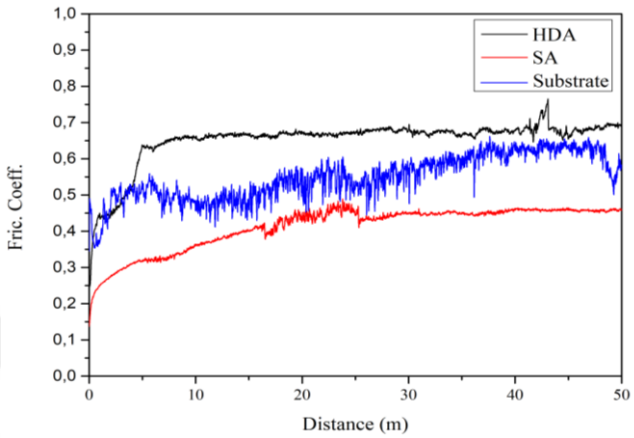

Figure 3.8 : Variation of friction coefficient with the sliding distance.

There are various aluminum coating techniques reported in the literature to enhance the surface properties of steels such as oxidation, corrosion, and wear resistance. Examples include thermal spraying, friction welding, and arc spraying welding. In the study by Riastuti et al.[37], an aluminum coating was applied to 316L stainless steel using the thermal spray method, followed by wear testing. The coating exhibited a hardness of 96 HB and a wear volume of 0.0132 mm^3, which are considerably lower than the values obtained in the present study. Similarly, in the work of Sahoo et al.[38], the surface of 316L steel was coated with an Al6063 alloy using friction welding, resulting in a relatively low hardness value of about 138 HV. In both studies, surface hardness could potentially be increased through diffusion annealing due to aluminide formation; however, this process is sometimes avoided to prevent damage to the substrate microstructure. From this perspective, the advantage of the induction heating method becomes evident it enables diffusion annealing within the coating layer while preserving the microstructure of the base material. In another study, Zhou et al.[39] coated the surface of carbon steel with aluminum using the arc spraying method. Because the as-sprayed coatings exhibited low hardness, subsequent diffusion annealing was performed at different temperatures. After annealing at 800 °C and 900 °C, aluminide phases formed, but Kirkendall porosities also developed, which

decreased the wear resistance. In the current study, due to the extremely rapid nature of induction heating, such void formation did not occur.

3.4.5 Wear track examinations

SEM images of the wear tracks are given in Fig. 3.9. It is seen that there are dark colored oxide regions on the surface of both samples in the worn surfaces. This shows that the oxidative wear mechanism is active in both samples [40]. In addition, the cracks seen in both coated samples (Fig. 3.7 b and c) show that the fatigue type wear mechanism is also active in these samples. Due to the repetitive movement of the counter ball, both thermal and mechanical stresses to which the material is exposed cause the formation of thermo-mechanical cracks. In the continuation of the test, these cracks form a network and cause delamination by separating from the surface in those areas [33,41]. In addition, the bright areas seen on the wear surface of the coated samples show that the Fe-Al based coating layer is still present on the surface. In the EDS analysis on these bright zones, there are still high amount of Fe and Al which is characteristics for the aluminide coatings. This situation is consistent with the wear track depth values determined by the surface profilometer.

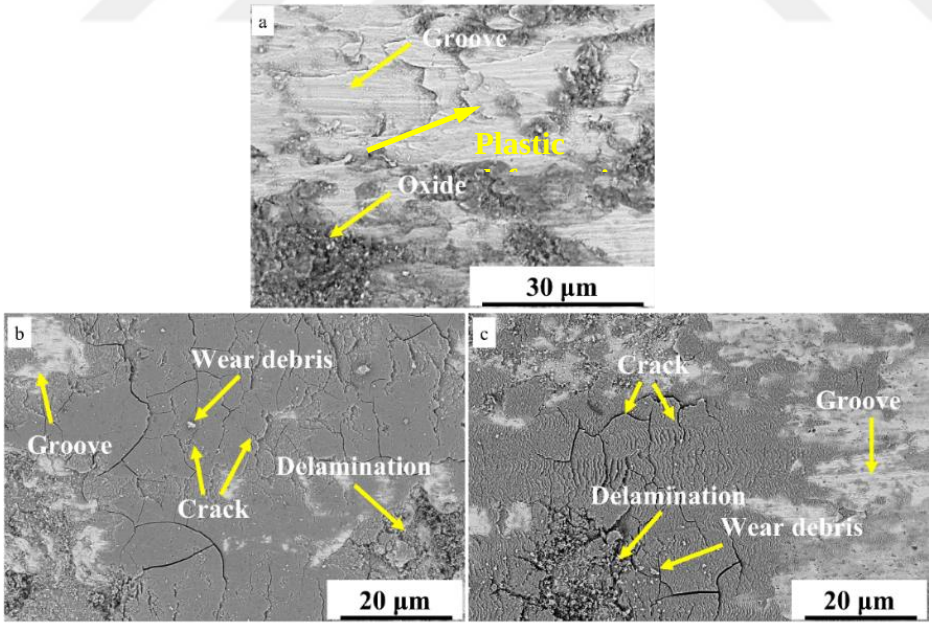

Figure 3.9 : SEM micrographs of wear tracks: (a) substrate, (b) SA, (c) HDA.

The SEM-EDS mapping analysis provides insights into the elemental composition of the worn surfaces. This analysis helps in understanding the distribution of elements such as oxygen, aluminum and iron, which are crucial for determining the phases

present on the wear surfaces. The presence of oxide regions and cracking patterns suggests that both oxidative and fatigue wear mechanisms significantly influence the wear behavior of the coatings. These findings highlight the complex interactions between mechanical and chemical processes during wear. In addition, the groove structure seen in the light-colored areas of the samples shows that the abrasive wear mechanism caused by plastic deformation is also effective. The presence of plastic deformation marks on the wear surface of the high hardness brittle Fe-Al based intermetallic phases obtained after the coating process is due to the presence of ductile FeAl intermetallic in the coating layer.

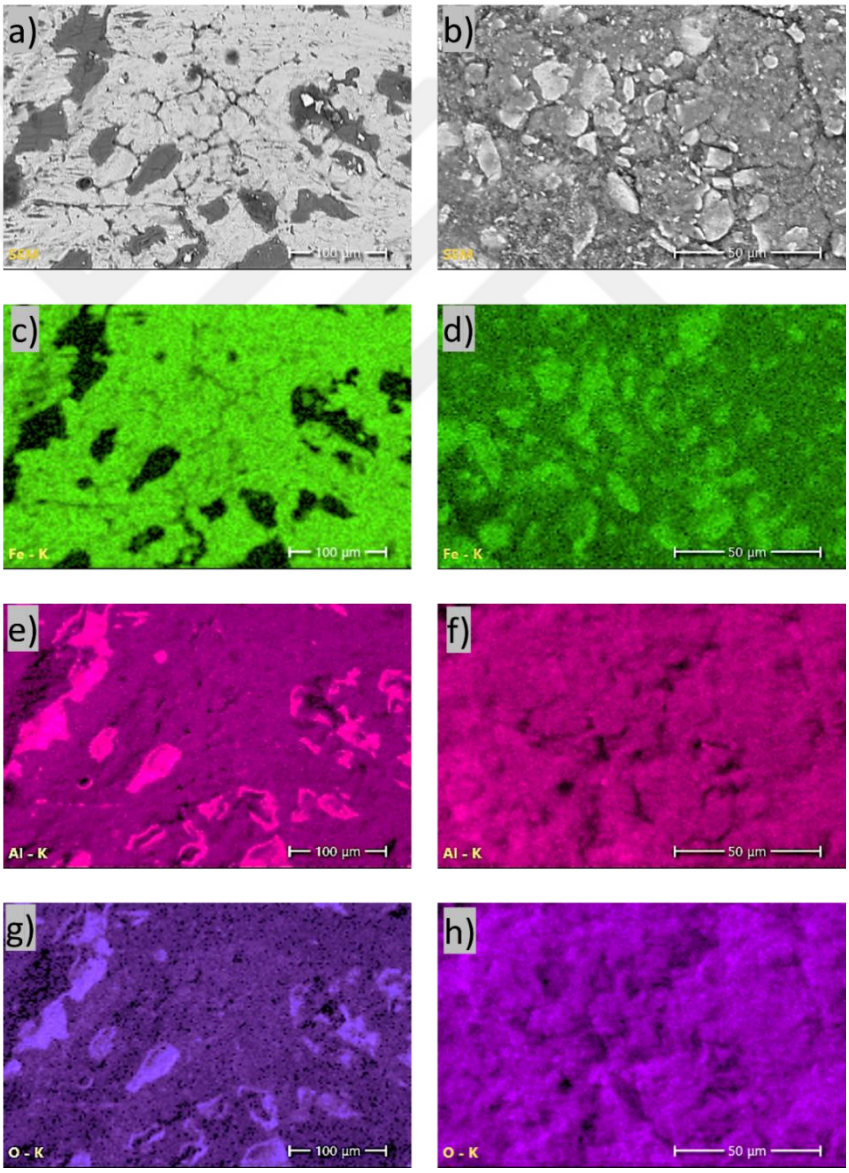

Figure 3.10 : EDS mapping analyses of the wear tracks for aluminized samples: (a) SEM image of the HDA sample, (b) SEM image of the SA sample, (c–e) elemental mappings of Fe, Al, and O for the HDA sample, (f–h) elemental mappings of Fe, Al, and O for the SA sample.

Figure 3.10 shows the EDS mapping analyses in the wear tracks of the SA and HDA samples. In both samples, Al and O elements are intensely present in the regions defined as oxides, which are seen as dark regions in the wear tracks. In addition to Al and O, Fe and Cr also exist in these oxide regions for the both samples.

3.4.6 Oxidation tests

Figure 3.11 shows the evolution of the specific weight change (weight change per unit area of the sample) of the 316L substrate, the SA and the HDA samples after 100 h of isothermal exposure at 1000 °C in air. Since oxide layer formation on the sample increases its weight, a lower weight change indicates a higher oxidation resistance. It is noted that the specific weight changes were very low for the aluminized samples, in particular, 2.5 mg/cm^2 in the SA sample, and 2 mg/cm^2 in the HDA sample. This shows that aluminizing process regardless of the process type significantly enhances the oxidation resistance of the 316 SS (with a weight loss of 200 mg/cm^2). In conventional high-temperature oxidation tests, surface oxide formation typically results in a measurable weight gain, and the oxidation resistance is commonly assessed on the basis of this increase. In contrast, during the present study, the oxides generated on the surface exhibited poor adherence and spalled off in a scale-like manner, leading to a net weight loss rather than the expected weight gain. In the study conducted by Lakakh et al., the high-temperature oxidation test of Cr/Ni austenitic stainless steel revealed a net weight loss, as oxide scales spalled off from the surface. Consequently, the oxidation resistance was evaluated on the basis of this weight loss [42].

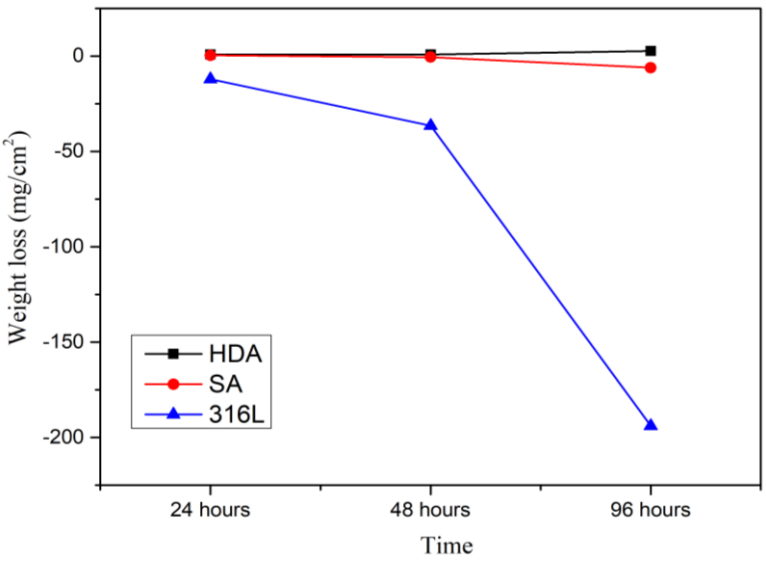

Figure 3.11 : Variation of the weight change with time after the oxidation tests.

Figures 3.12 present the cross sectional SEM micrographs after isothermal oxidation tests. The results indicate a progressive increase in coating thickness with prolonged oxidation exposure. Specifically, in the HDA sample, the initial coating thickness of 35 μm increased to 65 μm after 24 h of exposure, and further increased to 230 μm after 96 h as indicated in Fig. 3.12a and 3.12b. On the other hand, in the SA sample, the coating thickness increased from 35 μm to 130 μm after 24 h of exposure, and reached 400 μm after 96 h as indicated in Fig. 3.12c and Fig 3.12d. This increase in thickness suggests that the oxidation process facilitated diffusion-driven layer growth, resembling the effects of diffusion annealing.

As mentioned above, during the thermal oxidation tests conducted at 1000 °C, Al atoms within the aluminide phases such as Fe_2Al_5 and FeAl in the coating layer tended to diffuse inward, gradually forming aluminide phases richer in iron and eventually reaching the α-Fe(Al) phase. Since the thermal oxidation test acts as a kind of diffusion annealing, an increase in coating thickness occurred in the samples, and these increases differ between SA and HDA specimens. The results show that the SA sample exhibits a higher coating thickness than the HDA sample, and this difference is believed to stem from two main reasons. First, as revealed by the EBSD analysis results, the SA sample contains more phase boundaries, which provide greater pathways for atomic transfer; therefore, Al diffusion is expected to be more pronounced in the SA sample [43]. Second, the HDA process takes place in an Al–Si bath, and this is thought to be related to the diffused Si atoms. HDA processes are typically performed in Al–Si baths because Si atoms lower the eutectic temperature. Si atoms occupy the (001) plane in the Fe_2Al_5 crystal structure, and the Si atoms located on this plane restrict the diffusion of Al atoms [44]. Consequently, Si-containing HDA processes tend to result in relatively thinner coating layers. Similarly, during the oxidation test, the existing Si atoms within the aluminide phases are believed to limit Al diffusion, leading to a thinner coating in the HDA sample compared to the SA sample.

Additionally, the oxidation tests led to the formation of porosities within the coating with the porosity level increasing with the increase in the oxidation time. This porosity formation is attributed to the development of Kirkendall voids, which arise due to differences in the diffusion coefficients of various phases during phase transformations within the coating layer. For both samples, no oxide formation was observed after 24 hours of oxidation testing. However, after 96 hours, oxide formation was detected on

the surface at levels of approximately 5–10 μm, which was identified as alumina based on the EDS analysis results shown in Fig. 3.12f. Additionally, in the higher-magnification image of the HDA96 sample in Fig. 3.12e, $Fe_3(Cr,Ni)Al$ islands were observed within the α-Fe(Al) matrix. These observations indicate that phase transformations continuously occurred during the oxidation test. As the test progressed, Fe-rich aluminide phases formed and, by the end of 96 hours, these Fe-rich aluminides had transformed into α-Fe (Al), while some $Fe_3(Cr,Ni)Al$ phases that had not yet converted to α-Fe (Al) remained in the structure. XRD analysis (Fig. 3.13) confirmed that the Fe_2Al_5 and FeAl phases, which were initially presented before the oxidation tests, were almost not detected after the tests.

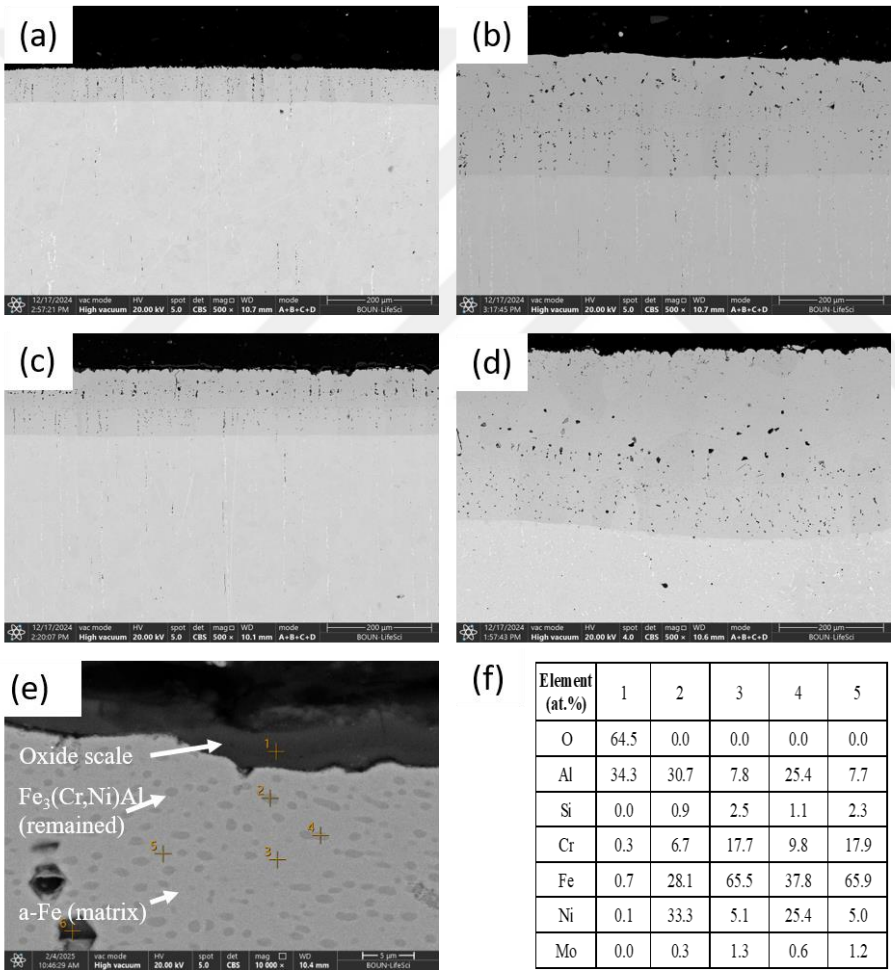

Element (at.%)	1	2	3	4	5
O	64.5	0.0	0.0	0.0	0.0
Al	34.3	30.7	7.8	25.4	7.7
Si	0.0	0.9	2.5	1.1	2.3
Cr	0.3	6.7	17.7	9.8	17.9
Fe	0.7	28.1	65.5	37.8	65.9
Ni	0.1	33.3	5.1	25.4	5.0
Mo	0.0	0.3	1.3	0.6	1.2

Figure 3.12 : Cross-sectional SEM images after oxidation tests: (a) HDA-24 h, (b) HDA-96 h, (c) SA-24 h, (d) SA-96 h, (e) higher magnification of HDA-96 h, (f) corresponding EDS analysis.

Fig. 3.13 shows the XRD analysis results after oxidation tests. It was observed that the Fe_2Al_5 and FeAl phases in the structure before the test were almost completely transformed into α-Fe (Al) phase even after 24h. As mentioned earlier in Section 3.1,

the oxidation test functioned almost like diffusion annealing and provided phase transformation. Alumina peaks were also observed after 96 h, as a thin alumina layer was observed on the surface by EDS mapping analysis (Fig. 3.12f).

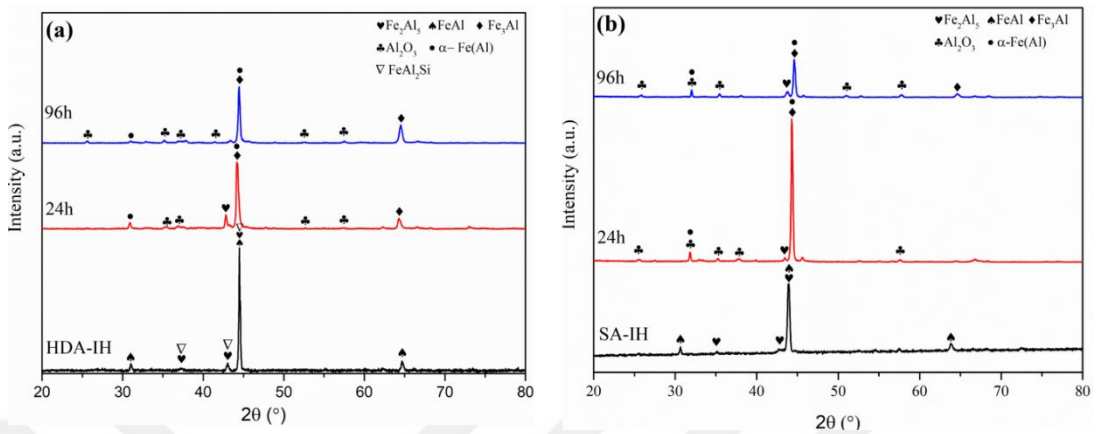

Figure 3.13 : XRD analysis results after oxidation tests; a) HDA and b) SA.

Fig. 3.14 shows a schematic representation of the results of the oxidation tests. The phase transformations, morphology changes and layer thicknesses of the coating layers after the application of aluminizing processes, induction heat treatment and oxidation tests are schematized to summarize the entire test procedure. HDA sample surface shows melt aluminum residue and aluminum-rich iron aluminide layer formed during the hot dip process (Figure 3.14a). On the SA sample surface (Figure 3.14b), there is a layer of aluminum held by physical bonding. After the induction heating, both samples have similar inner and middle layers and the outer layers are different (Figure 3.14c and d). Figure 3.14e, f, g and h show the microstructure after 24 and 96 h oxidation tests and schematize that the matrix is α-Fe (Al) and the thickness of the coating layer increases with increasing time.

Oxidation tests revealed that the HDA and SA samples exhibited significantly improved oxidation resistance, because there is not observed any iron oxide formation at the surface, only thin adherent Al_2O_3 (aluminum oxide) layer was occurred. Al_2O_3 is more stable than Cr_2O_3, therefore, it can resist to aggressive environment more than Cr_2O_3. Unlike the findings of Xi et al. [45], where a double oxide film structure (Fe_2O_3 in the outer layer, $FeCr_2O_4$ in the inner layer) was observed at 316L surface after oxidation test. This indicates that the oxidation mechanism in HDA and SA oxidized samples are predominantly governed by the formation of stable Al_2O_3 layers, providing effective protection against high-temperature oxidation.

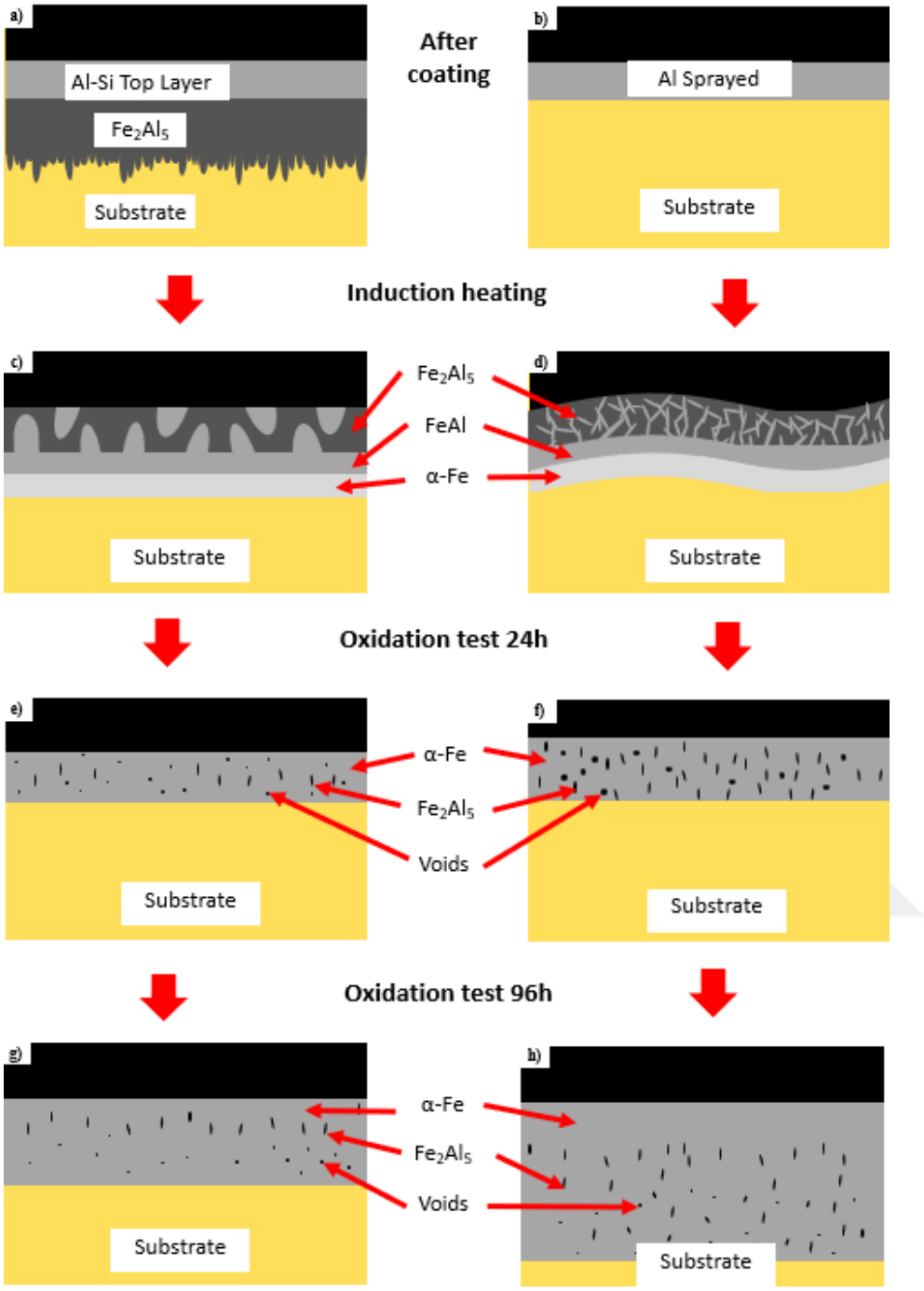

Figure 3.14 : Schematic representation of coating evolution before and after oxidation: (a,c,e,g) HDA and (b,d,f,h) SA samples.

3.5 Conclusions

In this study, the wear and high-temperature oxidation behaviors of AISI 316L SS were comprehensively investigated after being coated via two different aluminizing methods HDA and SA followed by a short-duration induction heat treatment at 1000 °C for 20 s. The aim was to evaluate the effectiveness of short-time induction heating as an alternative to conventional diffusion annealing and to compare the

resulting microstructural, mechanical, and tribological performance of both coating methods. The results revealed that both aluminizing techniques formed functional gradient aluminide layers composed primarily of Fe_2Al_5, FeAl, and Fe(Al) phases. However, the outermost layer morphology and mechanical performance differed significantly depending on the coating method. The SA samples developed a lamellar Fe_2Al_5-rich outer layer with significantly higher hardness (13.2 GPa) and elastic recovery compared to the smoother $FeAl_2Si$-rich outer layer of the HDA samples. Nanoindentation and wear tests revealed that the ratio of hardness to elastic recovery can be well correlated with the wear rate with a high level of correlation coefficient. The wear tests also demonstrated that SA-treated samples had a notably lower coefficient of friction (~0.4) and wear depth (~7 μm), as opposed to the HDA-treated ones (~0.65 and ~20 μm, respectively). This enhancement is attributed to the unique lamellar microstructure induced by the slurry process and rapid diffusion via induction heating, which together hinder crack initiation and propagation under cyclic loading. Oxidation experiments conducted at 1000 °C for up to 96 h showed that both coatings effectively suppressed the formation of iron oxides and facilitated the transformation of intermetallic phases into a protective α-Fe (Al) matrix. A very thin, adherent Al_2O_3 layer was consistently observed on the surface of both SA and HDA samples, functioning as a diffusion barrier and significantly enhancing oxidation resistance. Notably, SA coatings reached a greater final thickness (400 μm) after oxidation due to more extensive phase transformation and diffusion-driven growth. The combination of slurry aluminizing and short-term induction heating emerges as a promising surface modification strategy for SSs exposed to high temperatures. It offers a high-performance, energy-efficient, and time-saving alternative to conventional thermal treatments. Moreover, the ability to form graded coatings with tailored mechanical and oxidation-resistant properties positions this technique as a strong candidate for future applications in harsh service environments, such as petrochemical reactors, turbine components, and high-efficiency heat exchangers. In conclusion, this work not only establishes the superior performance of the SA process assisted with the induction heating in terms of wear and oxidation resistance, but also underlines the potential of integrating advanced rapid heating technologies with conventional coating methods to engineer robust and multifunctional surface layers on austenitic SS. Future studies may explore scalability of the proposed process to a larger products, long-term cyclic oxidation behavior, and compatibility with other alloy systems.

4. INDUCTION ASSISTED HOT-DIP AND SLURRY ALUMINIZING OF INCONEL 718[2]

4.1 Introduction

IN718, a Ni-Fe based superalloy, is widely used in high-temperature applications such as gas turbines and aerospace engines due to its excellent mechanical properties and stability. During use at high temperatures, oxidation resistance is also required to ensure longevity of the superalloy [46–48]. Therefore, various thermochemical based surface modification techniques have been adapted to improve its oxidation resistance. Aluminizing is one technique using for this purpose, which is based on the formation of aluminide layers on the surface. Because this method is a thermochemical treatment controlled by diffusion, temperature and time are the key parameters to determine the type and morphology of the aluminide layers [48,49].

Aluminizing can be applied in liquid (hot-dip aluminizing), solid (slurry or pack aluminizing), or gaseous environments (chemical vapor deposition), which have some advantages and disadvantages over each other. Hot dip aluminizing (HDA), slurry aluminizing (SA), and pack aluminizing (PA) are more economical methods than chemical vapor deposition (CVD), which requires a highly sophisticated equipment [49–51]. In HDA process, a substrate is immersed into a molten aluminium bath containing pure Al or Al-Si alloy for relatively short time (less than 10 min), and intermetallic compound containing aluminium, called aluminide, is formed on the surface. Slurry aluminizing uses a mixture containing aluminium particles and a binder, called slurry, which is sprayed onto the substrate surface. This method is advantageous due to its ability to produce uniform coatings with good adhesion and controlled thickness in large parts [52].

[2]This chapter is based on the article: Karakas, A., Balci, E. and Baydogan, M. (2025). Induction Assisted Hot-Dip Aluminizing of Inconel 718, Mater. Res. Express 12 (2025), https://doi:10.1088/2053-1591/ae22c5

Types of aluminide phases mainly depend on the main elements coming from the substrate itself, and their stoichiometry is related with the aluminizing parameters such as temperature, time and aluminizing methods as well as distance from the substrate-coating interface. For example, in a nickel base alloy, as in this study, nickel aluminides with different stoichiometry ($NiAl_3$, Ni_2Al_3, NiAl or Ni_3Al) are formed [53]. Depending on the diffusivity of Al and Ni, aluminizing processes can be called a high activity or low activity aluminizing. In a high activity aluminizing in Ni-based alloys, inward diffusion of Al takes place and aluminium rich aluminides are formed, while a low activity aluminizing encourages the formation of Ni-rich aluminides due to outward diffusion of Ni. Similarly, aluminizing of a steel produces iron aluminides such as $FeAl_3$, Fe_2Al_5 and FeAl [54]. Previous studies have shown that HDA can significantly enhance the lifespan of Ni-based alloys in harsh environments [55,56]. SA process is also very effective to enhance oxidation resistance improving high-temperature performance of Ni-based alloys [52,57].

Since the SA process, being a sprayed method, is performed at room temperature, the slurry is not transformed into aluminide just after the spraying. Therefore, it needs performing a further diffusion annealing after spraying to be able to form aluminide on the surface. On the other hand, aluminides can even form during HDA because the process is already performed in a molten aluminium bath at an elevated temperature. However, in this process, some Al may remain untransformed on the surface due to immersion in the molten bath, which also requires further diffusion annealing to be transformed into aluminides.

Conventional diffusion annealing methods, typically involving furnace heating, require long heating times up to several hours. It is time-consuming and energy-intensive, and might affect the substrate's microstructure during long term holding at an elevated temperature. To overcome these shortcomings, recent advancements have introduced induction heating as an alternative diffusion annealing method. It utilizes electromagnetic fields to directly heat the material, resulting in a rapid temperature increase and focuses energy directly on the material, minimizing heat loss to the surroundings. It offers several advantages over conventional furnace heating, including faster heating rates, better energy efficiency and local heating within seconds [47,58,59]. The shorter processing time and precise temperature control of induction heating result in reduced thermal exposure of the substrate [58–60].

Previous studies concerning induction heating have shown that it can enhance the diffusion kinetics and improve the microstructural characteristics of aluminide coatings on different materials. Several studies have compared the performance of induction heating with conventional furnace heating. For instance, Hu et al [60] performed pack chromizing of AISI 5140 steel using induction and furnace heating in comparison with each other. They reported that induction heating provided a thicker coating, a stronger interface and better wear properties than those obtained with conventional furnace chromizing. Takesue et al [61] used in gas blow induction heating (GBIH) in nitriding of a Ti6Al4V alloy to heat the sample. They found that nitrogen diffusion layer could be obtained in a short time and surface hardness increased with the increase in the process temperatures. In a recent study by Bauer et al [62], Alloy 800 was diffusion annealed by induction heating at a temperature range of 700 and 1000 °C after slurry aluminizing. They reported that (Fe,Cr,Ni)Al diffusion coatings could be formed for all temperatures on the surface with their relative thickness changing depending on the temperature.

Summarized works in the literature revealed that induction heating has been used as a fast heating method in various applications, and make it a promising technique for the diffusion annealing after aluminizing. On the other hand, little work has been devoted to induction heating for the purpose of diffusion annealing of an aluminized sample. This work, therefore aimed to demonstrate effect of fast induction heating by comparing the characteristics of two competitive aluminizing process, namely HDA and SA processes on the elementel distributions, types of the formed phases, and integrity of the interfaces between the coating layers on IN718 superalloy.

4.2 Experimental Methods

4.2.1 Hot dip and slurry aluminizing

IN718 round bars, whose nominal chemical composition was given in Table 4.1, were used in the present study. The bars supplied in AMS 5662 condition with the diameter of 30 mm, and were cut into 15 mm thick round samples.

Table 4.1 : Chemical composition of IN718 substrate.

Elements	wt. %
C	0.08
Mn	0.25
Cr	18.24
Si	0.23
S	0.002
P	0.004
Fe	16.29
Mo	3.01
Co	0.8
Nb	5.27
Ti	0.83
Al	0.87
Ni	Balance

The samples were divided into three groups for the following processes. The first group was only hot dip aluminized (referred as HDA sample). The second group was hot dip aluminized followed by induction heating (referred as HDA+Induction sample). The third group was slurry aluminized assisted by induction heating (referred as SA+Induction sample). Because the coating cannot form just after spraying the slurry without the induction heating, there is no sample group that can be addressed as "SA sample".

Prior to the aluminizing processes, the surface was ground first with 320 grit sandpaper for 2 min, ultrasonically cleaned in ethanol for 5 min and then rinsed with acetone. For the HDA process, the samples were immersed in a graphite crucible filled with molten Al-11 wt. % Si alloy at 700 °C for 9 min and pulled out from the molten bath and cooled in still air to the room temperature. For the slurry aluminizing, the slurry was prepared as composed of a binder solved in a solvent (55 wt.%) and microparticles of aluminum (45 wt. %) with an average size of 30–35 μm (Nanografi, 99.9 % pure). The solvent was a mixture of polyvinyl butyral (PVB) and methyl ethyl ketone with a mass ratio 1:10. All components were mixed in a beaker with a magnetic stirrer system for 1h. The mixture was then ball milled for 24 h to obtain the slurry. The slurry was then sprayed with an airbrush to the samples, and then allowed to dry in ambient air. The amount of slurry sprayed was 24 mg/cm^2. It was determined by weighing the sample before and after the slurry application. After the induction heating, there was a little

particulate material seen on the SA sample. It was easily removed from the surface by a gentle air spraying before further characterization works.

4.2.2 Induction heating

Induction heating equipment (model RT-380M50, manufactured by Reterm Induction Heating Limited, TUR) with a maximum power of 50 kW and maximum frequency of 20 kHz was used as the heat source for diffusion annealing (Figure 4.1).

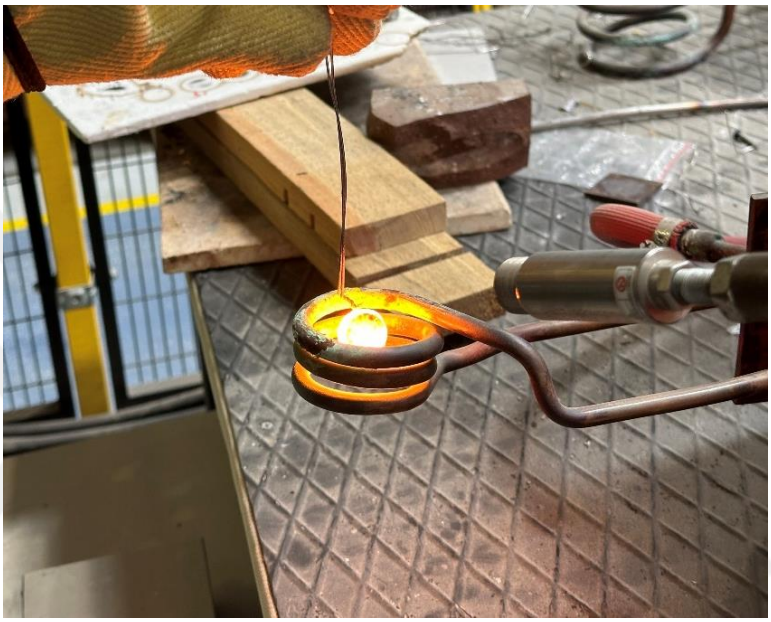

Figure 4.1 : General view of induction heating.

Depending on the shape and size of the samples, the appropriate helical coil was used, and the distance between the coil and the sample was 10 mm. The induction coil was being cooled with water circulating system during the heating to prevent overheating. The induction current was set to heat the sample from room temperature to 1000 °C with a heating rate of 50 °C/s. The temperature was measured by a pyrometer. After reaching the desired temperature, the coated samples were hold at this temperature for 20 s, and cooled in air to the room temperature.

4.2.3 Characterization

After the aluminizing and diffusion annealing processes by the induction heating were completed, cross sections of the samples were mounted in bakelite, ground by emery papers and polished with 1 μm diamond paste using the conventional procedure, and etched with Kalling 2 solution (5 g $CuCl_2$ + 100 mL HCl + 100 mL ethanol) for 10 s. Microstructural examinations were conducted using a scanning electron microscope

(SEM – Thermofisher Quatro) operating at 25 kV, equipped with an X-ray energy-dispersive spectroscopy (EDS) detector. Electron backscattered diffraction (EBSD) analysis was conducted on an SEM (Tescan MAIA3 XMU) equipped with an EBSD detector operating at 20 kV and 6.4 nA with a step size of 0.09 μm, Qualitative phase analysis was made by an X-ray Diffractometer (XRD) using a Rigaku D-Max 2200 PCI device (Cu Kα radiation, λ = 0.15418 nm) between 2θ angles of 20 and 90° with a scanning rate of 2 °C/min.

4.3 Results and Discussion

4.3.1 Hot dip aluminizing (HDA sample)

Figure 4.2a shows cross sectional SEM micrograph of the HDA sample without the induction heating. Total coating thickness is 120 μm, and the substrate coating interface is flat indicating a uniform dissolution and interdiffusion along the interface, which immediately start just after the immersion. It also indicates that the coating has three separate layers, namely, the outer layer, the mid-layer, and the inner layer (interdiffusion layer, IDL). The outer layer is 35 μm thick. Although mostly Al and Si occupy the outer layer as shown by the line EDS analysis (Figure 4.2b) performed along the entire coating, the outer layer does not have the characteristic microstructure of Al-11 wt. % Si alloy forming the molten bath. It shows that dissolution and diffusion have already affected the outer layer and result in the redistribution of the elements Beside the line EDS analysis, EDS mapping analyses were also performed to demonstrate the elemental distribution along the coating. Figure 4.2c and d clearly show the accumulation of Al and Si near the surface with the former was significantly higher. This is attributed to that Si has a higher melting point (1414 °C) than Al (660 °C), and therefore its inward diffusion is less likely with respect to that of Al at a lower temperature [63]. These elements also exist in the entire coating in a decreasing amount as compared to the surface. On the other hand, while Cr and Fe were present in the substrate with approximately 18 wt. % and 16 wt. %, respectively, their contents were approximately 6-10 at. % for each in the mid- and inner layers of the coating while their contents are lower in the outer layer. In contrast, Ni spots in the EDS mapping (Figure 4.2e) decorate mainly the outer and inner layers, leaving the mid-layer Ni deficient. It also reveals that location of Ni is completely opposite to the locations of Cr and Fe in the mid- and the inner layers, indicating that Ni is present at

the expense of Cr and Fe, and vice versa. This can be seen clearly from the EDS line analysis in Figure 4.2b as well as the EDS mapping analyses in Figure 4.2e to g. For example, at a depth of 60 μm from the surface, Cr and Fe contents are about 9 at. % where Ni content significantly drops. Similarly, at a depth of 110 μm, Ni content increases to 13.7 at. %, however, at the same point, Cr and Fe contents again exhibited a drop. Cr and Fe are the substrate elements. Presence of them in the mid- and the inner layers, and their lower amounts in the outer layer show that they could not reach to the outer layer by the outward diffusion. Instead they must have been dissolved at the beginning of the HDA process when the substrate was in first contact with the molten Al-11 wt. % Si bath. At the same time, Ni outward diffusion takes place towards the outer layer (along 120 μm of the entire coating from the substrate) leaving the mid layer Ni deficient, and relatively rich in Cr and Fe as well [64]. It is also worth noting that Cr and Si do not occupy the same locations of the coating in the HDA sample despite they both present in the entire coating. It means that these two elements do not form any silicide phase within the coating. As will be shown later by EDS mapping analyses, however, after the induction heating, Cr and Si concentrated in the same regions in the HDA+Induction sample to form a silicide phase. This clearly suggests that presence of these elements during the HDA process is not enough to form a silicide phase, and further heating is required for its formation, which will then be achieved by the induction heating in the HDA+Induction sample.

In order to further characterize the HDA coating, all three layers (the outer, the mid- and the inner layers) were examined and analyzed in detail. Higher magnification SEM micrographs of the outer layer can be characterized with black and gray areas with the latter has a lamellar morphology (Figure 4.3a). EDS point analysis (Figure 4.3b) shows that black areas contain mainly Al (91.9 at. %) with lower Si (1.3 at. %). Small amount of oxygen was also detected indicating that the elements might be oxidized during the HDA process. In the gray lamellar areas, in addition to Al and Si, substrate elements such as Ni, Cr, Fe and Nb were also detected whose contents varied depending on the location. This shows that during the HDA process, Ni, Cr, Fe and Nb coming from the substrate can exist in the outer layer with the contents of 11.8, 2.4, 1.3 and 1.1 at. %, respectively.

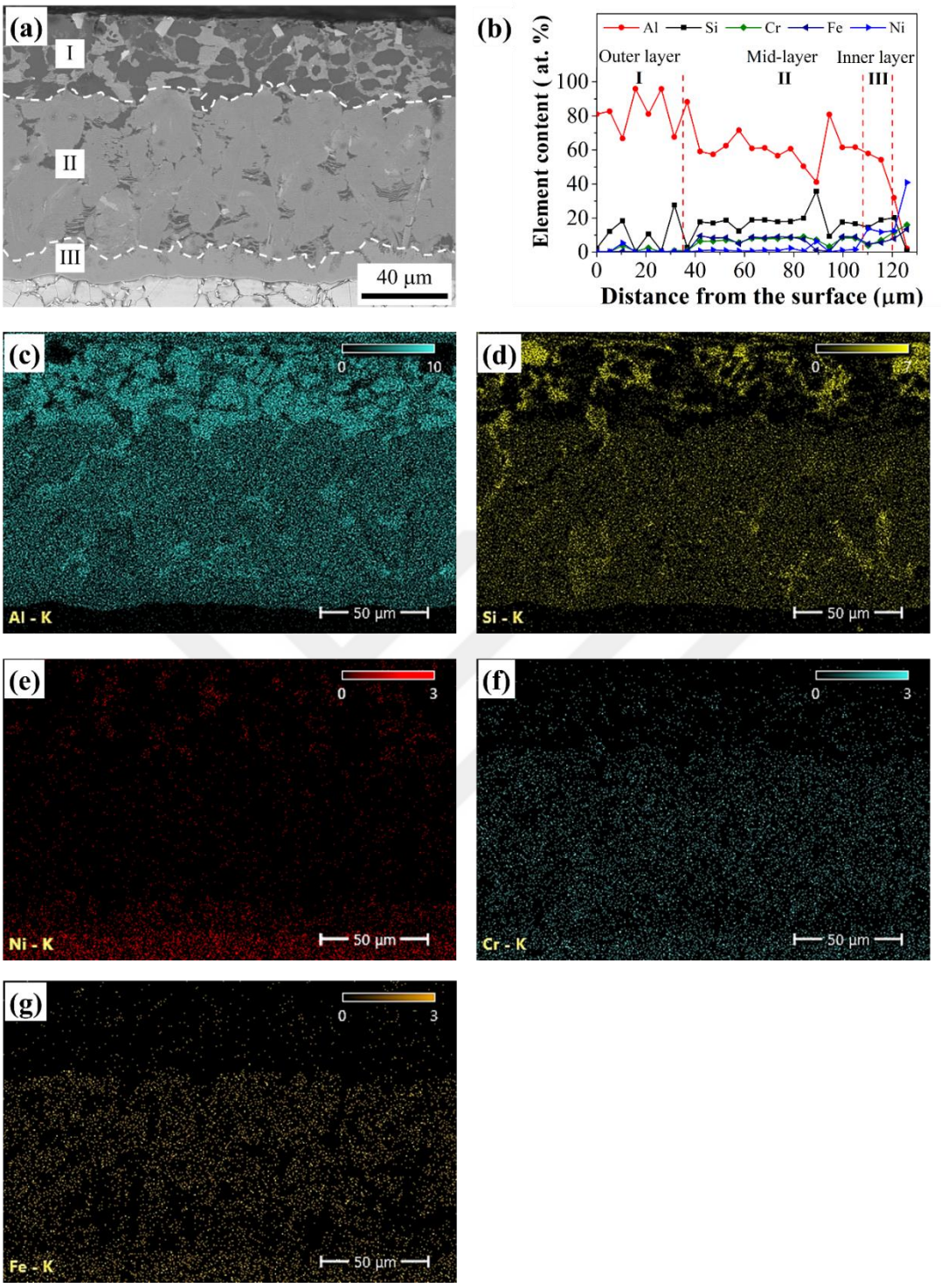

Figure 4.2 : EDS mapping analysis of the main elements in the HDA sample; (a) Cross sectional SEM micrographs of the sample. (b) Line EDS analysis from the surface, (c-g) EDS mapping analysis of Al, Si, Ni, Cr and Fe, respectively.

The mid-layer of the HDA coating is 73 µm thick (Figure 4.3c). In this layer, the black and gray areas still exist, with the latter has a higher volume fraction than in the outer layer. EDS analysis (Figure 4.3d) indicates that the gray lamellar areas are rich in Al and Si (60.3 at. % and 18.9 at. %, respectively) in addition to some Cr and Fe as

previously shown by the EDS line analysis. Their contents are higher as compared to the outer layer. Enlarged view of the gray lamellar areas is presented in Figure 4.3e. This morphology is similar to that observed during hot dip aluminizing of Fe-Cr-B cast steel by Zhang et al [65], and might be due to the formation of various interfaces during the dissolution of elements at the beginning of the HDA process. We also performed a line EDS analysis over the lamellar morphology within the gray area (Figure 4.3f). This analysis showed that Al and Si are the main elements in this area with an Al content of around 60 at. %, and Si content of around 20 at. % in addition to Fe and Cr. However, it is noted that Ni content is very low in the gray lamellar area (1.2 at. %). It is also noted that Al and Si contents slightly change in the expense of each other, and brighter lamella corresponds to a relatively higher Si contents than its content in the molten metal (11 wt. %). As will be shown later by XRD analysis, however, no Si related phase was observed in the HDA sample in the form of silicide or aluminide. This suggests that Si precipitation might occur in a lamellar form during the HDA process when it is not incorporated in the aluminide coating. In the mid layer, there are also white precipitates with an equiaxed or plate morphology (Points 1 and 4 in Figure 4.3c). EDS analysis (Figure 4.3d) taken from these precipitates revealed that Ni is concentrated in these precipitates instead of being present in the gray lamellar area, and the white precipitates have a stoichiometry of $NiAl_3$ type nickel aluminide.

The inner layer, namely, interdiffusion layer (IDL), is the closest layer to the substrate with a thickness of 12 μm. The interface is well adhered to the substrate and free from any discontinuity (Figure 4.3g). The lamellar morphology is dominant over this layer, and Si content (around 18 at. %) is quite high indicating the inward diffusion of Si. There is no black Al-rich region in this layer as a result of the reduced content of Al towards the substrate, with respect to its contents in the outer and the mid layers. Elemental distributions within this layer are rather uniform with Al, Si, Ni, Cr and Fe contents of 57, 17, 13, 6 and 6 at. %, respectively (Figure 4.3h). This analysis also confirms that $Ni(Fe)Al_3$ type aluminide form in the inner layer IDL as a result of inward diffusion of Al. When we compare the lamellar morphology in the outer, the mid- and the inner layers, it is seen that the distinct feature of the lamellar region is that it forms in regions where Al and Si contents are significantly high and, this does not depend on the Ni content.

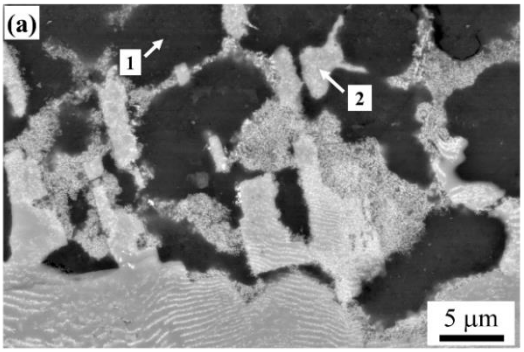

(b)

Elements (in at. %)	Point 1 (black area)	Point 2 (gray area)
O	6.6	4.1
Al	91.9	71.1
Si	1.3	8.2
Cr	0.1	2.4
Fe	0.0	1.3
Ni	0.1	11.8

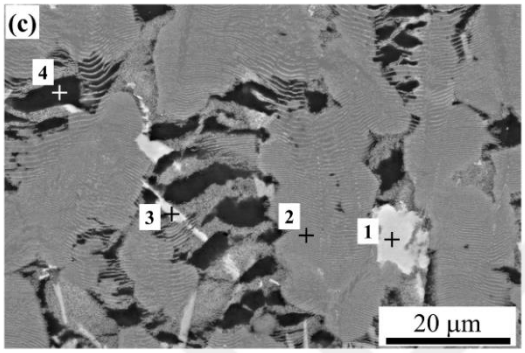

(d)

Elements (in at. %)	Point 1 (polygonal prec.)	Point 2 (lamellar area)	Point 3 (plate like prec.)	Point 4 (black area)
Al	35.7	60.3	53.0	97.0
Si	36.1	18.9	21.5	2.2
Cr	8.8	8.9	7.2	0.3
Fe	1.7	9.0	0.9	0.2
Ni	14.8	1.2	12.9	0.2
Nb	2.2	0.9	3.4	0.1
Mo	0.6	0.8	1.1	0.1

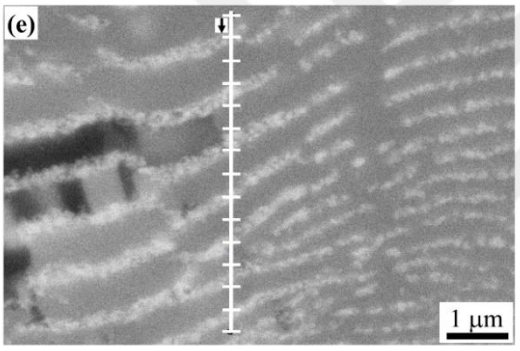

(f)

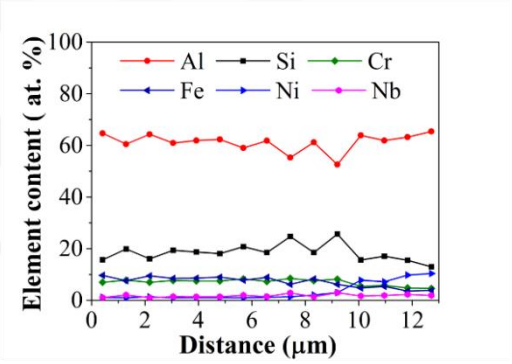

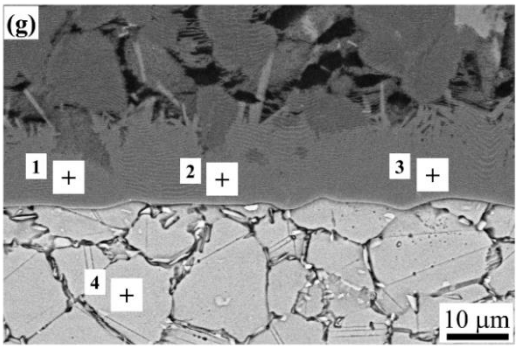

(h)

Elements (in at. %)	Point 1	Point 2	Point 3	Point 4
Al	58.0	55.5	57.2	1.4
Si	15.7	18.9	17.0	0.4
Cr	5.3	6.7	5.7	20.8
Fe	6.1	5.3	5.8	19.1
Ni	13.3	12.1	12.9	51.9

Figure 4.3 : SEM micrographs and corresponding points EDS analysis of the coating layers in the HDA sample. (a-b) the outer layer, (c-d) the mid layer, (e-f) lamellar morphology within the mid layer, (g-h) the inner layer.

Since the total coating thickness is 120 µm in the HDA sample, which inhibits the penetration of X-rays through the coating thickness, sequential grinding (40 µm and 100 µm in two passes) was performed for phase identification in each individual layer (the outer, the mid- and the inner layers). Figure 4.4 shows XRD patterns of each layer

of the HDA coating. As shown, all patterns are similar to each other with no obvious difference among them. The coating layers comprise Al and Si rich phases, $NiAl_3$ type aluminide and some small oxide peaks belonging to Cr and Fe. This agrees with the previous EDS analysis revealing the presence of oxygen, and confirms that oxides form during the HDA process.

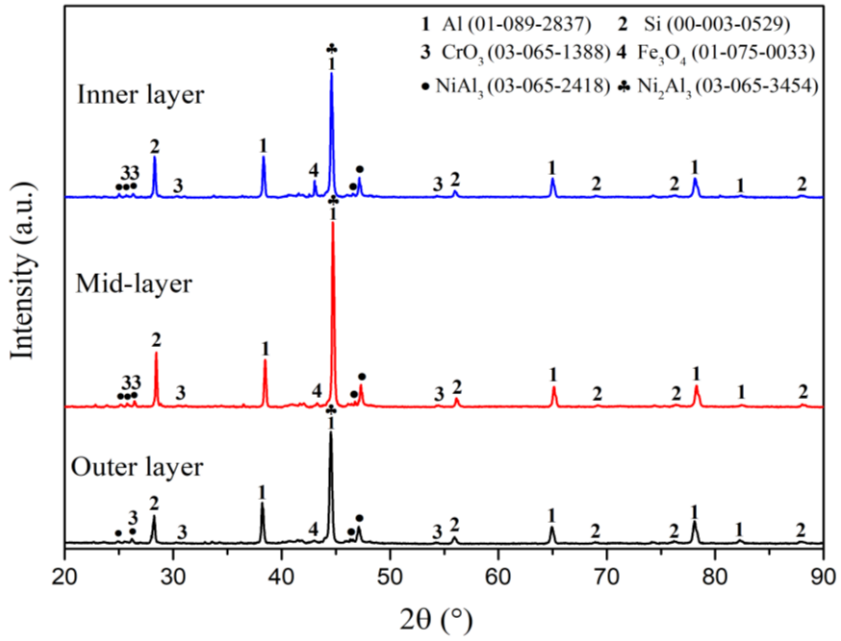

Figure 4.4 : XRD patterns of the inner, mid and outer layers in the HDA sample after sequential grinding from the surface.

4.3.2 Hot dip aluminizing + Induction heating (HDA+Induction sample)

Figure 4.5 shows cross sectional SEM micrographs of the HDA+Induction sample after the induction heating for 20 s. The HDA+Induction sample has a coating layer of 250 μm in total indicating that even short time induction heating increased the coating thickness more than two times as a result of further diffusion provided by the induction heating (Figure 4.5a). It was previously reported that [66] a 200 μm coating thickness was formed when Inconel 718 superalloy was furnace annealed at 700 °C for 10 h after hot dip aluminizing. The coating thickness of the present HDA+Induction sample is 250 μm and higher than the reported thickness in the literature. It shows that 25 % thickness increment in the coating could be achieved when diffusion annealing is performed by the short time induction heating (20 s) with respect to conventional furnace heating taking longer durations (10 h). The observed thickening of the coating through the induction heating can be attributed to the fact that induction heating can heat the sample based on Joule heating and Eddy currents induced within the material.

This situation is advantageous when compared to conventional furnace heating, which relies on radiation within the furnace chamber. During the induction heating, heat is produced by the mechanism of Joule heating, while the Eddy currents can provide electromigration, which is atomic movement due to the current flow through the coating [58]. Therefore, the induction heating can significantly contribute the enhanced diffusion of the atoms resulting in the thickening of the coating.

The HDA+Induction sample has four layers with different morphologies which are separated from each other by well-defined borders, as shown in Figure 4.5a. The thickness of each layer from the outer surface is 70 μm, 125 μm, 45 μm and finally 10 μm. EDS line analysis show the elemental distribution from the outer surface in Figure 4.5b. It is noted that Al content is mostly higher than Ni content revealing the formation of Al-rich aluminides by the induction heating. However, towards the substrate (layers IV and V) Al decreases and Ni increases indicating the formation of Ni-rich aluminides. In addition, as observed in the HDA sample without induction heating (Figure 4.2b), it is observed that in the HDA+Induction sample, the Al and Ni contents in the middle layer of the coating (Layer II) are lower in the regions where Si, Cr, and Nb contents are high and, vice versa. This indicates that these elements (Si, Cr, and Nb) have a tendency to form a new phase, namely silicide phase, which will be confirmed by EDS and XRD analysis later, as a result of limited solubility of these elements in Ni_2Al_3 and NiAl [67].

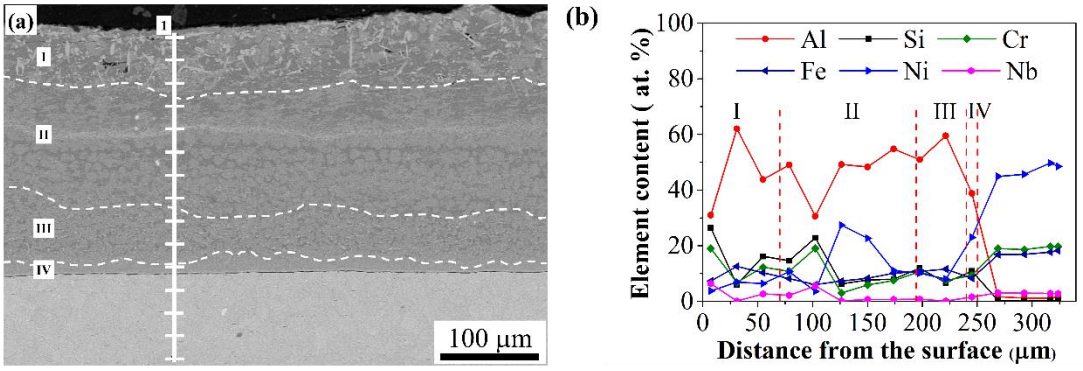

Figure 4.5 : (a) Cross sectional SEM micrograph of the HDA+Induction coating and (b) line EDS analysis results of the coating.

Enlarged SEM micrographs and EDS points analysis of each layer in the HDA+Induction sample were presented in Figure 4.6a and b. The micrographs were backscattered electron images, which are capable of revealing elements based on their

atomic weights, and helps evaluating the distribution of the elements. In the outer layer (Layer I in Figure 4.5a), the contents of all elements significantly vary depending on the location. As a result, light gray areas (Point 1 in Figure 4.6a) are $(Ni,Fe)_2Al_3$ based on the EDS analysis, and the dark gray areas (Point 2 in Figure 4.6a) are $(Ni,Fe)Al_3$. There is also a white phase (Points 3 in Figure 4.6a) in the form of polygonal or plate shape precipitates. They have significantly higher Si, Cr and Nb (36.4, 27.2 and 11.8 at. %, respectively) with a slightly higher Si content than Cr. The former comes from the Al-11 wt. % Si alloy in which the HDA process was performed, and the latter comes from the substrate itself. Beside Cr and Si, other elements were also counted by EDS detector due to spot size of the electron beam. In the white precipitates, Al, Ni and Fe contents are relatively lower (3.5 Al, 0.9 Ni, 2.6 Fe, in at. %, respectively). This observation is well agreement with the line EDS analysis in Figure 4.5b, which shows that Al and Ni variations are in contrast to those of Si, Cr, and Nb. This is further confirmed by EDS mapping analyses (Figure 4.7). Considering that Al and Ni form nickel aluminides after the induction heating, which will be shown later by XRD analysis, it is very obvious that the nickel aluminides formed after the induction heating do not contain Si, Cr, and Nb. Instead, these three elements form a new silicide phase with each other. This is attributed to limited solubility of these elements in nickel aluminides [67]. Cr has a stronger affinity for Si than Al. Also, Mo and Cr silicides generally have more negative $\Delta G°$ values than Nb silicides. However, in the white precipitates, Mo content is quite low (Figure 4.6b). This increases the probability of Cr silicides formation [63]. Based on the element contents in the EDS analysis, formation of $CrSi_2$ phase is likely. As we mentioned in Section 3.1, Cr and Si do not occupy the same locations in the HDA sample. However, they concentrated in the same locations after the induction heating (in the HDA+Induction sample).

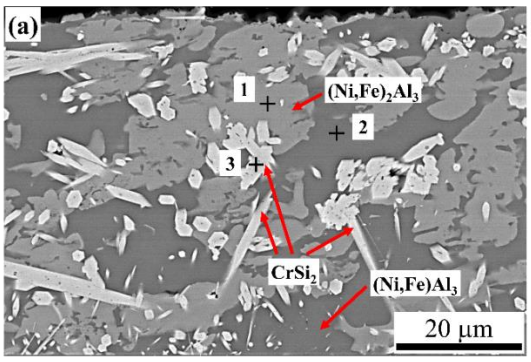

(b)

Elements (in at.%)	Point 1 (Light gray)	Point 2 (Dark gray)	Point 3 (White precipitates)
O	3.7	5.9	14.1
Al	50.2	61.8	3.5
Si	5.4	6.1	36.4
Cr	3.0	7.5	27.2
Fe	8.3	11.7	2.6
Ni	29.4	6.3	0.9
Nb	0.0	0.1	11.8
Mo	0.1	0.5	1.1

Figure 4.6 : (a) Cross sectional SEM micrograph of the outer layer of the HDA+Induction sample, and (b) the EDS point analyses for the points shown in (a).

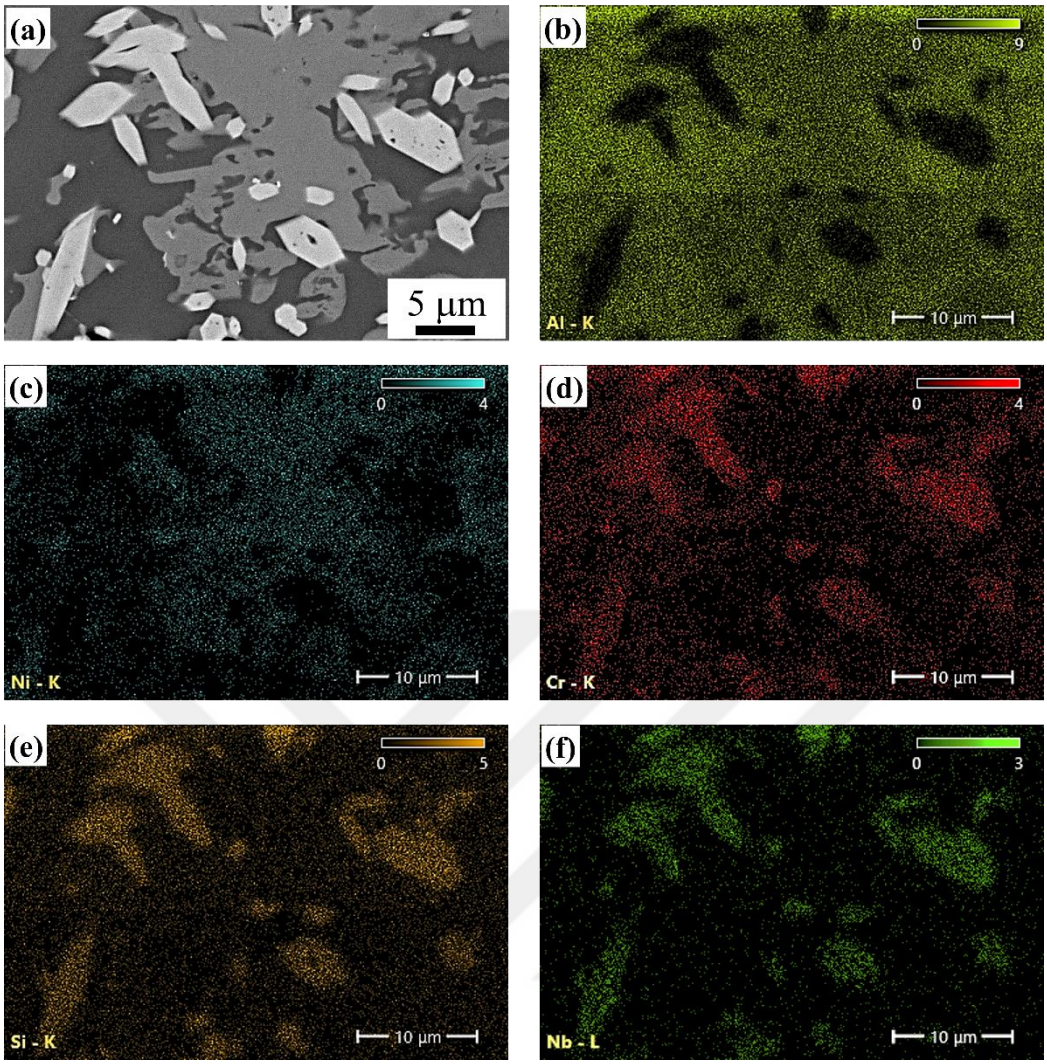

Figure 4.7 : EDS mapping analyses of the outer layer in the HDA+Induction sample. (a) Cross sectional SEM micrographs of the sample. (b-f) EDS mapping analysis of Al, Ni, Cr, Si and Nb, respectively.

Formation of silicide phase becomes possible due to the additional heat provided through the mechanism of Joule heating during the induction heating [58]. Efficiency of the induction heating can be demonstrated by the penetration depth. It is defined as the depth at which eddy currents decrease to approximately 86 % of their maximum value at the surface, and can be expressed by Eq. (4.1) [68]:

$$\delta = 503\sqrt{\frac{\rho}{\mu_r F}} \tag{4.1}$$

where,

δ is the current penetration depth (m),

F is the frequency of the current in the induction coil (20,000 Hz),

ρ is the electrical resistivity of Inconel 718 (1.250 x10^{-6} Ω.m),

μ_r is the relative magnetic permeability of Inconel 718 (1.0011).

For the present study, the penetration depth is found as 3.97 x10^{-3} m (3.97 mm). The coating thicknesses than have been reached in the present study were 120 μm for the HDA sample, and 250 μm for the HDA+Induction sample. It shows that the penetration depth of the Eddy currents provided by the induction heating is significantly higher than the coating thickness, and thus the induction heating can significantly affect the coating layers. In the view point of performance of silicide phases during service, Sekido et al [69] investigated the oxidation behavior of cast Nb-Cr-Si alloys and reported that Cr addition to $NbSi_2$ increases the oxidation resistance of the alloy, while a binary $NbSi_2$ has a poor oxidation resistance, when it is lower than the solubility limit of $NbSi_2$. It is therefore, formation of the $CrSi_2$ phase *in-situ* after the induction heating of the HDA sample might have a potentiality to affect the oxidation behavior of the Inconel 718 superalloy, which is one of the main motivations of aluminizing studies, and thus worth studying in detail in a future investigation.

In the second layer from the outer surface (Layer II in Figure 4.5a), there are light and dark gray regions (Figure 4.8a). These can be assigned as $(Ni,Fe)_2Al_3$, and $(Ni,Fe)Al_3$, respectively, based on points EDS analysis. It should be noted that there are still Si, Cr, and Nb rich white precipitates in this layer. However, they are in the form of tiny needles in contrast to their polygonal or plate like morphology in the outer layer. Si and Cr contents in the needles are also lower than those in the precipitates in the outer layer. Relatively lower contents of such elements in this layer lead to the formation of the thinner morphology and smaller size of the white phase. It indicates that the morphology of the Cr silicide phase strongly depends on the contents of the elements in the coating layers. The inner layers of the coatings (Layers III and IV in Figure 4.5a) are shown in Figure 4.8c. Existing phases are $(Ni,Fe)_2Al_3$ (dark gray, Point 1), $CrSi_2$ (white phase, Point 2). EDS analysis also shows that Al and Ni contents are very close to each other in the IDL layer (Point 3), as also indicated by line EDS analysis in Figure 4.5b. However, NiAl formation in this layer was not seen, as will be confirmed by XRD analysis later in Figure 4.9.

Overall results of the HDA process before and after the induction heating show that it is a high activity process during which inwards diffusion of Al and Si is more

significant than the outward diffusion of Ni in a low activity process [70]. A main advantage of the high activity process is the prevention of the formation of Kirkendall porosities [71]. It was confirmed by the absence of any Kirkendall porosity in either the HDA and the HDA+Induction samples in the present study. Based on the contrast difference revealed by the back scattered electron detector, it should also be mentioned that distribution of the elements within the coating is rather uniform. When the cross sections before and after the induction heating are compared (Figure 4.2a vs Figure 4.5a), it can be seen that short time induction heating encourages the formation of $CrSi_2$ phase as the white precipitate and significantly affected its distribution, size and morphology within the coating. That is, as the distance from the surface increases, $CrSi_2$ phase get thinner and finally, it becomes tiny needles in the mid- and the inner layers of the coating.

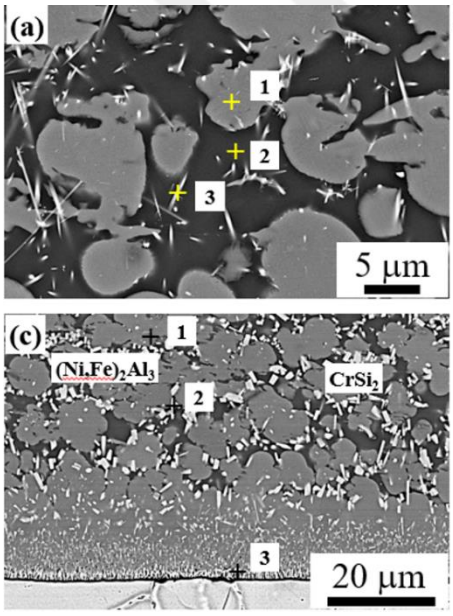

(b)

Elements (in at. %)	Point 1 (light gray) $(Ni,Fe)_2Al_3$	Point 2 (dark gray) $(Ni,Fe)Al_3$	Point 3 (needle-like precipitates)
O	3.5	2.6	2.4
Al	50.7	62.7	50.0
Si	5.9	6.0	14.2
Cr	2.5	7.8	11.9
Fe	5.8	12.2	9.9
Ni	31.3	8.0	7.5
Nb	0.1	0.1	2.3

(d)

Elements (in at. %)	Point 1	Point 2	Point 3
O	4.7	11.7	10.8
Al	48.8	15.2	27.1
Si	5.2	26.4	5.5
Cr	3.3	23.7	10.0
Fe	8.9	5.0	11.0
Ni	28.9	7.6	24.2
Nb	0.1	5.2	8.5

Figure 4.8 : (a-b) Cross sectional SEM micrographs in the HDA+Induction sample and the corresponding EDS analyses of the points shown on the SEM micrographs. (a-b) Layer II in Figure 5a, (c-d) Layers III and IV in Figure 5a.

Similar to the HDA samples without the induction heating, the HDA+Induction sample was also sequentially grinded (100 μm and 220 μm in two passes) to identify the phases in each individual layer. Figure 4.9 shows XRD patterns of each layer of the coating. It is seen that $NiAl_3$ and Ni_2Al_3 are the main aluminide phases as Al-rich aluminides. Although near-equiatomic contents of Al and Ni were detected by EDS analysis, no NiAl peaks were observed by XRD analysis. In addition to various forms of nickel aluminides, it was also confirmed the formation of $CrSi_2$ phase which appears

as the white polygonal and plate shape precipitates in the outer layer, and in the form of tiny needles in the mid and the inner layers, where Si and Cr contents are relatively lower.

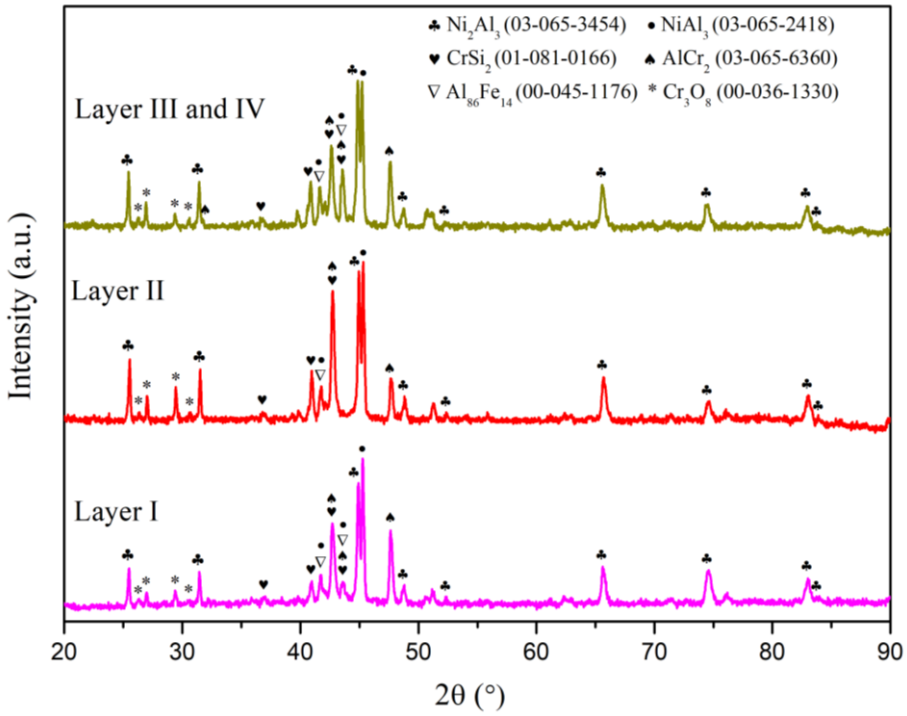

Figure 4.9 : XRD patterns of the HDA+Induction sample after sequential grinding from the surface.

4.3.3 Slurry aluminizing with Induction heating (SA +Induction sample)

Figure 4.10a shows cross sectional SEM micrograph of the slurry aluminized sample. Total coating thickness is 43 μm. It shows that slurry aluminizing with the induction heating produces approximately six times thinner coating than that of HDA+Induction process (with a thickness of 250 μm). Goral et al. [72] reported the formation of similar thickness coating (~40 μm) by a low activity CVD process on Inconel 713 alloy, while the slurry aluminizing in the same work resulted in a thicker coating (~60 μm). The coating produced by the slurry aluminizing in this study comprised two distinct layers such as outer layer with a thickness of 18 μm, and an inner layer of 25 μm in thickness. When compared to higher number of layers in the HDA and HDA+Induction coatings, the SA sample has less coating layers, suggesting that a more uniform coating could be formed with less morphological and elemental variations in slurry aluminizing. The outer layer has an island like morphology with brighter domains of 8-10 μm in size in a darker matrix. The inner layer of the coating is dense, and rather uniform in

appearance. The coating also does not contain any Kirkendall porosity, which occurs on the side of the element having higher diffusivity during interdiffusion. This indicates that interdiffusion takes place in almost equal rates between the substrate-coating interface and between the layers as well. A more uniform and a denser inner layer can be attributed to that Al particles within the slurry has been uniformly distributed and effective interdiffusion could be maintained by the induction heating along the interface. As previously mentioned, the combined effects of Joule heating and Eddy currents provide by the induction heating [58] could melt the Al particles in the slurry, ignite self-propagating high temperature synthesis, and the solid state diffusion taking place within the coating results in the rapid coating formation on the surface of Inconel 718 superalloy. This has been led to the formation of a well-adhered aluminide layer. Each layer of the slurry aluminized coating was examined by SEM-EDS to reveal the elementel distribution and to identify possible phases within the coatings.

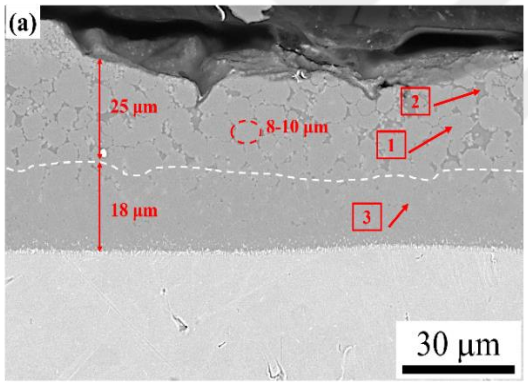

(b)

Elements (in at. %)	Point 1 (bright)	Point 2 (dark)	Point 3 (IDL)
O	4.9	5.4	2.1
Al	53.7	58.9	52.6
Si	0.4	0.6	0.8
Cr	5.7	6.0	8.3
Fe	7.6	6.5	8.4
Ni	27.3	20.1	26.5
Nb	0.2	1.3	0.6
Mo	0.2	0.7	0.4

Figure 4.10 : (a) Cross sectional SEM micrographs of the SA sample (b) EDS analyses of the points shown in (a).

Figure 4.10b shows that Point 1 (bright), Point 2 (dark) and Point 3 (inner layer) seen in Figure 4.5a contain (in at. %) 50-60 Al, 6-8 Cr, 6.5-8.5 Fe, 20-27 Ni suggesting that the coating has mainly Ni_2Al_3. Despite the fact that existence of dark and bright sections, main elements coming from the slurry and the substrate are almost equal in content, and distributed uniformly in the coating. This shows that the substrate elements such as Ni, Fe and Cr dissolve in the molten Al. This is compatible with the reported mechanism of the SA process where the Al particles in the slurry melt first, wetting the substrate surface, then the aluminide coating (Ni_2Al_3) forms through self-propagating high temperature synthesis [73,74], finally subsequent solid state diffusion results in the final structure of the coating. Therefore, as seen in the line EDS

analysis (Figure 4.11), Al content is much higher than Ni content revealing Al-rich aluminides are dominant in the most of the coating. Towards the coating-substrate interface, Ni content is higher than Al content within 5 μm from the interface, indicating that Ni rich phases can even form toward the substrate – coating interface. This observation is compatible with that was reported by Kepa et al. [75] for a slurry aluminized pure Ni substrate followed by a short time heat treatment. Cr can form another phase with Al as reported by Sarraf et al [76] for reactive air aluminizing of In738LC. Small amount of oxygen within the coating is the results of Al oxidation during the heating [62]. Because the heating time is very short, oxide formation must have been very limited allowing to inward diffusion of more Al. Uniform distribution of the elements in the coating also show that, in addition to inward diffusion of Al, outward diffusion of Ni, Fe, and Cr are possible, and absence of any Kirkendall porosity within the coating is attributed to that both inward and outward diffusion take place at nearly equal rates.

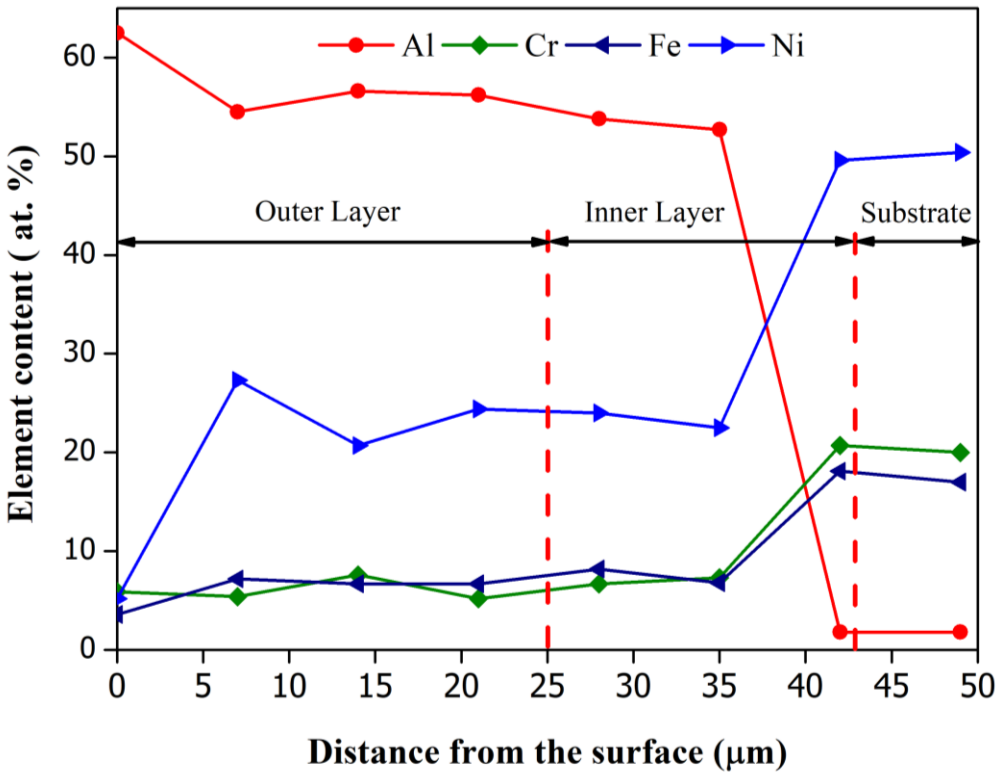

Figure 4.11 : Line EDS analysis through the coating thickness in the slurry aluminized sample.

XRD pattern of the SA coating is given in Figure 4.12. Various form of aluminides such as $NiAl_3$, and Ni_2Al_3 exist, along with $AlCr_2$ as the intermetallic formed by the substrate elements. XRD pattern is compatible with the suggestions of the EDS

analysis. It should be noted that even though formation sequence of nickel aluminides is $NiAl_3$, Ni_2Al_3, Ni_3Al and NiAl [77], in the present study, there is no peak assigned as Ni_3Al. It is reasonable when considering the maximum atomic ratio of Ni is about 50 %, which is less than required for the formation of Ni_3Al.

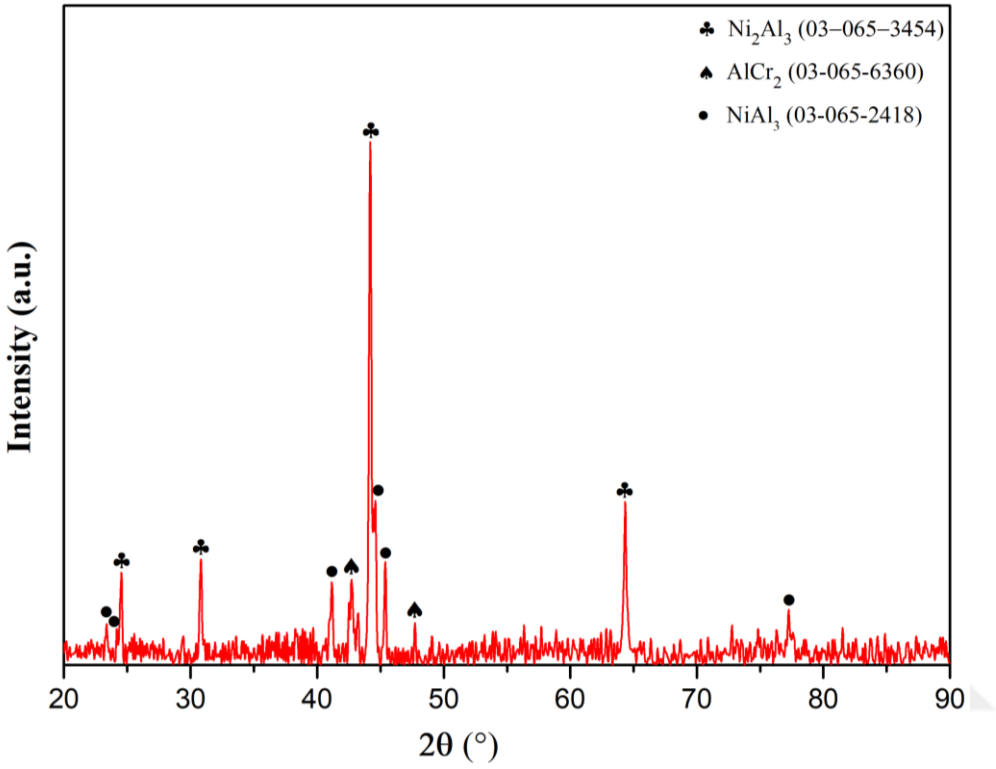

Figure 4.12 : XRD patterns of the SA sample after the induction heating.

Figure 4.13 shows the EBSD (Electron Backscatter Diffraction) analysis of the SA sample, which revealed the presence of NiAl within the coating layer. However, no other phases could be assigned in the EBSD analysis. It should be mentioned that grain size is mostly uniform within the coating with finer grains detected at the substrate coating interface. Also, no preferred orientation for the grains was noticed. Wang et al [78] recently reported that oxide morphology depends on grain orientation for Haynes 230 alloy. From this point of view, in addition to their effects on morphological and structural properties, tailored properties of slurry and induction heating parameters might also potentially affect the crystal orientations and hence the service performance of the coating such as oxidation resistance.

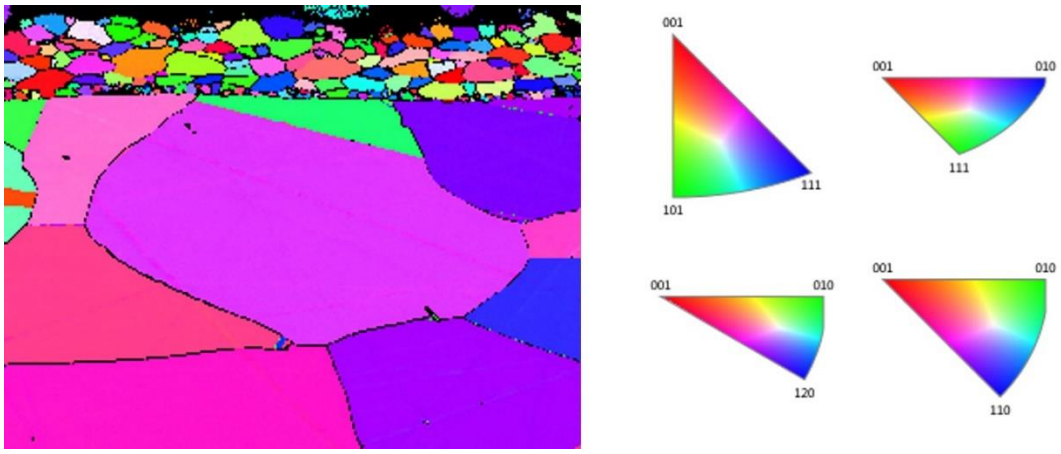

Figure 4.13 : Cross sectional phase colour map of the SA sample.

4.4 Comparison of the Coatings

The HDA, the HDA+Induction, and the SA+Induction sample are compared in this section. Such an attempt would be informative even though the former uses a molten Al-11 wt. % Si bath while the latter uses a slurry containing pure Al particles. Because the processes have several similarities and dissimilarities, they resulted in structural and morphological differences. These are elemental distribution in the coatings, coating thickness, type of the formed phases, and appearance of the substrate-coating interface.

In the view point of elemental distribution, EDS mapping analysis show that Cr and Fe mostly occupy the mid- and the inner layers of the HDA sample, while their contents are relatively low in the outer layer. The contents of Cr and Fe become more uniform due to further diffusion provided by the induction heating (in the HDA+Induction sample). At the same time, Cr and Si form $CrSi_2$ whose morphology varies from polygonal or plate-like to needle-like form as Cr and Si content decrease with increasing distance from the surface. For the hot dip aluminizing processes, Al content is always higher than Ni indicating that Al-rich nickel aluminides mainly form. For the HDA coating, the Al-rich aluminide is $NiAl_3$. After the induction heating, in the HDA+Induction sample, Ni_2Al_3 also form. In the SA coatings, however, towards the substrate a Ni rich aluminide, NiAl, can even form in addition to $NiAl_3$ and Ni_2Al_3. In the view point of distributions of the substrate elements, Cr and Fe distributed uniformly and exist in the level of 6-8.5 at. % throughout the entire SA coating. It is attributed to the fact that HDA and SA have different mechanisms although they resemble to each other at the initial stages of the processes. In the former, the substrate

is immersed in a molten bath at 700 °C where interfacial reactions between the substrate elements and the molten metal are initiated, and the elements dissolve to the molten metal. At the same time, Al inward diffusion and Ni outward diffusion take place with the latter is limited as evidenced by EDS point and mapping analysis (Figures 4.2b and 4.2e). This mechanism is responsible for the presence of Cr and Si in the mid- and the inner layers of the HDA coatings. Then a solid state diffusion takes place during the induction heating. It provides more diffusion and redistributes the elements within the coating, i.e., the outward diffusion of Ni, Cr and Fe resulting their more uniform distribution towards the outer layer (Figure 4.5b). However, in the SA process, the substrate was sprayed first by the slurry at room temperature, and the sprayed substrate is then subjected to high temperature provided by the induction heating. Therefore, in the SA process, the sprayed substrate experiences a high temperature once, only during the induction heating. During this heating, melting of Al within the slurry takes place first, and Al melt wets the substrate. The substrate elements dissolve in the molten Al. In this respect, the initial stage of the SA process resembles to the initial stage of the HDA process in the view point of dissolution of the elements. Afterwards, self-propagating high temperature synthesis forms the coating in the SA process, and finally solid state diffusion finalizes the coating in its final form. This explains the observed difference in the coating thickness between the HDA+Induction coating and the SA coating. In the former, there is a coating which has been already formed during the HDA process (120 μm thick), and the induction heating providing further diffusion allows the coating to become thicker (250 μm). In the latter, coating formation and diffusion take place only within 20 s resulting a thinner coating (43 μm). In this limited duration, a significant outward diffusion of Ni is unlikely. However, there is significant Ni content (20.1 - 26.5 at. % as shown in Figure 4.10b) throughout the SA coating. Thus, Ni must have been dissolved in the first stage, namely during the dissolution, in the SA process. It should also be considered that the SA coating has always higher Ni content than the HDA coating (as shown in Figure 4.10b and Figure 4.2b, respectively). However, the HDA+Induction coating has similar Ni content with the SA coating (as shown in Figure 4.5b and Figure 10b, respectively). This suggests that the induction heating in the SA process, which heated the sample up to 1000 °C, can provide more rapid dissolution and more uniform distribution of the elements than that of the HDA process performed at 700 °C, and a

coating uniformity similar to that of the SA coating for Ni, Fe and Cr can be achieved in HDA coatings only after the application of the induction heating. Regarding the effect of coating thickness, ASTM B875-16 is the standard related to the aluminizing of nickel-based superalloys, which specifies that the coating layer must have a minimum thickness of 25 μm and be free of voids. While a lower limit for thickness is defined, no upper limit is specified. However, literature data indicate that increasing thickness increases the risk of void formation within the coating. For example, in the study by Cheng et al. [79], hot-dip aluminizing was applied for different durations, resulting in samples with varying coating thicknesses. It was observed that as the thickness increased, the prevalence of Kirkendall voids also increased. Therefore, the optimal coating thickness is often determined according to the expected performance requirements, such as oxidation, erosion, or wear resistance. In the work of Castañeda et al. [80], the samples with coating thicknesses in the range of 8–80 μm demonstrated improved oxidation resistance with increasing thickness. Conversely, in the study of Kopec et al. [81], fatigue tests on MAR-M247 alloys coated by CVD aluminizing with thicknesses of 20 and 40 μm revealed no significant influence of coating thickness on fatigue strength. The present study focuses on the structural characteristics of IN718 alloy coated by two different aluminizing methods, without conducting performance tests. To clearly evaluate the influence of coating thickness on oxidation resistance, thermal shock behaviour, static or dynamic loading conditions, and wear resistance, further dedicated testing is required.

4.5 Conclusions

Two commonly used aluminizing processes, hot dip aluminizing and slurry aluminizing on Inconel 718 superalloy were investigated in this study. Short time induction heating was utilized after hot dipping in the HDA processes, and after the slurry application in the SA process. Thus, three different coated samples were produced such as HDA sample, HDA+Induction sample, and SA+Induction sample. Although the HDA and the SA processes have different mechanisms in the view point of coating formation, and the aluminium sources used in the processes are different, such as molten Al-Si bath for the HDA process, and pure Al powder for the SA process, the initial stage of both processes, namely the dissolution of the substrate elements into the melt, is similar to each other in many respects. The obtained results

showed that all coatings were well adhered to the substrate without any apparent crack or Kirkendall porosity, as a promising characteristic for the service performance of the coatings. The HDA process was dominated by the dissolution of substrate elements such as Ni, Cr and Fe, inward diffusion of Al, and outward diffusion of Ni, resulting of $NiAl_3$ and Ni_2Al_3 aluminides being the former was the dominant phase. After the application of the induction heating (the HDA+Induction sample), solid state diffusion rearranges the elements within the coating leading to the formation of more Ni_2Al_3, increased the coating thickness from 120 μm to 250 μm, and resulted in the formation of $CrSi_2$ phase within the coatings. It is also noted that the morphology of the silicide phase changed from polygonal or plate-like morphology to needle-like morphology with increasing distance from the surface. In the SA sample, the significant differences with respect to the HDA, and HDA+Induction samples are the reduced thickness (43 μm), a denser IDL layer and more uniform element distribution within the coating. Although the major aluminide phase was still Ni_2Al_3, the SA process also allowed the formation of Ni-rich aluminide such as NiAl at the substrate coating interface. It should be emphasized that the SA process could produce such a dense and more uniform coating within very short period of time (20 s). Overall results highlighted remarkable subjects for future research for both process in combination with the short time induction heating. These are silicide formation in the HDA+Induction sample, and the formation of a uniform and a dense coating in the SA sample. When taking into account the previous works reporting that Cr addition increases oxidation resistance of Nb-silicides. It would be worth studying the effect of silicide formation on the oxidation behavior of Inconel 718 superalloy. Also, the SA process, being a versatile technique, which can be applied to various substrates without subjected them to a high temperature for a long time, would be a promising aluminizing method to protect the Ni-based substrates against oxidation.

5. PACK ALUMINIZING BY INDUCTION HEATING: APPLICATION TO INCONEL 718 PRODUCED BY COLD SPRAY ADDITIVE MANUFACTURING[3]

5.1 Introduction

IN718 is a nickel-based superalloy widely used in aerospace and power generation due to its excellent high-temperature strength and creep resistance resulting from the precipitation–strengthened mechanism. IN718 alloy is primarily produced using a combination of special melting techniques such as vacuum induction melting, forging methods, and precision heat treatment processes [82]. Recently, the CSAM process has attracted significant interest as a viable, alternative production technique for IN718 alloy [83]. The high deposition efficiency, reduced porosity, and minimal thermal distortion achieved with the CSAM process offer significant potential for reducing material waste and carbon emissions in conventional machining operations. CSAM enables the deposition of materials at temperatures well below their melting points. Due to its unique capabilities, CSAM deposition is increasingly accepted as both an additive manufacturing and repair technology. CSAM can be considered a rapid manufacturing process capable of producing individual components without size constraints and applicable to a wide range of materials, including IN718 alloy [84]. However, recent studies reveal the need to develop more controlled and toolpath-optimized manufacturing strategies to improve the limited geometric accuracy of CSAM, which stems from the nature of the particle deposition process [85]. Furthermore, in the study of Garfias et al. [86], significant improvements in coating/substrate adhesion were reported when the IN718 substrate was heated before deposition, further highlighting the importance of thermal management in the CSAM process.

[3]This chapter is based on the article: Karakas, A., Balci, E. and Baydogan, M. (2026). Pack Aluminizing by Induction Heating: Application to Inconel 718 Produced by Cold Spray Additive Manufacturing, Mater. Res. Express 13 (2026), https://doi: 10.1088/2053-1591/ae3711

IN718 becomes susceptible to accelerated oxidation and spallation above 700 °C [87,88]. Various surface engineering techniques have been developed to improve the surface integrity of IN718 under these conditions, and among these, aluminide coatings are considered one of the most effective protective strategies. Aluminide coatings operate on the principle of forming thermodynamically stable nickel-aluminum intermetallics (e.g., $NiAl_3$, Ni_2Al_3, NiAl) that support the formation of a slow-growing, dense, and adherent α-Al_2O_3 layer during high-temperature exposure. This oxide layer acts as a diffusion barrier, preventing further oxidation and minimizing the loss of alloying elements, particularly chromium and nickel, which are otherwise depleted during conventional scale formation involving Cr_2O_3 and NiO [89].

Among aluminizing methods, pack aluminizing stands out due to its cost-effectiveness, scalability, and ability to produce high-quality coatings with adjustable thickness and phase composition. In the pack aluminizing process, a powder mixture containing aluminum as the source, an inert filler, and a halide-based activator such as $AlCl_3$ is prepared. Solid-state diffusion of aluminum is then achieved on the substrate surface placed within this powder mixture. The process is typically carried out in the temperature range of 600–700 °C for low-temperature aluminizing and 1000–1100 °C for high-temperature aluminizing; higher temperatures promote deeper diffusion and the formation of more stable aluminide phases [90–92]. However, prolonged exposure to such high temperatures can lead to grain growth, precipitate coarsening, and even the formation of detrimental phases such as δ (Ni_3Nb) or Laves phases in IN718, which can seriously affect the mechanical integrity of the component [93].

Previous studies on the aluminizing of IN718 have shown a strong correlation between process parameters and coating performance. For example, in the study by Kumar et al. [94], IN718 samples were coated using the pack aluminizing process at 900 °C for 5 h, resulting in the formation of Ni_2Al_3 and NiAl-based coating layers. Subsequently, high-temperature corrosion tests were performed at 700 °C for 5 h. They found that the aluminized surface reduced hot corrosion by approximately 50% compared to the untreated alloy. However, conventional pack aluminizing, which is typically performed by prolonged heating in a furnace, involves significant energy consumption and exposes the part to high temperatures for an extended period. This might limit the process's use in industrial applications involving complex geometries or thermal sensitivity, and can undesirably alter the microstructure of the substrate. In contrast,

induction heating provides a localized and rapid thermal input, allowing the process to be completed in a significantly shorter time. For example, Hu et al. [97] used induction heating during pack chromizing of AISI 5140 steel and demonstrated that induction heating can be successfully used for pack chromizing due to the rapid completion of the process and the lack of detrimental effects on the substrate microstructure. This technique not only increases energy efficiency and shortens overall processing time but also minimizes detrimental microstructural changes associated with prolonged high-temperature exposure [31,96]. Induction heating offers potential advantages for the pack aluminizing process; however, to our knowledge, there is no published study in the literature systematically investigating the application of induction heating in the pack aluminizing of IN718. Therefore, considering that long durations of several hours in conventional furnace aluminizing can lead to detrimental effects on the substrate, this study aims to investigate the microstructure and tribological performance of aluminide coatings formed by applying shorter PIA processes of 5, 10, and 15 min on CSAM-fabricated IN718 superalloy.

5.2 Experimental

5.2.1 Material and coating processes

The CSAM process employed in this study was performed using a high-pressure industrial cold spray system. Cylindrical aluminum rods with dimensions of 60 mm in diameter and 300 mm were used as the substrate material. The IN718 coating was deposited to the aluminum substrate under a nitrogen atmosphere using a combined rotating and reciprocating tool path. During this process, the aluminum rods rotated continuously around its long axis, while the spray nozzle moved axially back and forth between two predetermined positions. The powder coating material was commercial IN718 powder with an average particle size of 20 μm. The spraying distance was 30 mm. After the cold spraying process, the IN718 coated sample was immersed in a caustic bath to dissolve and remove the aluminum substrate. IN718 surface was then cleaned, sandblasted, and prepared for the pack aluminizing processes to ensure proper adhesion of the coating. The chemical composition of the IN718 sample investigated is given in Table 5.1.

Table 5.1 : Chemical composition of IN718 sample.

Elements	C	Mn	Cr	Fe	Mo	Co	Nb	Ti	Al	Ni
wt.%	0.08	0.25	18.24	16.29	3.01	0.8	5.27	0.83	0.87	Balance

The aluminide coatings were produced using the pack aluminizing process. The pack mixture consisted of pure aluminum powder (25% wt., <45 µm, 99.5% purity) used as the aluminum source, $AlCl_3$ powder (5% wt., <45 µm, 98% purity) used as the activator, and Al_2O_3 powder (70% wt., <45 µm, 99% purity) used as an inert filler to prevent sintering and agglomeration of the powder. In this study, samples were embedded into the powder mixture in a sealed retort.

Induction heating equipment (model RT-380M50, manufactured by Reterm Induction Heating Limited, TUR) with a maximum power of 50 kW and maximum frequency of 20 kHz was used as the heat source for diffusion annealing. Depending on the shape and size of the samples, the appropriate helical coil was used, and the distance between the coil and the sample was 10 mm. The induction coil was being cooled with water circulating system during the heating to prevent overheating. The induction current was set to heat the sample from room temperature to approximately 1000 °C with a heating rate of 50 °C/sec. The temperature was measured by a pyrometer. After reaching the desired temperature, the coated samples were hold at this temperature for 5, 10, and 15 min (hereafter referred as PIA5, PIA10, and PIA15, respectively), and cooled in air to the room temperature. Schematic illustration and photograph of pack aluminizing with induction heating process are indicated in Figure 5.1.

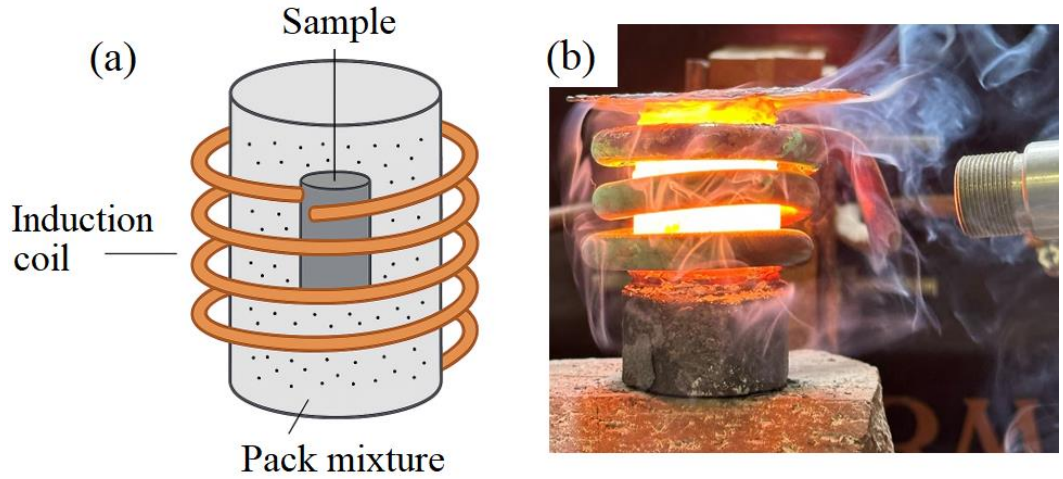

Figure 5.1 : (a) Shematic illustration and (b) photograph of pack aluminizing with induction heating process.

5.2.2 Characterization

After the induction assisted pack aluminizing were performed, cross sections of the samples were mounted in bakelite, ground by emery papers, polished with 1 μm diamond paste in a conventional manner, and etched with Kalling2 solution (5 g $CuCl_2$ + 100 mL HCl + 100 mL ethanol) for a few seconds. Microstructural examinations were conducted using a scanning electron microscope (SEM – Thermofisher Quatro) operating at 25 kV, equipped with an X-ray energy-dispersive spectroscopy (EDS) detector. Qualitative phase analysis was made by X-ray Diffraction (XRD) using a Rigaku D-Max 2200 PCI device (Cu Kα radiation, $\lambda = 0.15418$ nm) between 2θ angles of 20 and 90° with a scanning rate of 2 °C/min. To evaluate the coatings' adhesion to the substrate, Rockwell C adhesion tests (with a diamond cone indenter having 0.2 mm tip radius under a load of 150 kg) were conducted, and the coatings' surface were examined by an optical microscope against crack and delamination.

Dry sliding wear tests of the uncoated and the coated samples were conducted utilizing a reciprocating wear testing apparatus (Tribotech Oscillating Tribotester), an Al_2O_3 ball with a diameter of 6 mm was used as counterface material. The wear tests were performed under dry sliding conditions at room temperature, with a load of 3 N, a sliding speed of 10 mm/s, a stroke length of 5 mm, and a total sliding distance of 50 m. Friction coefficient was recorded continuously during the tests. After the tests, the wear tracks were scanned by a two-dimensional surface profilometer (Veeco Dektak 6M) to evaluate the worn volume. It was then used to calculate the wear rate in the unit of mm^3/Nm by also considering the normal load and the sliding distance. Subsequent to the tests, the worn surfaces were examined by using a scanning electron microscopy (SEM, Hitachi TM-1000) to determine the wear mechanism.

5.3 Results and Discussion

5.3.1 Microstructural examinations and phase composition

Figure 5.2 shows the microstructure of the IN718 sample produced with CSAM before the PIA process. It can be observed that it has a dentritic microstructure and there are voids at the interparticle regions. Since the IN718 powders used in the CSAM process are produced by atomization method, their microstructure is formed in a dendritic structure and gaps may form between the particles during the plastic deformation of

the powders during the cold spray process. For these two reasons, a dendritic and porous microstructure is formed after CSAM [98,99]. Cross sectional SEM micrographs of the aluminized samples in Figure 3 shows that the substrate has a dendritic structure and therefore the induction heat treatment does not change the microstructure of the substrate.

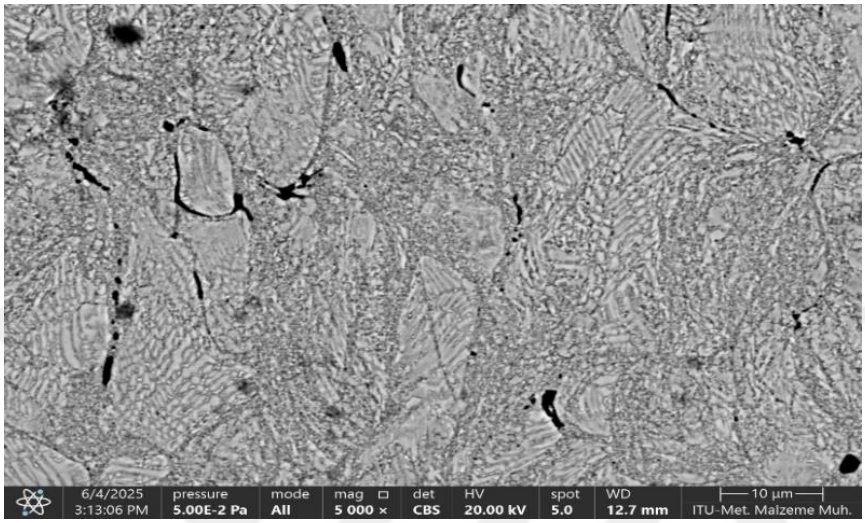

Figure 5.2 : SEM micrograph of IN718 sample produced by CSAM.

As seen in the micrographs in Figure 5.3, the PIA process successfully produced dense and adherent aluminide coatings on the IN718 substrate for all PIA times. The coating thickness was found to be approximately 10 µm in the PIA5 sample and approximately 19 µm in the PIA10 sample, thus increasing as the coating time increased up to 10 min, while remaining constant at approximately 19 µm in the PIA15 sample. The SEM micrographs in Figure 5.3b and c reveal the presence of a distinct bilayer structure within the coating in the PIA10 and the PIA15 samples. EDS analysis was used to determine the composition of these layers. The outer layer (dark region) was found to be rich in aluminum, with a composition of approximately (in at. %) 74.5% Al, 15.5% Ni, 4.5% Fe, and 5.5% Cr, corresponding to the Ni(Fe,Cr)Al_3 phase. The inner layer (white region) contained a lower concentration of aluminum, with a composition of approximately (in at. %) 60.4 Al, 24.6 Ni, 7.3 Fe, and 7.7 Cr, corresponding to the Ni_2(Fe,Cr)Al_3 phase for both samples. These Al-rich phases are characteristics of a high-activity, low-temperature pack aluminizing process, where coating growth is controlled by the inward diffusion of aluminum into the substrate. Aluminizing process is divided into low activity and high activity processes according to the temperature used. NiAl-based (high temperature aluminizing) [100] coating layers are

obtained by outward diffusion of Ni when low activity process is applied, and Ni_2Al_3-based [101] coating layers are obtained by inward diffusion of Al when high activity process is applied. On the other hand, the aluminizing process in this study was carried out at a high temperature of 1000 °C, the resulting coating morphology and phase composition are typical for a low-temperature high activity process, as the dominant phases were Al-rich intermetallics, such as Ni_2Al_3 and $NiAl_3$. This is attributed to the short induction heating time, particularly 10 min process, which limited the diffusion of nickel atoms towards the surface. With increasing aluminizing time from 10 min to 15 min, no significant changes were observed in the coating thickness, phase composition, or morphology, suggesting that the system had already reached a kinetically stable configuration. This observation suggests that within 10–15 min during the induction heating, Ni-rich aluminide phases (e.g., NiAl, Ni_3Al) did not have sufficient time to nucleate and grow. Although the processing temperature (1000 °C) is thermodynamically sufficient to overcome the activation energy barrier for the formation of Ni-rich phases [102], the diffusion-controlled kinetics at such short durations prevented their development. It was initially estimated that process durations of 10–15 min would be insufficient to form aluminide coatings at 1000 °C under conventional furnace-based pack aluminizing conditions. However, it was hypothesized that the additional mechanisms activated during induction heating such as localized Joule heating and electromigration could enhance diffusion kinetics and enable the formation of aluminide phases even within this limited time interval [20]. As a result, the phases such as Ni_2Al_3 and $NiAl_3$ that could typically form at 600–700 °C after several hours were observed to form within just 10 min under the induction heating. Thevand et al. [103] observed the formation of Ni_2Al_3 and $NiAl_3$ at phases on pure nickel after 1.5 h of pack aluminizing at 1050 °C. Similarly, Jopek et al. [104] reported the dominance of Ni_2Al_3 in the coating of MAR-M247 alloy treated at 950 °C for 4 h. These results suggest that phase formation is governed not solely by temperature, but also by time-dependent diffusion kinetics, which are strongly influenced by the heating method used.

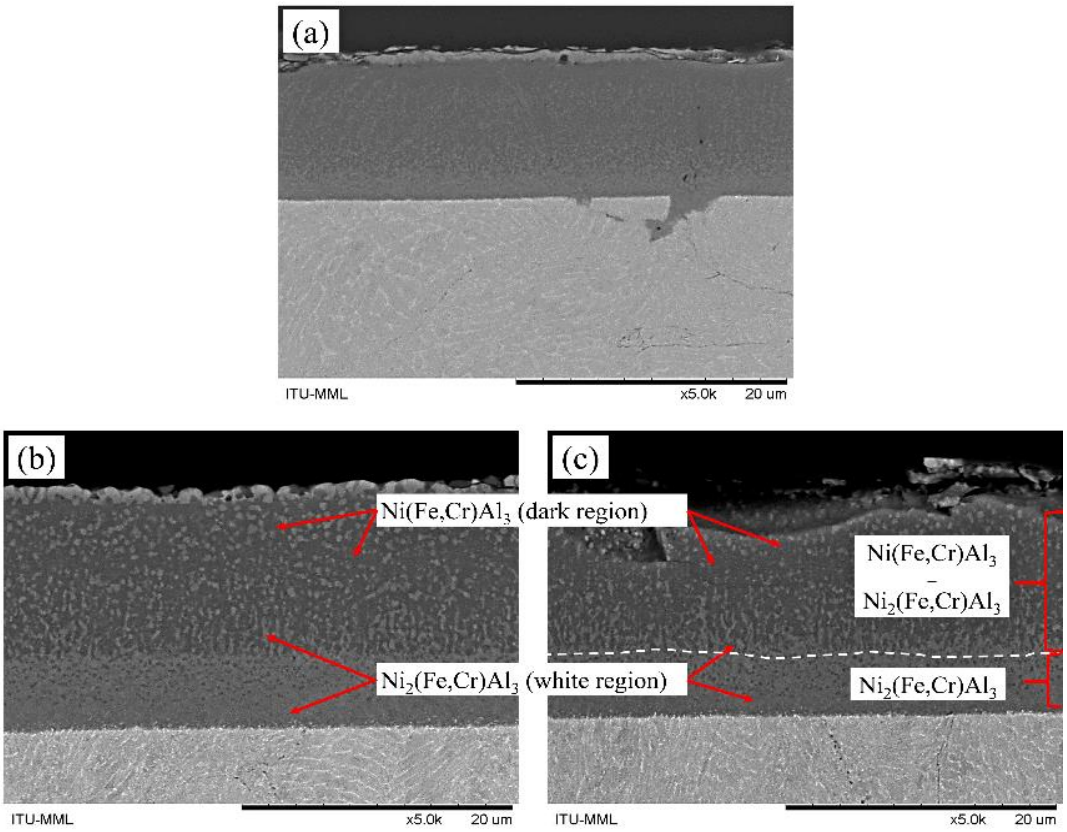

Figure 5.3 : Cross sectional SEM micrographs of the coatings for (a) PIA5, (b) PIA10 and (c) PIA15 samples.

Figure 5.4 presents the appearance of the coatings' surfaces after the Rockwell C adhesion tests, which were examined to evaluate the adhesion strength of the coating-substrate in a qualilitative manner, based on ths standar comparison charts given in elsewhere [87,105]. The PIA5 sample was assigned as HF3 due to limited circumferential cracks around the indent. The adhesion strength of the PIA10 sample was evaluated as HY4 due to the circumferential cracks and partial delamination. For the PIA15 sample, it is seen that more delamination exists in addition to the circumeferential cracks, therefore we assigned this sample as HF5. HF1 to HF4 are acceptable in the view point of coating adhesion, while HF5 and HF 6 are not acceptable. Accordingly, we concluded that PIA5 and PIA10 samples have an acceptable level of coating adhesion.

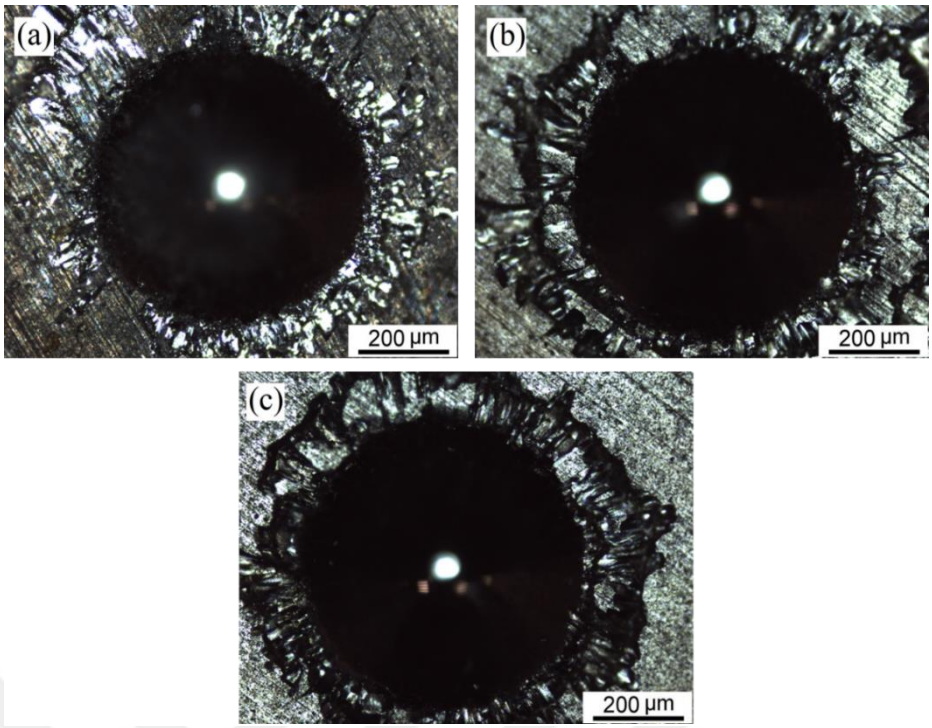

Figure 5.4 : Surface appearances of the samples after the Rockwell C adhesion tests. (a) PIA5, (b) PIA10, and (c) PIA15.

During the aluminizing process, increasing thermal conditions and extended exposure time promote the decomposition of the aluminizing medium, releasing reactive aluminum species. These aluminum atoms continuously diffuse into the substrate, where they subsequently participate in further chemical reactions (5.1) and (5.2) [106]:

$$3[Al] + Ni \rightarrow NiAl_3 \quad (5.1)$$

$$[Ni] + NiAl_3 \rightarrow Ni_2Al_3 \quad (5.2)$$

According to thermodynamic data, the Gibbs free energy of formation for the compounds involved in reactions of $NiAl_3$ and Ni_2Al_3 are quantified as -1.319 eV/atom, -0.613 eV/atom, respectively. The presence of negative Gibbs free energy values indicates the thermodynamic favorability and spontaneity of these reactions under the stipulated conditions [107]. Due to its lower Gibbs free energy, the $NiAl_3$ phase is thermodynamically expected to form prior to other aluminide phases. In this study, both $NiAl_3$ and Ni_2Al_3 phases were observed to coexist within the coating. EDS analyses revealed that Ni_2Al_3 was predominantly located near the substrate interface, whereas $NiAl_3$ became more concentrated towards the outer surface. This compositional gradient suggests a sequential phase formation pathway governed not only by thermodynamic stability, but also by diffusion-controlled kinetics. The inward diffusion of aluminum and the outward diffusion of nickel during the aluminizing

process likely contributed to this layered distribution. Grimme et al. [108] performed pack aluminizing to IN718 alloy at two different temperatures, forming Ni_2Al_3 and NiAl type aluminides in the coatings. They also conducted wear tests of the samples, and found that both phases increased the wear resistance of the alloy exhibiting similar wear behaviour at room temperature. Döleker et al. [109] formed $NiAl_3$ on the surface of Inconel 601 alloy by pack aluminizing at 700 °C for 4 h, and conducted wear and oxidation tests. They observed that aluminium-rich $NiAl_3$ phase increased wear and oxidation resistance of the alloy. As reported in various studies, aluminum-rich nickel aluminide phases such as $NiAl_3$ and Ni_2Al_3 contribute to enhanced wear resistance of the coated samples. This improvement is primarily attributed to the high hardness of these intermetallic compounds, which reduce material loss during sliding or abrasive contact. XRD patterns of the samples given in Figure 5.5 confirm the EDS analyses results. XRD peaks corresponding to Ni_2Al_3 and $NiAl_3$ are dominant, along with $AlCr_2$ and $NiFeAl_5$ phases for all samples.

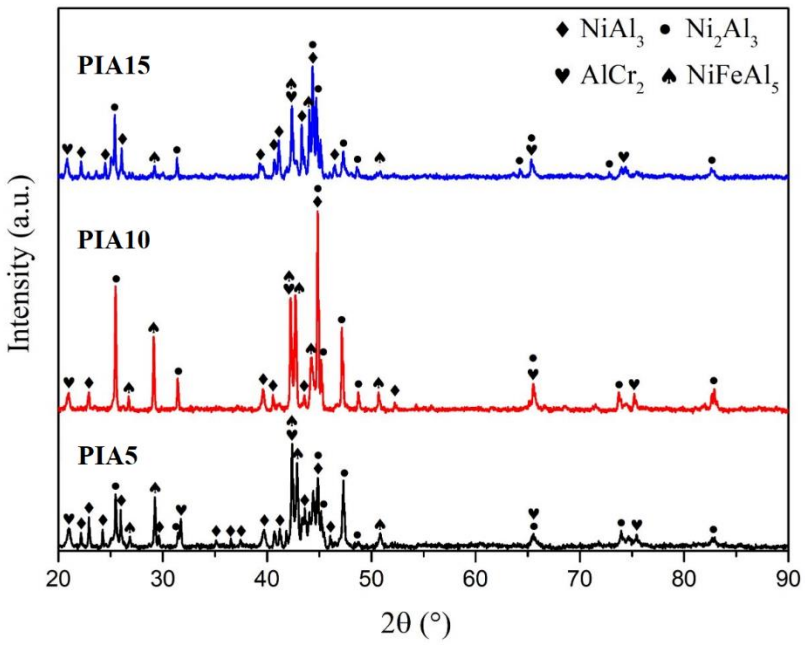

Figure 5.5 : XRD patterns of the samples.

5.3.2 Tribological properties

Figure 5.6 shows the cross-sectional profiles of the wear tracks. These profiles clearly reveal the enhanced wear resistance provided by the coatings. The uncoated sample exhibits by far the deepest wear track. The wear track depth reaches approximately 35 µm. This indicates that the IN718 alloy undergoes significant wear under these test conditions when uncoated. All aluminized samples demonstrated dramatically higher

wear resistance compared to the uncoated sample. The PIA5 sample has a wear track depth of approximately 15 µm. The wear depth is significantly reduced compared to the uncoated sample. The PIA10 sample has a wear track depth of approximately 5 µm. The PIA15 sample shows a wear depth of approximately 5-10 µm. Wear rate of the samples was also calculated by considering worn volume, normal load and the sliding distance, and given in Figure 5.7 in comparison to hardness of the samples. The aluminized samples with higher hardness have a lower wear rate (higher wear resistance) than the substrate. It is clear that pack aluminizing assisted with the induction heating significantly improved the wear resistance of IN718 alloy fabricated by cold spray additive manufacturing. Among the aluminized samples, PIA10 sample (10 min induction heated sample) exhibits the lowest wear rate. Standard deviations of the hardness values are slightly higher than those of the wear rate, and for the aluminized samples, no simple correlation is observed between the wear rate and the hardness. When the cross-sectional coating images in Figure 5.3 are evaluated together with the 2D profilometer data in Figure 5.6, it is observed that the coating in the PIA5 sample has partially detached or diminished in certain regions. This will be further supported by the worn surface morphology to be shown later in Figure 5.9b, where deep grooves similar to those found on the uncoated material and spalling are clearly visible. In contrast, for the PIA10 and PIA15 samples, the wear tracks remain confined within the coating layer, indicating that the coating integrity was preserved during the wear process.

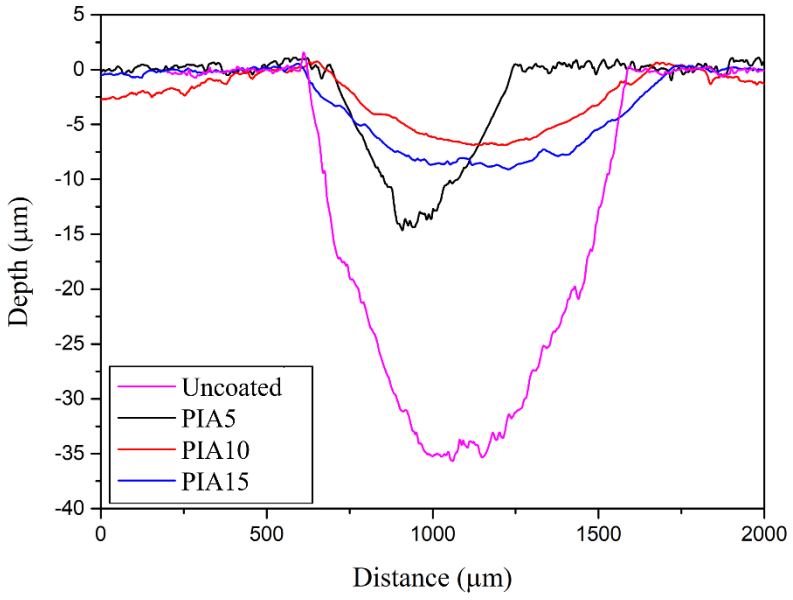

Figure 5.6 : Wear track profiles of the samples.

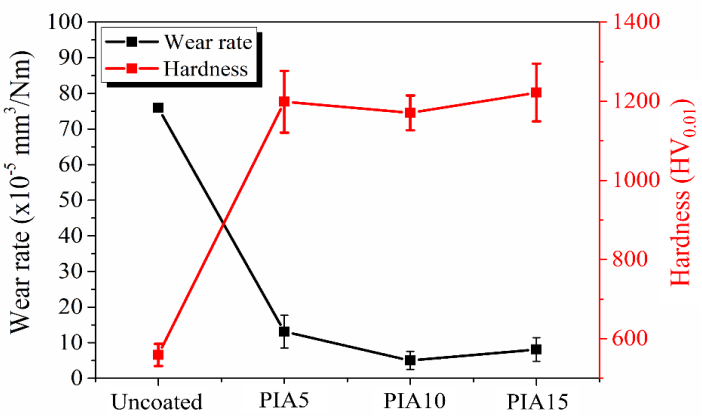

Figure 5.7 : Wear rate and hardness of the samples.

Figure 5.8 represents the friction coefficient variation with the sliding distance for the uncoated and the aluminized IN718 samples. The uncoated sample starts with a friction coefficient of approximately 0.3, rapidly rises, then reach steady state in the range of 0.6-0.7 and continues with oscillations. The PIA5 starts around 0.3, quickly rises to about 0.5, and then reach steady state in the range of 0.5-0.651 values with the fluctuations. It is observed that the friction coefficient is generally slightly lower compared to the uncoated sample. The PIA10 starts from around 0.3 and rapidly increases, exhibiting a relatively more stable friction behavior in the 0.5-0.6 range and it shows fewer oscillations compared to the other samples. The PIA15 starts with low friction but shows sudden increases reaching above 0.6-0.7 and significant oscillations as the test progresses.

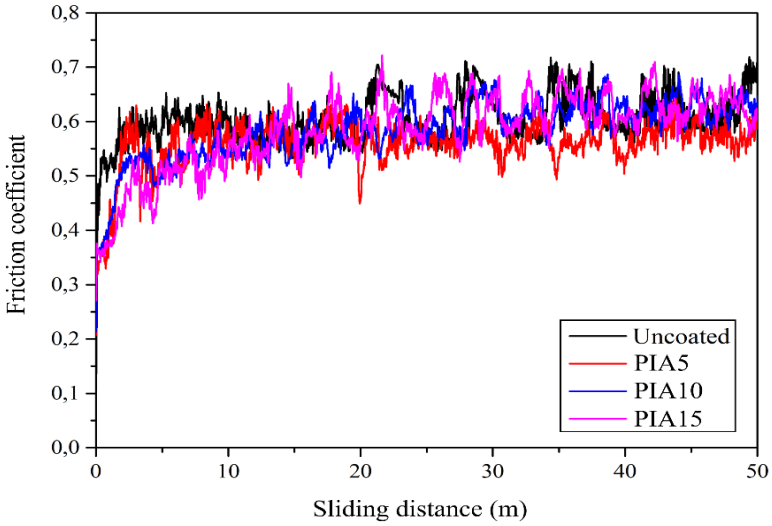

Figure 5.8 : Variation of the friction coefficients with the sliding distance.

The uncoated sample starts with a friction coefficient of approximately 0.3, rapidly rises, then reachs steady state around 0.6, and then exhibits fluctuations in the range of

0.6-0.7 until the end of the test. The PIA5 starts around 0.3, rapidly rises to about 0.6, and then reach steady state with some fluctuations in the range of 0.5-0.6. It is observed that the friction coefficient of the PIA5 sample is slightly lower than that of the uncoated sample. The PIA10 starts from around 0.3 and rapidly increases, exhibiting a relatively more stable friction behavior in the range of 0.5-0.6. The PIA15 starts with a low friction coefficient of 0.3, increase to 0.6 at 20^{th} m of the sliding distance, and finally reaches to the friction coefficient of the uncoated alloy with some fluctuations. Overall, the aluminized coatings are shown to slightly decrease the friction coefficient of the uncoated IN718, which might be attributed to the formation of hard Ni-Al based aluminides on the surface. The fluctuations in the friction coefficient might be attributed to stick-slip mechanism during the continuous movement of the counterface ball on the surface. Wear debris entrapping in between the counterface ball and the sample's surface results in three body abrasion with corresponding rise in the friction coefficient, and subsequent removal of the debris between the surfaces leads to decrease in the friction coefficient. These reperated action exhibits a fluctuation in the friction behaviour of the samples.

Worn surface SEM images of the samples are shown in Figure 5.9. The uncoated sample (Figure 5.9a and e) shows intense oxide and deep grooves. This shows that oxidation takes place during sliding as a result of heat generated by friction during reciprocating motion. Oxide formation and deep grooves in in the uncoated IN718 sample indicates that the dominat wear mechansims are oxidation and abrasive wear. Spalling, grooves and cracks are observed on the wear surface of PIA5 sample. The cracks on the wear surface are caused by the tensile and compressive stresses caused by the repetitive movements of the counter ball and indicate that the fatigue wear mechanism is active in addition to abrasive wear. The spalling areas are caused by the hard and brittle Ni-Al based intermetallic compounds in the coating layer that first cracks and then separate from the surface during the test. The worn surfaces of the PIA10 and PIA15 samples are more uniform in appearance, as compared to the worn surface of the PIA5 sample. It is due to the fact that the wear is penetrated into the substrate in the PIA5 sample because the coating thickness is around 10 μm whereas the wear track depth is around 15 μm. Because the coating thickness is less in the PIA5 sample, more brittle $NiAl_3$ layers near the outer surface would result in a deeper wear track.

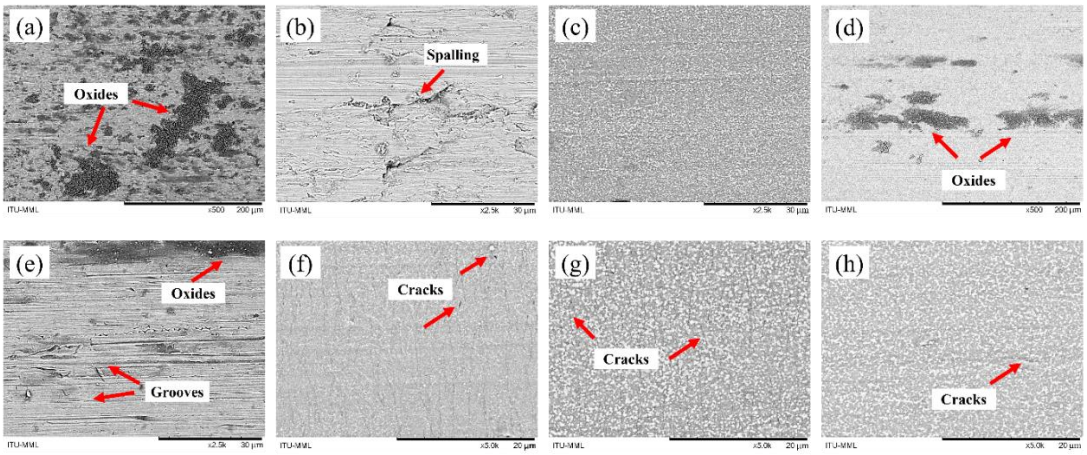

Figure 5.9 : Worn surface SEM images. (a,e) Uncoated, (b,f) PIA5, (c,g) PIA10 and (d,h) PIA15 samples.

Figure 5.10 presents the cross-sectional SEM images of the wear tracks of the samples. As observed in Figure 5.10a, the coating layer on the PIA5 sample has completely disappeared, and the higher-magnification image in Figure 10d reveals the occurrence of brittle fracture in the substrate. As shown in Figures 5.10b,c,e and f, the PIA10 and PIA15 samples exhibited similar subsurface wear damage. In both samples, lateral cracks are observed within the wear tracks. These cracks tend to propagate along the interface between two distinct sublayers of the coating and appear to form an interconnected network. This cracking behavior is attributed to a fatigue wear mechanism, where repeated mechanical stress induced by the counterbody leads to stress accumulation and crack initiation.

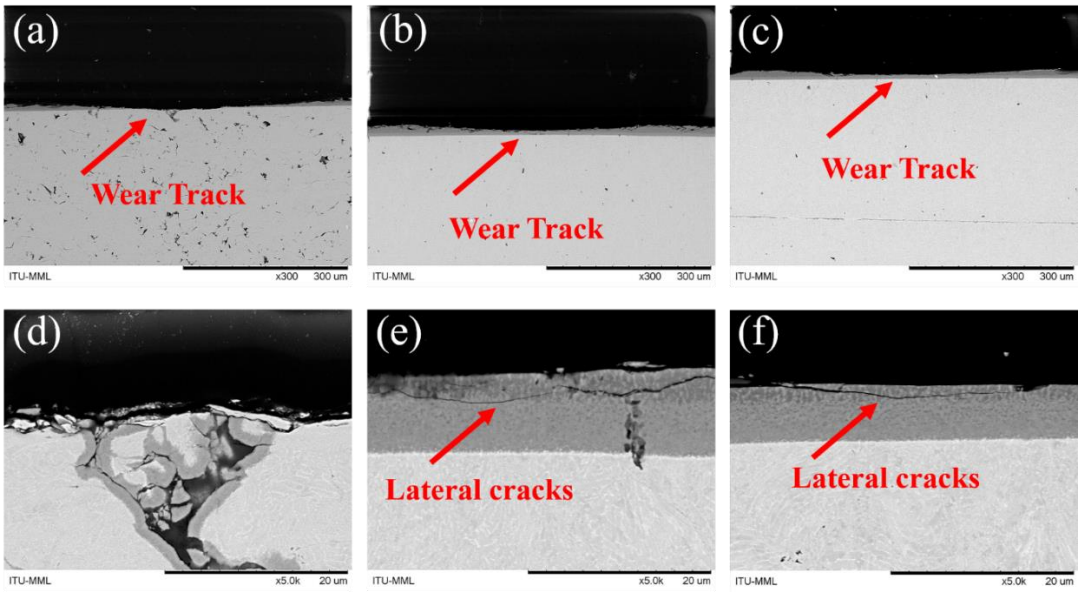

Figure 5.10 : Cross sectional SEM images of the worn tracks. (a) PIA5, (b) PIA10, (c) PIA15 (low magnification), (d) PIA5, (e) PIA10, (f) PIA15 (high magnification).

5.4 Conclusion

This study demonstrated the successful formation of aluminide coatings on IN718 produced with CSAM substrates using a Pack Induction Aluminizing (PIA) process at 1000 °C for durations of 5, 10, and 15 min. The process yielded dense, adherent dual-layer coatings predominantly composed of $NiAl_3$ and Ni_2Al_3 phases. Despite the high process temperature, the short diffusion times preserved the substrate microstructure while enabling the formation of Al-rich intermetallics typical of high-activity, low-temperature aluminizing. The coating thickness increased from ~10 μm for 5 min to ~19 μm for 10 min, and then achieved at stabilization for 15 min of process time. XRD and EDS analyses confirmed the compositional gradient and phase distribution across the coating. The rapid formation of $NiAl_3$ and Ni_2Al_3 phases, which typically require several hours at lower temperatures, was attributed to the enhanced diffusion kinetics facilitated by induction heating, likely supported by localized Joule heating and electromigration effects. Tribological evaluations revealed substantial improvements in friction and wear resistance. The PIA10 and PIA15 samples exhibited shallow wear tracks as compared to the uncoated substrate. SEM investigations confirmed that the coatings exhibit lateral cracks within the coating layers, suggesting fatigue-driven wear mechanisms. Overall, this work highlights the potential of PIA as a time-efficient and thermally controlled surface engineering method for CSAM-produced IN718 components. By enabling the formation of protective aluminide coatings within minutes, this technique offers a compelling alternative to conventional long-duration thermal treatments, particularly for geometrically complex or thermally sensitive components intended for high-temperature service.

6. CONCLUSIONS AND RECOMMENDATIONS

6.1 Conclusions

This doctoral thesis systematically investigated induction-assisted aluminizing as a rapid, energy-efficient, and high-performance surface engineering approach for AISI 316L stainless steel, conventionally forged IN718, and CSAM IN718 alloys. Three aluminizing routes HDA, SA and PA were examined under short-duration induction heating, and their effects on coating formation mechanisms, phase evolution, and functional performance were comprehensively evaluated.

One of the most significant outcomes of this thesis is the demonstration that induction heating can effectively replace conventional long-duration diffusion annealing, reducing process times from several hours to seconds or minutes while still enabling the formation of well-bonded, diffusion-controlled aluminide coatings. The rapid heating rates and localized thermal input associated with induction heating were shown to significantly accelerate atomic diffusion without inducing detrimental microstructural degradation in the substrate materials.

For AISI 316L stainless steel, both HDA and SA routes assisted by induction heating produced functionally graded aluminide coatings composed mainly of Fe_2Al_5, FeAl, and α-Fe(Al) phases. Despite having similar phase constituents, the two processes resulted in markedly different outer-layer morphologies. The HDA route generated a relatively smooth and compact Fe_2Al_5/$FeAl_2Si$-rich outer layer, whereas the SA route produced a distinctive lamellar Fe_2Al_5-dominated structure. Nanoindentation and tribological analyses revealed that the lamellar morphology formed by the SA process led to significantly higher surface hardness, enhanced elastic recovery, and superior wear resistance. A strong linear correlation was established between the wear rate and the ratio of hardness to elastic recovery, indicating that coating toughness plays a decisive role in governing wear behavior. High-temperature oxidation tests conducted at 1000 °C confirmed that both coatings effectively suppressed iron-oxide formation and promoted the development of a thin, adherent Al_2O_3 scale. While SA coatings

exhibited greater diffusion-driven thickness growth during oxidation, HDA coatings demonstrated slightly superior oxidation stability due to the diffusion-retarding influence of Si.

For conventionally forged IN718, induction-assisted HDA and SA processes were shown to significantly modify coating uniformity, phase distribution, and elemental gradients. Induction heating transformed initially Al-rich intermetallic layers into thicker and more diffusion-controlled aluminide structures, primarily consisting of Ni_2Al_3 and NiAl phases. The SA process yielded thinner but more homogeneous coatings with fine grain size and random crystallographic orientation, as confirmed by EBSD analysis—features that are favorable for long-term oxidation resistance. In contrast, HDA coatings achieved comparable uniformity only after induction heating. These findings highlight the critical role of induction heating in tailoring coating architecture and phase evolution, particularly for Ni-based superalloys where precise control of diffusion kinetics is essential.

For CSAM-produced IN718, the proposed PIA method proved to be a highly effective and time-efficient alternative to conventional furnace pack aluminizing. Dense, dual-layer aluminide coatings characteristic of high-activity aluminizing were successfully formed within minutes. The coatings consisted of an outer $Ni(Fe,Cr)Al_3$ layer and an inner $Ni_2(Fe,Cr)Al_3$ layer, with thickness increasing systematically with processing time. Tribological testing demonstrated a substantial reduction in friction coefficient and an improvement in wear resistance exceeding 80% compared to the uncoated alloy. These results confirm that PIA is particularly well-suited for additively manufactured components, where minimizing thermal exposure while achieving high-performance surface protection is crucial.

Overall, this thesis establishes that induction-assisted aluminizing is a versatile, scalable, and industrially relevant surface modification strategy. By combining conventional aluminizing routes with rapid induction heating, it is possible to engineer diffusion-bonded, graded aluminide coatings with tailored microstructures and superior wear and oxidation performance, while significantly reducing energy consumption and processing time.

6.2 Recommendations for Future Work

Based on the findings of this thesis, several recommendations can be made for future research and technological development:

1. **Long-term cyclic oxidation and thermal fatigue studies**: While isothermal oxidation behavior was extensively investigated, future studies should focus on cyclic oxidation and thermal fatigue conditions to better simulate real service environments, particularly for aerospace and energy applications.
2. **Residual stress and adhesion strength analysis**: The rapid thermal cycles associated with induction heating may induce unique residual stress states within the coatings. Advanced techniques such as X-ray stress analysis or micro-cantilever testing could provide deeper insight into coating adhesion and failure mechanisms.
3. **Process scalability and complex geometry evaluation**: Further work is recommended to assess the applicability of induction-assisted aluminizing on large-scale or geometrically complex components, including tubes, blades, and near-net-shape additively manufactured parts.
4. **Extension to other alloy systems**: The methodology developed in this thesis can be extended to other high-temperature alloys, such as ferritic-martensitic steels, cobalt-based superalloys, high-entropy alloys and duplex stainless steels, to explore the broader applicability of induction-assisted diffusion coatings.
5. **Multifunctional coating design**: Future research may also consider combining aluminizing with secondary alloying elements (e.g., Cr, Si, or reactive elements) to further enhance oxidation resistance, wear performance, or hot corrosion behavior.

In conclusion, this doctoral study demonstrates that induction-assisted aluminizing represents a significant advancement in diffusion-based surface engineering, offering a powerful combination of performance enhancement, processing efficiency, and sustainability. The insights gained from this work provide a strong scientific and technological foundation for the development of next-generation protective coatings for demanding industrial applications.

REFERENCES

[1] **Hsieh C. and Wu W.** (2012) "Overview of Intermetallic Sigma Phase Precipitation in Stainless Steels," *ISRN Metallurgy*, vol. 2012, pp. 1–16, doi: 10.5402/2012/732471.

[2] **Dudziak T.** (2023) "Effect of 316L Stainless Steel Fabrication on Oxidation Resistance, Surface Morphology, and Hot Tensile Behavior," *J. Mater. Eng. Perform.*, vol. 32, no. 22, pp. 10443–10454, doi: 10.1007/s11665-023-08321-6.

[3] **Borgioli F., Adachi S. and Lindner T.** (2024) "Advances in Low-Temperature Nitriding and Carburizing of Stainless Steels and Metallic Materials: Formation and Properties*," Multidisciplinary Digital Publishing Institute (MDPI)*, doi: 10.3390/met14101179.

[4] **Saravanan M., Venkateshwaran N., Devaraju A., Krishnakumari A. and Saarvesh J.** (2017) "Surface modification of 316L stainless steel by plasma-assisted low temperature carburizing process," *Surface Review and Letters*, vol. 24, no. 8, doi: 10.1142/S0218625X17501165.

[5] **Ding Y., Chen X., Liu Y.A. and Su X.** (2019) "Effect of diffusion process on coating in hot-dipped aluminized steel," *Surface Review and Letters*, vol. 26, no. 10, doi: 10.1142/S0218625X19500707.

[6] **Dorcheh A.S. and Galetz M.C.** (2016) "Slurry aluminizing: A solution for molten nitrate salt corrosion in concentrated solar power plants," *Solar Energy Materials and Solar Cells*, vol. 146, pp. 8–15, doi: 10.1016/j.solmat.2015.11.024.

[7] **Shetty P.P.** (2019) "Low-Temperature Pack Aluminization Process on Pipeline Steel to Inhibit Asphaltene Deposition," *ACS Appl. Mater. Interfaces*, vol. 11, no. 50, pp. 47596–47605, doi: 10.1021/acsami.9b17430.

[8] **Marulanda J.L., Perez F.J. and Remolina-Millán A.** (2013) "Aluminum-silicon co-deposition by FB-CVD on austenitic stainless steel AISI 316, *Journal of Physics: Conference Series, Institute of Physics Publishing*, doi: 10.1088/1742-6596/466/1/012009.

[9] **Yuan B.** (2024) "Effects of Annealing and Oxidation on the Microstructure of Hot-Dipped Aluminum–Silicon Coating of 316L Stainless Steel," *J. Phase Equilibria Diffus.*, vol. 45, no. 2, pp. 114–131, doi: 10.1007/s11669-024-01092-0.

[10] **Majumdar S., Paul B., Kain V. and Dey G.K.** (2017) "Formation of Al2O3/Fe-Al layers on SS 316 surface by pack aluminizing and heat treatment," *Mater. Chem. Phys.*, vol. 190, pp. 31–37, doi: 10.1016/j.matchemphys.2017.01.002.

[11] **Wang D. and Shi Z.** (2004) "Aluminizing and oxidation treatment of 1Cr18Ni9 stainless steel," *Appl. Surf. Sci.*, vol. 227, no. 1–4, pp. 255–260, doi: 10.1016/j.apsusc.2003.11.076.

[12] **Bauer J.T., Montero X. and Galetz M.C.** (2020) "Fast heat treatment methods for Al slurry diffusion coatings on alloy 800 prepared in air," *Surf. Coat. Technol.*, vol. 381, doi: 10.1016/j.surfcoat.2019.125140.

[13] **Takesue S., Kikuchi S., Misaka Y., Morita T. and Komotori J.** (2020) "Rapid nitriding mechanism of titanium alloy by gas blow induction heating," *Surf. Coat. Technol.*, vol. 399, doi: 10.1016/j.surfcoat.2020.126160.

[14] **Chen X.** (2020) "A high bioactive alkali-treated titanium surface induced by induction heat treatment," *Surf. Coat. Technol.*, vol. 385, doi: 10.1016/j.surfcoat.2020.125362.

[15] **Hu J., Ma C., Yang X., Xu H., Guo N. and Yu H.** (2017) "Microstructure Evolution During Continuous Cooling in AISI 5140 Steel Processed by Induction Heating Chromizing," *J. Mater. Eng. Perform.*, vol. 26, no. 11, pp. 5530–5537, doi: 10.1007/s11665-017-2942-x.

[16] **Yang Y., Aprilia A., Wu K., Tan S.C. and Zhou W.** (2022) "Post-Processing of Cold Sprayed CoNiCrAlY Coatings on Inconel 718 by Rapid Induction Heating," *Metals*, vol. 12, no. 3, doi: 10.3390/met12030396.

[17] **Tang Z., Guo Y., Jia Z., Li Y. and Wei Q.** (2015) "Examining the effect of pileup on the accuracy of sharp indentation testing," *Advances in Materials Science and Engineering*, vol. 2015, doi: 10.1155/2015/528729.

[18] **Karakaş A. and Baydogan M.** (2024) "Hot-Dip Aluminizing of Flow-formed AISI 4140 Steel," in *Procedia Structural Integrity*, Elsevier B.V., pp. 42–46, doi: 10.1016/j.prostr.2024.06.007.

[19] **Kishore K., Chhangani S., Prasad M.J.N.V. and Bhanumurthy K.** (2021) "Microstructure evolution and hardness of hot dip aluminized coating on pure iron and EUROFER 97 steel: Effect of substrate chemistry and heat treatment," *Surf. Coat. Technol.*, vol. 409, doi: 10.1016/j.surfcoat.2020.126783.

[20] **Li R., Liu Y., Liu W., Li H. and Liu H.** (2024) "Fe_2Al_5 formation in the cold-sprayed Al coatings on steel by ultra-fast Joule heating," *Mater. Lett.*, vol. 369, doi: 10.1016/j.matlet.2024.136732.

[21] **Bauer J.T., Montero X., Schütze M. and Galetz M.C.** (2016) "Innovative slurry coating concepts for aluminizing of an austenitic steel in chlorine and sulfur containing atmosphere," *Surf. Coat. Technol.*, vol. 285, pp. 179–186, doi: 10.1016/j.surfcoat.2015.10.074.

[22] **Guo C., Kang C., Xu C. and Wang J.** (2021) "An atomistic investigation of branching mechanism during lamellar eutectic solidification," *Comput. Mater. Sci.*, vol. 196, doi: 10.1016/j.commatsci.2021.110536.

[23] **Sharma G., Awasthi R. and Chandra K.** (2010) "A facile route to produce Fe-Al intermetallic coatings by laser surface alloying," *Intermetallics*, vol. 18, no. 11, pp. 2124–2127, doi: 10.1016/j.intermet.2010.06.023.

[24] **Novák P.** (2010) "Intermediary phases formation in Fe-Al-Si alloys during reactive sintering," *J. Alloys Compd.*, vol. 497, no. 1–2, pp. 90–94, doi: 10.1016/j.jallcom.2010.03.028.

[25] **Majumdar S., Paul B., Kain V. and Dey G.K.** (2017) "Formation of Al2O3/Fe-Al layers on SS 316 surface by pack aluminizing and heat treatment," *Mater. Chem. Phys.*, vol. 190, pp. 31–37, doi: 10.1016/j.matchemphys. 2017.01.002.

[26] **Sathish M., Radhika N. and Saleh B.** (2021) "A critical review on functionally graded coatings: Methods, properties, and challenges," *Composites Part B: Engineering*, doi: 10.1016/j.compositesb.2021.109278.

[27] **ASTM International** (2020) "Standard Specification for Steel Sheet, Aluminum-Coated, by the Hot-Dip Process," *ASTM Standard*, doi: 10.1520/A0463_A0463M-15R20E01.

[28] **Dey P.P., Sahu S., Banerjee P.S. and Ghosh M.** (2023) "A review on metallurgical features of hot-dip aluminized steel," *Materials Futures*, doi: 10.1088/2631-8695/acb902.

[29] **Cheng W.J. and Wang C.J.** (2012) "EBSD characterization of high-temperature phase transformations in an Al-Si coating on Cr-Mo steel," *Mater. Charact.*, vol. 64, pp. 15–20, doi: 10.1016/j.matchar.2011.12.003.

[30] **Takata N., Nishimoto M., Kobayashi S. and Takeyama M.** (2015) "Crystallography of Fe_2Al_5 phase at the interface between solid Fe and liquid Al," *Intermetallics*, vol. 67, pp. 1–11, doi: 10.1016/j.intermet. 2015.07.011.

[31] **Sun Y., Li X., Xu L., Shen H. and Liu Y.** (2024) "Effect of induction heat treatment on microstructure, mechanical and corrosion properties of stainless steel 308 L fabricated using wire arc additive manufacturing," *Sci. Rep.*, vol. 14, no. 1, p. 26089, doi: 10.1038/s41598-024-75382-5.

[32] **Romankov S., Park Y.C., Semin V., Komarov S., Serikkanov A. and Louzguine-Luzgin D.V.** (2024) "Solid-state aluminizing process for high-adhesion composite coatings: Synergistic effects of plastic flow, atomic mixing and interaction on structure and properties," *Surf. Coat. Technol.*, vol. 489, doi: 10.1016/j.surfcoat.2024.131099.

[33] **Zarei F., Nuranian H. and Shirvani K.** (2022) "Development of FeAl Coatings by a Combined Aluminizing Process to Improve the Dry Sliding Wear Resistance of HH309 Alloy," *J. Mater. Eng. Perform.*, vol. 31, no. 9, pp. 7337–7352, doi: 10.1007/s11665-022-06744-1.

[34] **Gao Y., Yu Z., Gu H., Ren X. and Li Y.** (2025) "Cracking resistance and adhesion of Al/Al2O3 thick lamellar structure coatings sprayed with plasma spraying," *Appl. Surf. Sci.*, vol. 682, doi: 10.1016/j.apsusc.2024. 161701.

[35] **Erappa Rajj B.** (2024) "Nano-Sized Al2O3-Gr Reinforced Al7075 Hybrid Composite: Impact of Cooling Agents on Mechanical, Wear, and Fracture Behavior," *ACS Omega*, vol. 9, no. 16, pp. 17878–17890, doi: 10.1021/acsomega.3c08822.

[36] **Moshkovich A., Lapsker I. and Rapoport L.S.** (2024) "The Effect of Plastic Deformation on the Flattening of Friction Surfaces," *Lubricants*, vol. 12, no. 8, doi: 10.3390/lubricants12080276.

[37] **Riastuti R., Siallagan S.T., Rahmat Z. and Bancin B.A.H.** (2018) "The study of mechanical properties and corrosion resistance of Molybdenum coating and Aluminum coating using Thermal Spray method on stainless steel 316L," in *IOP Conference Series: Materials Science and Engineering*, Institute of Physics Publishing, doi: 10.1088/1757-899X/420/1/012058.

[38] **Sahoo D.K., Mohanty B.S., Pradeep A.M.V. and John A.D.F.** (2020) "An experimental study on friction surfaced coating of Aluminium 6063 over AISI 316 stainless steel substrate," *Mater. Today Proc.*, vol. 40, pp. S10–S18, doi: 10.1016/j.matpr.2020.03.251.

[39] **Zhou J., Yang M., Wang R. and Pang X.** (2017) "Annealing behavior of aluminum coating prepared by arc spraying on P355NL1 steel," *Surf. Coat. Technol.*, vol. 330, doi: 10.1016/j.surfcoat.2017.09.073.

[40] **Günen A. and Ergin Ö.** (2023) "A Comparative Study on Characterization and High-Temperature Wear Behaviors of Thermochemical Coatings Applied to Cobalt-Based Haynes 25 Superalloys," *Coatings*, vol. 13, no. 7, doi: 10.3390/coatings13071272.

[41] **Erdogan A., Yener T., Doleker K.M., Korkmaz M.E. and Gök M.S.** (2021) "Low-temperature aluminizing influence on degradation of nimonic 80A surface: Microstructure, wear and high temperature oxidation behaviors," *Surfaces and Interfaces*, vol. 25, doi: 10.1016/j.surfin.2021.101240.

[42] **Lekakh S.N., Neroslavsky O., Li M. and Godlevski L.** (2022) "Stochastic Model for High Temperature Oxidation of Cr–Ni Austenitic Steels Assisted by Spallation," *Oxidation of Metals*, vol. 98, no. 3–4, pp. 239–254, doi: 10.1007/s11085-022-10120-8.

[43] **Li W.** (2025) "Effect of Aluminizing and Laser Shock Peening Treatments on the High-Temperature Oxidation Resistance of AISI 321 Stainless Steel for Solar Thermal Power Heat Exchanger," *Chinese Journal of Mechanical Engineering*, vol. 38, no. 1, doi: 10.1186/s10033-025-01217-7.

[44] **Azimaee H., Sarfaraz M., Mirjalili M. and Aminian K.** (2019) "Effect of silicon and manganese on the kinetics and morphology of the intermetallic layer growth during hot-dip aluminizing," *Surf. Coat. Technol.*, vol. 357, pp. 483–496, doi: 10.1016/j.surfcoat.2018.10.035.

[45] **Huang X.** (2020) "Oxidation behavior of 316L austenitic stainless steel in high temperature air with long-term exposure," *Mater. Res. Express*, vol. 7, no. 6, doi: 10.1088/2053-1591/ab96fa.

[46] **Erdogan C., Vural H., Karakaş A., Fenercioğlu T.O. and Yalçinkaya T.** (2023) "Ductile failure of Inconel 718 during flow forming process and its numerical investigation," *Eng. Fail. Anal.*, vol. 152, doi: 10.1016/j.engfailanal.2023.107424.

[47] **Cojocaru M.O., Branzei M. and Druga L.N.** (2022) "Aluminide Diffusion Coatings on IN 718 by Pack Cementation," *Materials*, vol. 15, no. 15, doi: 10.3390/ma15155453.

[48] **Yener T.** (2022) "Wear and oxidation performances of low temperature aluminized IN600," *Surf. Coat. Technol.*, vol. 436, doi: 10.1016/j.surfcoat.2022.128295.

[49] **Telbakiroğlu Y.B. and Konca E.** (2023) "Effect of Aluminizing on the Oxidation of Inconel 718 and Inconel 738LC Superalloys at 925–1050°C," *Research Square*, doi: 10.21203/rs.3.rs-3186106/v1.

[50] **Čelko L., Hutařová S., Petrenec M., Obrtlík K., Hrčková M. and Podrábský T.** (2014) "Microstructural characterization of slurry aluminide diffusion coatings," in *Materials Science Forum*, Trans Tech Publications Ltd, pp. 584–589, doi: 10.4028/www.scientific.net/MSF.782.584.

[51] **Kopec M.** (2024) "Recent Advances in the Deposition of Aluminide Coatings on Nickel-Based Superalloys: A Synthetic Review (2019–2023)," *Coatings*, doi: 10.3390/coatings14050630.

[52] **Wang C.J. and Chen S.M.** (2006) "Microstructure and cyclic oxidation behavior of hot dip aluminized coating on Ni-base superalloy Inconel 718," *Surf. Coat. Technol.*, vol. 201, no. 7, pp. 3862–3866, doi: 10.1016/j.surfcoat.2006.07.242.

[53] **Shmorgun V.G., Bogdanov A.I., Kulevich V.P., Iskhakova L.D. and Taube A.O.** (2021) "Microstructure and phase composition of diffusion coating formed in NiCr alloys by hot-dip aluminizing," *Surfaces and Interfaces*, vol. 23, doi: 10.1016/j.surfin.2021.100988.

[54] **Rasmussen A.J., Agüero A., Gutierrez M. and Østergård M.J.L.** (2008) "Microstructures of thin and thick slurry aluminide coatings on Inconel 690," *Surf. Coat. Technol.*, vol. 202, no. 8, pp. 1479–1485, doi: 10.1016/j.surfcoat.2007.06.056.

[55] **Sun W.** (2019) "Improving microstructural and mechanical characteristics of cold-sprayed Inconel 718 deposits via local induction heat treatment," *J. Alloys Compd.*, vol. 797, pp. 1268–1279, doi: 10.1016/j.jallcom.2019.05.099.

[56] **Dalaee M.T., Gloor L., Leinenbach C. and Wegener K.** (2020) "Experimental and numerical study of the influence of induction heating process on build rates Induction Heating-assisted laser Direct Metal Deposition (IH-DMD)," *Surf. Coat. Technol.*, vol. 384, doi: 10.1016/j.surfcoat.2019.125275.

[57] **Hu J., Ma C., Yang X., Xu H., Guo N. and Yu H.** (2017) "Microstructure Evolution During Continuous Cooling in AISI 5140 Steel Processed by Induction Heating Chromizing," *J. Mater. Eng. Perform.*, vol. 26, no. 11, pp. 5530–5537, doi: 10.1007/s11665-017-2942-x.

[58] **Takesue S., Kikuchi S., Akebono H., Morita T. and Komotori J.** (2020) "Characterization of surface layer formed by gas blow induction heating nitriding at different temperatures and its effect on the fatigue properties of titanium alloy," *Results in Materials*, vol. 5, doi: 10.1016/j.rinma.2020.100071.

[59] **Bakhtiary O., Sarraf S. and Soltanieh M.** (2025) "Microstructure evaluation of Si-modified aluminide coatings on IN625 deposited by slurry aluminizing process," *Surf. Coat. Technol.*, vol. 495, doi: 10.1016/j.surfcoat.2024.131592.

[60] **Bozza F.** (2014) "Diffusion mechanisms and microstructure development in pack aluminizing of Ni-based alloys," *Surf. Coat. Technol.*, vol. 239, pp. 147–159, doi: 10.1016/j.surfcoat.2013.11.034.

[61] **Zhang X.** (2024) "On the effect of thermal diffusion treatment on the hot-dipped Al-Si alloy coating on Fe-Cr-B cast steel," *Constr. Build. Mater.*, vol. 411, doi: 10.1016/j.conbuildmat.2023.134631.

[62] **Kavukcu A., Kaba M., Muhaffel F. and Baydoğan M.** (2022) "High Temperature Wear Behavior of Hot-Dip Aluminized Inconel 718," in 31st International Conference on Metallurgy and Materials, *METAL*, TANGER Ltd., pp. 493–499, doi: 10.37904/metal.2022.4423.

[63] **Tu X.** (2015) "Oxidation and microstructure evolution of Al-Si coated Ni3Al based single crystal superalloy with high Mo content," *Appl. Surf. Sci.*, vol. 325, pp. 20–26, doi: 10.1016/j.apsusc.2014.11.076.

[64] **Wu K., Aprilia A., Tan S.C. and Zhou W.** (2023) "Rapid post processing of cold sprayed Inconel 625 by induction heating," *Materials Science and Engineering: A*, vol. 872, doi: 10.1016/j.msea.2023.144955.

[65] **Sekido N., Aizawa R. and Ueno S.** (2019) "Effect of Cr addition on the phase equilibria and oxidation behavior of NbSi2," *Mater. Trans.*, vol. 60, no. 5, pp. 666–673, doi: 10.2320/matertrans.MB201809.

[66] **Zhang Y., Pint B.A., Cooley K.M. and Haynes J.A.** (2008) "Formation of aluminide coatings on Fe-based alloys by chemical vapor deposition," *Surf. Coat. Technol.*, vol. 202, no. 16, pp. 3839–3849, doi: 10.1016/j.surfcoat.2008.01.023.

[67] **Bose S.** (2007) *High Temperature Coatings*, Elsevier, doi: 10.1016/B978-0-7506-8252-7.X5000-8.

[68] **Goral M., Ochal K., Kubaszek T. and Drajewicz M.** (2020) "The influence of deposition technique of aluminide coatings on oxidation resistance of different nickel superalloys," in *Materials Today: Proceedings*, Elsevier Ltd, pp. 1746–1751, doi: 10.1016/j.matpr.2020.04.863.

[69] **Kepa T., Bonnet G. and Pedraza F.** (2021) "Oxidation behaviour of ultrafast slurry aluminized nickel," *Surf. Coat. Technol.*, vol. 424, doi: 10.1016/j.surfcoat.2021.127667.

[70] **Shekari M., Adeli M., Khobzi A., Kobashi M. and Kanetake N.** (2017) "Induction-activated self-propagating, high-temperature synthesis of nickel aluminide," *Advanced Powder Technology*, vol. 28, no. 11, pp. 2974–2979, doi: 10.1016/j.apt.2017.09.004.

[71] **Kepa T., Pedraza F. and Rouillard F.** (2020) "Intermetallic formation of Al-Fe and Al-Ni phases by ultrafast slurry aluminization (flash aluminizing)," *Surf. Coat. Technol.*, vol. 397, doi: 10.1016/j.surfcoat.2020.126011.

[72] **Sarraf S.H., Soltanieh M. and Rastegari S.** (2023) "Reactive air aluminizing of a nickel-based superalloy (IN738LC): Coating formation mechanism," *Surf. Coat. Technol.*, vol. 456, doi: 10.1016/j.surfcoat.2023.129229.

[73] **Liu Z., Jie X., Wu H., Shen G., She G. and Wang D.** (2023) "The Preparation and Properties of Ni_2Al_3 Intermetallic Compound Coating," *Coatings*, vol. 13, no. 11, doi: 10.3390/coatings13111900.

[74] **Wang X., Fan F., Szpunar J.A. and Zhang L.** (2015) "Influence of grain orientation on the incipient oxidation behavior of Haynes 230 at 900 °C," *Mater. Charact.*, vol. 107, pp. 33–42, doi: 10.1016/j.matchar. 2015.06.029.

[75] **Cheng W.J. and Wang C.J.** (2011) "Microstructural evolution of intermetallic layer in hot-dipped aluminide mild steel with silicon addition," *Surf. Coat. Technol.*, vol. 205, no. 19, pp. 4726–4731, doi: 10.1016/ j.surfcoat.2011.04.061.

[76] **Kopec M.** (2024) "Effect of Aluminide Coating Thickness on High-Temperature Fatigue Response of MAR-M247 Nickel-Based Superalloy," *Coatings*, vol. 14, no. 8, doi: 10.3390/coatings14081072.

[77] **Sun W.** (2019) "Improving microstructural and mechanical characteristics of cold-sprayed Inconel 718 deposits via local induction heat treatment," *J. Alloys Compd.*, vol. 797, pp. 1268–1279, doi: 10.1016/j.jallcom. 2019.05.099.

[78] **Karakaş A., Ataee A., Rathi A., Fenercioğlu T.O., Erdogan C. and Yalçinkaya T.** (2025) "Post heat treatment optimization of cold spray additive manufactured Inconel 718," *Sci. Rep.*, vol. 15, no. 1, p. 7361, doi: 10.1038/s41598-025-90723-8.

[79] **Li W., Yang K., Yin S., Yang X., Xu Y. and Lupoi R.** (2018) "Solid-state additive manufacturing and repairing by cold spraying: A review," J. *Mater. Sci. Technol.*, vol. 34, no. 3, pp. 440–457, doi: 10.1016/j.jmst. 2017.09.015.

[80] **Vaz R.F. et al.** (2022) "Metal Knitting: A New Strategy for Cold Gas Spray Additive Manufacturing," *Materials*, vol. 15, no. 19, doi: 10.3390/ma15196785.

[81] **Garfias A.** (2025) "Repair of Inconel 718 parts by Cold Spray Additive Manufacturing: The effect of substrate preheating on thick coatings properties," *J. Alloys Compd.*, vol. 1010, doi: 10.1016/j.jallcom.2024. 178182.

[82] **Bryndza G.** (2025) "Review of the Microstructural Impact on Creep Mechanisms and Performance for Laser Powder Bed Fusion Inconel 718," *Materials*, doi: 10.3390/ma18020276.

[83] **Wang Y., Suneson M. and Smialek J.L.** (2014) "Oxidation Behavior of Hf-Modified Aluminide Coatings on Inconel-718 at 1050°C," *Journal of Coating Science and Technology*, vol. 1, no. 1, pp. 25–45, doi: 10.6000/2369-3355.2014.01.01.4.

[84] **Wang C.J. and Chen S.M.** (2006) "Microstructure and cyclic oxidation behavior of hot dip aluminized coating on Ni-base superalloy Inconel 718," *Surf. Coat. Technol*., vol. 201, no. 7, pp. 3862–3866, doi: 10.1016/j.surfcoat. 2006.07.242.

[85] **Tang Z., Yang C., Duan Y., Ma L., Zheng S. and Li M.** (2024) "Corrosion and wear behaviors of Inconel 718 nickel-based alloy by boroaluminizing," *Surf. Coat. Technol*., vol. 478, doi: 10.1016/j.surfcoat.2024.130500.

[86] **Wang T.** (2021) "Microstructure and wear properties of laser-clad NiCo alloy coating on Inconel 718 alloy," *J. Alloys Compd*., vol. 879, doi: 10.1016/j.jallcom.2021.160412.

[87] **Yu L.** (2023) "Introducing both chemical and structural gradients in AISI 321 stainless steel via aluminizing and laser shock peening for superior properties," *Surf. Coat. Technol*., vol. 472, doi: 10.1016/j.surfcoat. 2023.129942.

[88] **Kumar S., Satapathy B., Pradhan D. and Mahobia G.S.** (2019) "Effect of surface modification on the hot corrosion resistance of Inconel 718 at 700 °C", Mater. Res. Express, vol. 6, no. 8, doi: 10.1088/2053-1591/ab1dc7.

[89] **Hu J.** (2018) "Effect of pack-chromizing temperature on microstructure and performance of AISI 5140 steel with Cr-coatings," *Surf. Coat. Technol.*, vol. 344, pp. 656–663, doi: 10.1016/j.surfcoat.2018.03.099.

[90] **Yang Y., Aprilia A., Wu K., Tan S. And Zhou W.** (2022) "Post-Processing of Cold Sprayed CoNiCrAlY Coatings on Inconel 718 by Rapid Induction Heating", *Metals*, Vol 12(3), https://doi.org/10.3390/met12030396

[91] **Assadi H., Gärtner F., Stoltenhoff T. and Kreye H.** (2003) "Bonding mechanism in cold gas spraying," *Acta Mater*., vol. 51, no. 15, pp. 4379–4394, doi: 10.1016/S1359-6454(03)00274-X.

[92] **Assadi H., Kreye H., Gärtner F. and Klassen T.** (2016) "Cold spraying – A materials perspective," *Acta Mater*., vol. 116, pp. 382–407, doi: 10.1016/j.actamat.2016.06.034.

[93] **Sun Y., Dong J., Zhao P. and Dou B.** (2017) "Formation and phase transformation of aluminide coating prepared by low-temperature aluminizing process," *Surf. Coat. Technol*., vol. 330, pp. 234–240, doi: 10.1016/j.surfcoat.2017.10.025.

[94] **Latief F.H. and Kakehi K.** (2014) "Influence of post ageing on creep behaviour of aluminized Ni-based single crystal superalloy prepared by low-activity high-temperature," *Vacuum*, vol. 109, pp. 157–161, doi: 10.1016/j.vacuum.2014.07.003.

[95] **Erdeniz D. and Dunand D.C.** (2014) "Microstructure development during pack aluminization of nickel and nickel-chromium wires," *Intermetallics*, vol. 50, pp. 43–53, doi: 10.1016/j.intermet.2014.02.009.

[96] **Thevand A., Poizet S., Crousier P. and Streiff R.** (1981) "Aluminization of nickel-formation of intermetallic phases and Ni_2Al_3 coatings.", *Journal of Materials Science*, vol 16, 2467-2479, doi.org/10.1007/ BF01113583

[97] **Jopek J., Mokrzycka M., Góral M., Koscielniak B., Ochal K. and Drajewicz M.** (2023) "High Temperature Protective Coatings for Aeroengine Applications," *Manufacturing Technology*, vol. 23, no. 4, pp. 436–448, doi: 10.21062/mft.2023.052.

[98] **Bryndza G.** (2025) "Review of the Microstructural Impact on Creep Mechanisms and Performance for Laser Powder Bed Fusion Inconel 718," *Materials,* doi: 10.3390/ma18020276.

[99] **Tang Z. et** (2024) "Effects of boriding and aluminizing on the electrochemical and wear behavior of IN-718 nickel-based alloy," *Surf. Coat. Technol*., vol. 494, doi: 10.1016/j.surfcoat.2024.131314.

[100] **Lei X.** (2024) "High-temperature oxidation resistances of coatings on Inconel 718 alloy by boriding, aluminizing, and boroaluminizing," *Surf. Coat. Technol*., vol. 494, doi: 10.1016/j.surfcoat.2024.131506.

[101] **Grimme C., Oskay C., Mengis L. and Galetz M.C.** (2021) "High temperature wear behavior of δ-Ni_2Al_3 and β-NiAl coatings formed on pure nickel using pack cementation process and diffusion heat treatment," *Wear*, vol. 477, doi: 10.1016/j.wear.2021.203850.

[102] **Döleker K.M.** (2025) "Investigation of high temperature wear and cyclic oxidation behavior of pack-aluminized Inconel 601," *J. Alloys Compd*.,vol. 1020, doi: 10.1016/j.jallcom.2025.179541.

CURRICULUM VITAE

Name Surname **:** Aptullah KARAKAŞ

EDUCATION **:**

- **B.Sc.** **:**2013, University of Dumlupinar, Engineering Faculty, Ceramic Engineering
- **M.Sc.** **:**2015, Gebze Technical University, Institute of Science and Technology, Material Science and Engineering

PROFESSIONAL EXPERIENCE AND REWARDS:

- 2017-still: Materials Technologies Team Leader at Repkon Company
- Best Paper Award**,** ICMME 2024: XVIII. International Conference on High Temperature Coatings

PUBLICATIONS, PRESENTATIONS AND PATENTS ON THE THESIS:

- **Aptullah Karakaş**, Erdem Balcı, Murat Baydoğan, (2026), Pack Aluminizing by Induction Heating: Application to Inconel 718 Produced by Cold Spray Additive Manufacturing, Materials Research Express https://doi.org/10.1088/2053-1591/ae3711
- **Aptullah Karakaş**, Erdem Balcı, Murat Baydoğan, (2025), Induction assisted hot-dip and slurry aluminizing of Inconel 718 Materials Research Express https://doi.org/10.1088/2053-1591/ae22c5
- **Aptullah Karakaş**, Erdem Balcı, Murat Baydoğan, (2025), Enhanced Wear and Oxidation Resistance of AISI 316L Stainless Steel via Slurry and Hot-Dip Aluminizing Assisted by Rapid Induction Heating, Langmuir https://doi.org/10.1021/acs.langmuir.5c04513
- **Aptullah Karakaş**, Murat Baydoğan, (2023), Crack Formation after Diffusion Annealing of Hot-Dip Aluminized AISI 4140 Steel, Procedia Structural Integrity https://doi.org/10.1016/j.prostr.2024.06.008
- **Aptullah Karakaş**, Murat Baydoğan, (2023), Hot-Dip Aluminizing of Flow-formed AISI 4140 Steel, Procedia Structural Integrity https://doi.org/10.1016/j.prostr.2024.06.007

- **Aptullah Karakas** and Murat Baydogan, (2024), The Effect of Bath Composition for Hot-Dip Aluminizing of AISI 4140 Steel, ICMME 2024: XVIII. International Conference on High Temperature Coatings
- **Aptullah Karakas** and Murat Baydogan, (2024), The Effect of Substrate Surface Roughness for Hot Dip Aluminizing of IN718 Alloy ICMME 2024: XVIII. International Conference on Metallurgical and Materials Engineering

OTHER PUBLICATIONS, PRESENTATIONS AND PATENTS:

- Oguzhan Kurt, Huseyin Tursun, **Aptullah Karakaş**, Bulent Acar, (2026), Fatigue Failure of a Conveyor Roller Shaft and Design Improvement Materials Research Express https://doi.org.10.1007/s11668-025-02365-7
- Özgün Yurdakul, **Aptullah Karakaş**, Bülent Acar, (2025), Comparison between Experimental Results and FEM-Based Analyses of Flow-Formed AISI 4140 Steel by Wear Rate Examination with Microscratch Testing, Tribology Transactions https://doi.org/10.1080/10402004.2025.2564885
- Erdem Balcı, **Aptullah Karakaş**, Burak Bayram, Mertcan Kaba, Faiz Muhaffel, Pınar Korkmaz Tilki, Evren Tan, Murat Baydoğan, (2025) Formation of In Situ Al/TiAl3 Coatings on Electron Beam Melted (EBM) Ti-6Al-4V Alloy by Cold Spray and Induction Heating, Journal of Thermal Spray Technology https://doi.org/10.1007/s11666-025-01994-6
- Ali Yetgin, **Aptullah Karakaş**, Bülent Acar, Emre Özaslan, (2025), Failure analysis and design improvement of a hot ironing die holder Engineering Failure Analysis https://doi.org/10.1016/j.engfailanal.2025.109397
- **Aptullah Karakaş**, Arash Ataee, Amit Rathi, Tevfik Ozan Fenercioğlu, Can Erdogan, Tuncay Yalçinkaya, (2025), Post heat treatment optimization of cold spray additive manufactured Inconel 718 Scientific Reports https://doi.org/10.1038/s41598-025-90723-8
- Ali Yetgin, **Aptullah Karakaş**, Bülent Acar, Emre Özaslan, Failure analysis of a helical compression spring with relatively low spring index, (2024), Engineering Failure Analysis https://doi.org/10.1016/j.engfailanal.2024.108798
- Can Erdogan, Hande Vural, **Aptullah Karakaş**, Tevfik Ozan Fenercioğlu, Tuncay Yalçinkaya, (2024), Ductile failure of Inconel 718 during flow forming process and its numerical investigation, Engineering Failure and Analysis https://doi.org/10.1016/j.engfailanal.2023.107424
- Elif Yazgan, Mehmet Mutlu, Güneş Aydin, **Aptullah Karakas**, Tevfik Fenercioglu, Murat Baydoğan, (2023), Mechanical and microstructural properties of AISI 4140 after flow-forming process Materials Research Proceedings
- Hande Vural, CAN Erdoğan, **Aptullah Karakaş**, Tevfik Fenercioglu, Tuncay Yalçınkaya, (2023), Experimental identification of uncoupled ductile damage models and application in flow forming of IN718 Materials Research Proceedings
- Mehmet Mutlu, **Aptullah Karakaş**, Hakan Kuşdemir, Umut Koltan, Tuncay Yalçinkaya, (2023), Flow forming and recrystallization behaviour of CuZn30 alloy, Esaform, Materials Research Proceedings https://doi.org/10.21741/9781644902479-112

- Mehmet Mutlu, Atasan Özsoy, T. Ozan Fenercioglu, **Aptullah Karakaş**, Murat Baydoğan, (2023), Effect of reduction ratio in flow forming process on microstructure and mechanical properties of a 6082 Al alloy Materials Research Proceedings https://doi.org/10.21741/9781644902479-111
- **Aptullah Karakaş**, Tevfik Ozan Fenercioğlu, Tuncay Yalçinkaya, (2022), The influence of flow forming on the precipitation characteristics of Al2024 alloys, Materials Letters https://doi.org/10.1016/j.matlet.2021.130066
- **Aptullah Karakaş**, Acar Can Kocabıçak, Senai Yalçınkaya, Yusuf Şahin, (2021), Flow forming process for annealed AISI 5140 alloy steel tubes Fracture, Fatigue and Wear https://doi.org/10.1007/978-981-15-9893-7_10
- Acar Can Kocabıçak, **Aptullah Karakaş**, Güneş Aydın, Senai Yalçınkaya, (2021), Investigation of flow forming process and heat treatment effects on 2024 aluminium tubes, Fracture, Fatigue and Wear https://doi.org/10.1007/978-981-15-9893-7_8
- **Aptullah Karakas**, Ali Sabri Berkem, Ahmet Capoglu, (2017), Mechanical behaviour of in-situ formed Cordierite-Anorthite ceramic composite Central and Eastern European Conference on Thermal Analysis and Calorimetry, Moldova 2017
- **Aptullah Karakas**, Ali Sabri Berkem, Ahmet Capoglu, (2017), Electrical properties and thermal expansion of in-situ formed Cordierite-Anorthite ceramic composite, Central and Eastern European Conference on Thermal Analysis and Calorimetry, Moldova